Optimum Design of Rib-Reinforced Composite I-beam

by

Amin Deldari Alamdari

B.S., Mechanical Engineering, University of Tabriz, 2015

Submitted to the Institute for Graduate Studies in
Science and Engineering in partial fulfillment of
The requirements for the degree of
Master of Science

Graduate Program in Mechanical Engineering

Boğaziçi University

2021

ACKNOWLEDGEMENTS

First of all, I would like to express my deep gratitude to my master thesis advisor, Prof. Fazıl Önder Sönmez for his endless support, kindness, encouragement and for his precious advice through this work. He is not only an outstanding academician but also a great man, I am very grateful to have the chance to get to know him.

I would like to mention that this study would not have been possible without the support of my lovely family. I would like to thank my mother for her love and permanent support, my sister for her encouragements, my father for believing in me in every stages of my life and our new member of family my brother-in-law. Without having these people behind me, there was no chances for any successes.

At the end, I would like to thank my friends Farzad Rahmani, Sina Dadashzadeh, Sina Narimani, Elyar Sharifi, Hasan Coban, Ayse Cifci, Mine Cifci, my cousin and my fat mate Babak and all friends who always had my back. Additionally, I would like to thank my lovely friend Selma Basibuyuk, she helped me in the last days and save my life, thanks for your great friendship during last four years. I hope you will not forget to mention my name in your PhD thesis.

ABSTRACT

OPTIMUM DESIGN OF RIB-REINFORCED COMPOSITE I-BEAM

The main goal of this study is to develop a methodology for optimum shape design of reinforcing ribs on the web of an I-beam so as to minimize the weight of the structure and maximize the buckling-load carrying capacity of the beam under three-point bending test condition. IM7/8552 carbon-fiber reinforced composite material is selected for the model because of its high strength with low density. A finite element model is developed to simulate the mechanical behavior of the I-beam under three-point bending. The model is validated by comparing its predictions with the results of an experimental study. Then, an I-beam with a large web is considered so that the most critical failure mode is web-buckling due to transverse shear loads. Tsai-Wu criterion is used to predict static failure. By using ANSYS Parametric Design Language (APDL), codes are developed to implement the optimization algorithm and carry out buckling analyses to determine the maximum buckling-load capacity. The design variables are the geometric parameters defining the shape, size, and orientation of the ribs. Three different configurations are considered for the ribs and a parametric study is conducted to select the best rib configuration for optimization. Additionally, another parametric study is done to find the best stacking sequence for the layers of the web. The optimum shape and orientation angle of the ribs are found using modified simulated annealing algorithm, which is a global search algorithm. A considerable improvement is obtained in load-carrying capacity of the I-beam by introducing the optimum rib configuration, which results in an insignificantly small increase in the use material compared to the I-beam with flat web.

ÖZET

Kaburga Takviyeli Kompozit I-kirişin Optimum Tasarımı

Bu çalışmanın temel amacı, yapının ağırlığını en aza indirmek ve kirişin üç nokta altında burkulma yükü taşıma kapasitesini en üst düzeye çıkarmak için bir I-kirişin ağı üzerindeki takviye nervürlerinin optimum şekil tasarımı için bir metodoloji geliştirmektir. bükme testi koşulu. Model için düşük yoğunluklu ve yüksek mukavemeti nedeniyle IM7 / 8552 karbon fiber takviyeli kompozit malzeme seçilmiştir. Üç noktalı eğilme altında I-kirişin mekanik davranışını simüle etmek için bir sonlu eleman modeli geliştirilmiştir. Model, öngörüleri deneysel bir çalışmanın sonuçlarıyla karşılaştırılarak doğrulanır. Daha sonra, büyük bir ağa sahip bir I-kiriş düşünülür, böylece en kritik arıza modu, enine kesme yükleri nedeniyle ağ burkulmasıdır. Statik arızayı tahmin etmek için Tsai-Wu kriteri kullanılır. ANSYS Parametrik Tasarım Dili (APDL) kullanılarak, optimizasyon algoritmasını uygulamak ve maksimum burkulma-yük kapasitesini belirlemek için burkulma analizleri yapmak için kodlar geliştirilir. Tasarım değişkenleri, nervürlerin şeklini, boyutunu ve yönünü tanımlayan geometrik parametrelerdir. Kaburgalar için üç farklı konfigürasyon dikkate alınır ve optimizasyon için en iyi nervür konfigürasyonunu seçmek için bir parametrik çalışma yürütülür. Ek olarak, web katmanları için en iyi istifleme sırasını bulmak için başka bir parametrik çalışma yapılır. Kaburgaların optimum şekli ve yönelim açısı, global bir arama algoritması olan değiştirilmiş benzetilmiş tavlama algoritması kullanılarak bulunur. Optimum nervür konfigürasyonu getirilerek I-kirişin yük taşıma kapasitesinde önemli bir gelişme elde edilir, bu da düz ağlı I-kirişe kıyasla kullanım malzemesinde önemsiz derecede küçük bir artışa neden olur.

TABLE OF CONTENTS

LIST OF FIGURES

LIST OF TABLES

LIST OF SYMBOLS

E_1	Longitudinal modulus
E_2	Transverse modulus
E_3	Through-thickness modulus
g	Gravitational acceleration
G_{12}	In-plane shear modulus
G_{13}	Transverse shear modulus
G_{23}	Through-thickness modulus
L	Total length of the I-beam
L_M	Length of the Markov chain
$L_{M,k}$	Length of the kth Markov chain
LF	Buckling load factor
m	Mass
n	Total number of variables
N	Number of laminate layers
w(x)	Deflection of the neutral axis
q(x)	Applied load
I	The second moment of inertia
P	Applied load
κ	Shear correction factor
A	Area of the cross section
T_k	Temperature of the kth Markov chain
T_0	Initial temperature
Δu	Change of displacement
U	Displacement in direction of X
V	Displacement in direction of Y
w	Displacement in direction of Z
V_f	Fiber volume fraction
σ_{ij}	Stress matrix components

σ_1	Normal stress in fiber direction
σ_2	Normal stress in transverse direction
σ_3, S_{12}	Shear stress
σ_{1c}	Longitudinal compressive strength
σ_{1t}	Longitudinal tensile strength
σ_{2c}	Transverse compressive strength
σ_{2t}	Transverse tensile strength
τ_{12}	Shear stress in the elastic symmetry plane 1-2
τ_{13}	Shear stress in the elastic symmetry plane 1-3
τ_{23}	Shear stress in the elastic symmetry plane 2-3
X_t	Tensile strength parallel to the fiber direction
X_c	Compressive strength parallel to the fiber direction
Y_t	Tensile strength normal to the fiber orientation
Y_c	Compressive strength normal to the fiber orientation
ε_1	Normal strain in the direction 1
ε_2	Normal strain in the direction 2
ε_3	Normal strain in the direction 3
γ_{12}	Shear strain component in the elastic symmetry plane 1-2
γ_{13}	Shear strain component in the elastic symmetry plane 1-3
γ_{23}	Shear strain component in the elastic symmetry plane 2-3
ϵ_{1t}^u , ϵ_{1c}^u	Longitudinal strains at failure in tension or compression in the Direction 1
ϵ_{2t}^u , ϵ_{2c}^u	Longitudinal strains at failure in tension or compression in the direction 2
γ_{12}^u	Shear strain at failure in the elastic symmetry plane 1-2
υ_{12}	Poisson's ratio for loading in the plane 1-2
t_f, t_s	Thickness of flanges
t_c, t_w	Thickness of webs
LF	Buckling load factor of rib-reinforced I-beam
LF_0	Buckling load factor of I-beam without rib
W	Total weight of the rib-reinforced I-beam
C_i	Weighting coefficient

W_0	Total weight of the I-beam without rib-reinforced
W_{rib}	Width of the ribs
L_{rib}	Length of the ribs
f	Objective function
f_h	Objective function value of the current configuration

LIST OF ACRONYMS/ABBREVIATIONS

2D	Two Dimensional
3D	Three Dimensional
APDL	ANSYS Parametric Design Language
CBT	Composite Beam Theory
CFRP	Carbon Fiber Reinforced Polymer
DOF	Degree of Freedom
FE	Finite Element
FEA	Finite Element Analysis
FEM	Finite Element Modelling
FRP	Fiber Reinforced Polymer
GA	Genetic Algorithm
GFRP	Glass Fiber Reinforced Polymer
GPa	Giga-Pascal
kg	Kilogram
kN	Kilo Newton
m	Meter
MBT	Modified Beam Theory
mm	Millimeter
MPa	Mega-Pascal
MSA	Modified Simulated Annealing
SA	Simulated Annealing

1. INTRODUCTION

Materials based on their properties and characteristics are divided into four main categories: Metals, plastics, ceramics, and composites. Each category involves large numbers of materials with different properties that sometimes overlap each other. Composite material means two or more materials combined on a macroscopic scale that behave as a single material. Different materials are combined to form a composite material so as to improve mechanical properties. Fibrous, laminated, particulate composite materials, and a combination of them are common types of composite materials. They find application in industries such as automotive, construction, marine, and aerospace.

The most important class of composite materials is continuous fiber-reinforced composites, because they have high strength and stiffness-to-weight ratios. For this reason, they are used in weight-critical applications. Considering their high material cost, composite part design should be optimized so that the desired performance is achieved with a minimum use of material or the performance is maximized for a given amount of material.

I-beams are commonly used to support transverse loads in various applications like spar beams in airplane wings, construction, aerospace, and marine engineering applications. I-beams should be designed to support the applied load without failure. Failure modes in beams are classified into two major types: flexural failure and shear failure. The former occurs when the imposed load exceeds the flexural capacity of the materials of the beam, while the latter occurs due to deficiency in shear resistance between different materials of the beam [1]. Buckling failure of I-beams will be discussed in more detail in the next chapter.

Bending-load carrying capacity of an I-beam can be increased by increasing its area moment of inertia. This can be achieved without an increase in its weight by making its flanges thicker and web thinner. However, as the web is made thinner, buckling of the web

becomes the dominant failure mode, especially if the web height is large as shown in Figure 1.1.

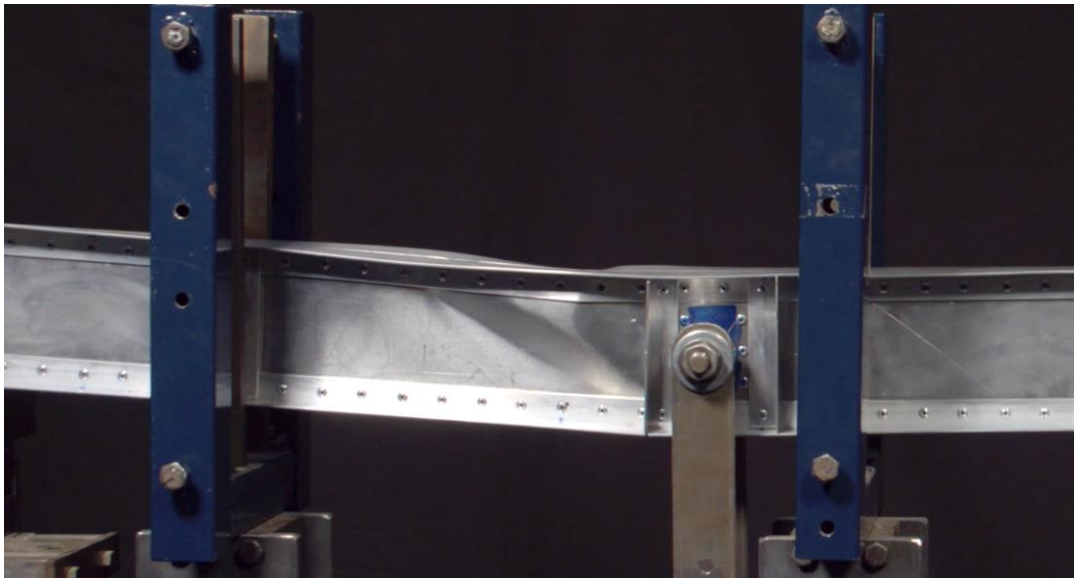

Figure 1.1. Web local buckling of an I-beam under pure bending.

Shear buckling of web is one of the dominant failure modes of I-beam structures especially if the web height is large. There are several methods to avoid shear buckling of the web such as designing the web in corrugated shape as shown in Figure 1.2, using stiffeners on the web, and increasing thickness of the web. Thicker web means increased weight, and thus increased material cost of the structure. Considering that composite materials are costly and they are generally used in weight-critical applications, increasing thickness is undesirable. Corrugated webs have complex shapes leading to manufacturing difficulty in joining web and flange parts of the I-beam. On the other hand, using stiffeners and ribs makes possible to significantly increase buckling strength of I-beams with little increase in weight.

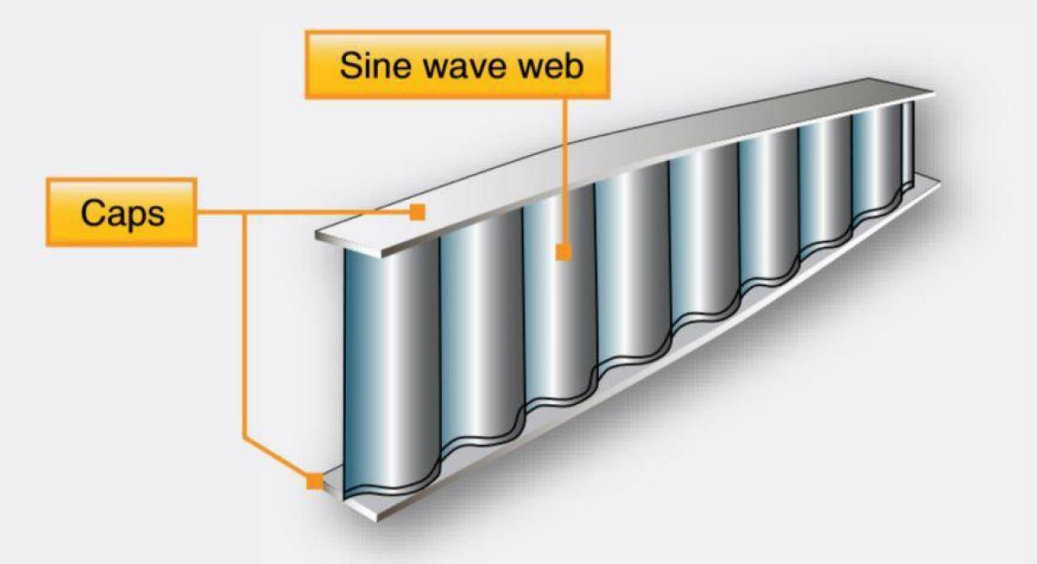

Figure 1.2. An illustration of an I-beam with sine wave web design [2].

1.1. Literature Review

Three-point bending test is generally used to determine the flexural strength and stiffness of composite materials [4,5]. The test causes bending and shearing of specimens, therefore it involves a more complex stress state compared to tension tests. The web is predominantly under normal stresses due to bending and flange is predominantly under shear stresses. Besides, geometric parameters greatly affect the mechanical behavior of specimens. There are a few studies in the literature on composite I-beams under three-point bending test. Most of them considered a composite I-beam without any reinforcement and tried to determine its mechanical behavior under three-point bending test. Some others investigated the effect of dimensions of the I-beam parts on its mechanical properties. A review of these studies is presented in the following:

Ozbasaran [6] analyzed the optimal design of an I-section beam-column subjected to different loading conditions. In that study, dimensions of the I-beam were considered as design variables. The I-beam was optimized using the crow search algorithm. In the optimization procedure, the critical factors were found to be buckling and large-deflection, if the flange and web thicknesses are small.

Yang et al. [7] experimentally and numerically investigated global buckling behavior of I-beams under three-point bending. That study showed all the test specimens developed lateral-torsional buckling and no local buckling. Increasing the slenderness or height-to-width of the I-beams resulted in lower critical buckling load and lead to simultaneous local buckling.

A fiber-reinforced polymer member design is commonly controlled by deflection and/or buckling instability, therefore buckling analysis is important in structures made by FRP material [8, 9]. Composite beams may undergo local buckling, global buckling or combination of both [8]. As a results, for local buckling numerous studies are conducted for different cross-sections [10-13]. Zeinali et al. [8] developed an experimental and numerical study on lateral torsional buckling of I-beam under three-point bending test. They showed the critical buckling load was increased non-linearly by decreasing span length of the I-beam.

Elbanna et al. [14] conducted an analytical study on the behavior of web of an I-beam with longitudinal and/or transverse stiffeners under pure in-plane bending condition using finite element modeling. They carried out a through parametric study to analyze the geometric parameters such as position, the flexural rigidity of the stiffeners and web plate aspect ratios. That study proposed that the stiffeners should be placed near the compression flange to get the maximum web buckling strength. Additionally, that study suggested that bend-buckling carrying capacity of stiffened panels is substantially related to the boundary condition along the edge of the stiffeners.

Barbero and Raftoyiannis [15] used Rayleigh-Ritz method to analyze anisotropic flanges of I-beams. They developed an analytical solution to predict critical buckling loads and the buckling mode of the I-beams.

Because of great benefits of ribs and stiffeners for helping structures to increase their strength under different loading types, there are a some studies in the literature on the design

optimization of stiffened and rib-reinforced composite structures. Lindgaard and Lund [16] optimized formulations for non-linear critical buckling load of composite structures. They considered different types of buckling behavior by concentrating on criterion functions for gradient-based optimization of the buckling load of laminated composite structures. They tried to maximize the buckling load considering fiber orientation angle as design variables.

Nguyen et al. [17] optimized thin-walled composite I-beams to maximize the critical buckling load by using micro-genetic algorithm. They considered geometric parameters and fiber orientation angle as design variables. Their numerical study showed that the geometric parameters were more effective than fiber orientation in increasing the buckling strength. Additionally, this study revealed that length-to-height ratio and height-to-width ratio of I-beams had significant effect on the critical buckling load.

Duvaut et al. [18] introduced and developed a new technique for finding the optimum fiber directions and fibers volume fraction. They found their optimum values for different parts of the structure. Their optimization procedure considered both local and global buckling.

Morton and Webber [19] proposed an optimization method to obtain minimum-weight design of a composite I-beam. All the I-beam dimensions were taken as design variables. They considered intra-laminar failure and buckling failure in the optimization procedure.

1.2. Problem Statement

The objectives of this thesis is to develop a methodology to maximize the web-buckling strength of I-beams by optimizing the shape of ribs. First, a finite element model of I-beam is developed to investigate its mechanical behavior under three-point bending loading. The dimensions of the I-beam and the rib shapes are defined parametrically using ANSYS parametric design language (APDL). The model is verified for an unstiffened I-

beam by comparing the model predictions with the experimental results reported by a previous study. After that, a parametric study is conducted to investigate the effects of different placements of ribs and choose suitable values for upper and lower limits of the parameters defining the rib shape.

Lastly, using a modified version of simulated annealing, which is a powerful stochastic global search algorithm, optimal shapes of various rib configurations are obtained.

2. THEORETICAL BACKGROUND

2.1. Three-Point Bending Test

Bending test methods have several characteristics that make them very useful and frequent to use in engineering applications. They have feasibility to measure different mechanical properties of materials. Young's modulus, shear modulus, shear stress, fracture toughness etc., are some of these mechanical properties. Between bending test methods, the three-point bending test is the common technique that used mostly in engineering field [20]. The main motives for the popularity of this method are its simplicity and reliable results. Three-point test usually used for assess mechanical properties of polymers, wood, composites and brittle materials [21].

Three-point bending tests as shown in Figure 2.1 are usually applied on rectangular beams. These beams take place on two rollers or pins as supports and the load applied slowly by another roller or pin in the middle of the beam. As the result of this loading, the tensile stress is developed in the convex side of the beam, and the compressive stress is generated on the concave side of the beam.

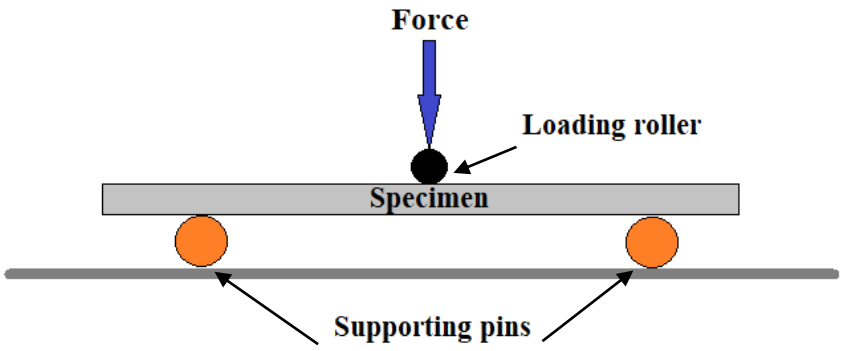

Figure 2.1. Typical three-point bending test.

The three-point bending test have some advantages and disadvantages. The preparation process of specimens and the procedure of testing is easy to apply, but the results of the test are depended on specimen geometry and loading conditions.

If the section of the beam is in the shape of I, the shear stress that produced in the web part of the beam becomes a critical factor. It is due to possibility of failure of the beam because of shear buckling in the web part. This study investigates the shear buckling of the I-beams and try to reduce the effect of generated shear load by adding ribs on the web part of the beam.

2.2. I-Beam Structure

An I-beam as shown in Figure 2.2 is a beam with an I-shaped cross-section. The horizontal elements of the beam are called flanges and the vertical element is called web. I-beams are widely used in construction, civil engineering, aerospace and automotive. The design and structure of the I-beam makes it uniquely capable of handling a variety of loading conditions. The web part of the beam resists shear force, while the flanges resist most of the bending moment applied on beam. Due to design of the I-beam, it capable of bending under very high stress instead of buckling. I-beans are commonly used as critical support trusses or the main framework in the structures due to their mentioned characteristic.

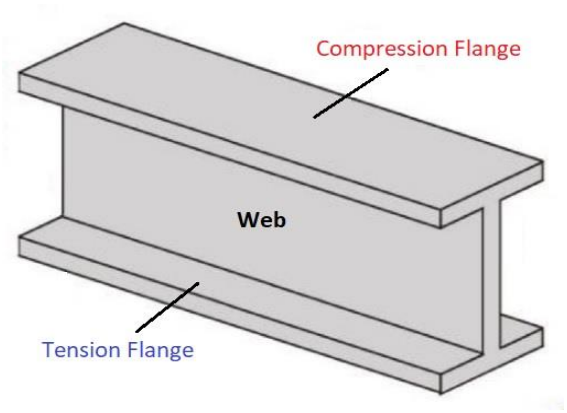

Figure 2.2. Parts of an I-beam.

2.3. Buckling

If a load applied on a structure, it undergoes failure due to exceeded local stresses from the maximum allowable stress of the material. However, it can fail because of another failure mode which results in collapsing of entire structure. In engineering, this kind of failure mode called buckling. Study of buckling for structures begins in 1744 by Euler [22] for the stability of flexible compressed beams.

Buckling is the instant change in the shape of structural elements under loading. It happens when a member in compression becomes elastically instable because of its slenderness and load [23]. The corresponding load is called critical buckling load. Primarily it is the case that accompanied with failure of structures in shape of column which have more length [24]. Beams, plates and shells are types of structures which buckling failure may be critical. Figure 2.3. shows the different types of buckling for different structures.

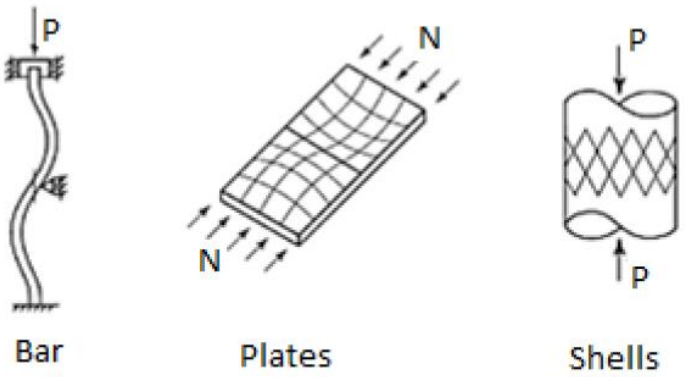

Figure 2.3. Different buckling types of structures [25].

Buckling analysis is crucial for structures in the form of beam because they are slender structures [26]. The main aim of buckling analysis is to anticipate the critical buckling load and deformation of structure in buckling procedure, which lead to understand the load carrying capacity of the structure and prevent the structure from collapsing. Consequently,

in design of structures, avoiding buckling failure is one of the important criterion that must be consider.

Structures which buckled has more than one critical buckling load. It means, when a structure is restrained from buckling by a lateral support, it might buckle at a higher load than the first critical buckling load. In mechanics of engineering different types of buckling shape of a structure is called buckling modes.

2.3.1. Buckling Analysis Types

Buckling occurs as an instability of a structure when it cannot support the applied compressive load levels. Each load level has an associated buckled mode shape; this is the shape that the structure predicted to behave in a buckled condition. Buckling is a critical failure criterion for various of structures. The type of buckling is related to the loading level, loading type, mechanical properties of material and geometry of the structure under loading. This part of study looks at two common buckling calculation, eigenvalue linear buckling and non-linear buckling, methods in finite element analysis (FEA).

2.3.1.1. Eigenvalue Linear Buckling.

Eigenvalue linear buckling analysis predicts the theoretical critical buckling load of an ideal elastic without any non-linearity in geometry or mechanical properties of material [28]. This method known as classical Euler buckling analysis. In an eigenvalue linear buckling problem, we are try to find corresponding load with singular stiffness matrix of the model [27]. This method overestimates the capacity of the structure and material during buckling process. It only gives the buckling behavior of the structure under loading, and there is not any way to predict post-buckling behavior of structure. Additionally, it used to predict the critical buckling loads of ideal structure without any imperfections. As a result, it is not

recommended for accurate, realistic buckling prediction analysis. Advantages of eigenvalue linear buckling are:

+ Short computing time
+ Easy to define accurately
+ No convergence problems
+ No experience is required

On the other hand, it has some disadvantages as following:

– In many cases the results may not be accurate
– Cannot take material nor geometrical non-linearity into account

2.3.1.2. Non-Linear Buckling.

The results of non-linear buckling are more accurate and match with real world outcomes because it employs non-linear, large-deflection and static analysis simultaneously to predict buckling load. It increases the applied load level gradually until it reaches critical load that structure becomes unstable. By unstable it means very large deflections occurs due to an infinitesimal increase in the load. This type of buckling analysis allows to model structure with geometric imperfections, load perturbations, material non-linearity and gaps. Non-linear buckling analysis has some disadvantages as following:

+ Any software that used for analysis in this method can animate failure process
+ Results are more robust than eigenvalue linear buckling outcomes
+ Non-linearity of the material and geometry can be defined in this analysis method

However, it has some pitfalls:

– The analysis process requires more computing time
– There exists convergence problem in results
– It is very difficult to set up the process

Figure 2.4 exhibits load-displacement curve of linear and non-linear finite element method (FEM) model. The diagram shows that when the bar enters into plastic deflection

region, the loss of stiffness result in a great decrease of critical buckling load in comparison between linear and non-linear model [27].

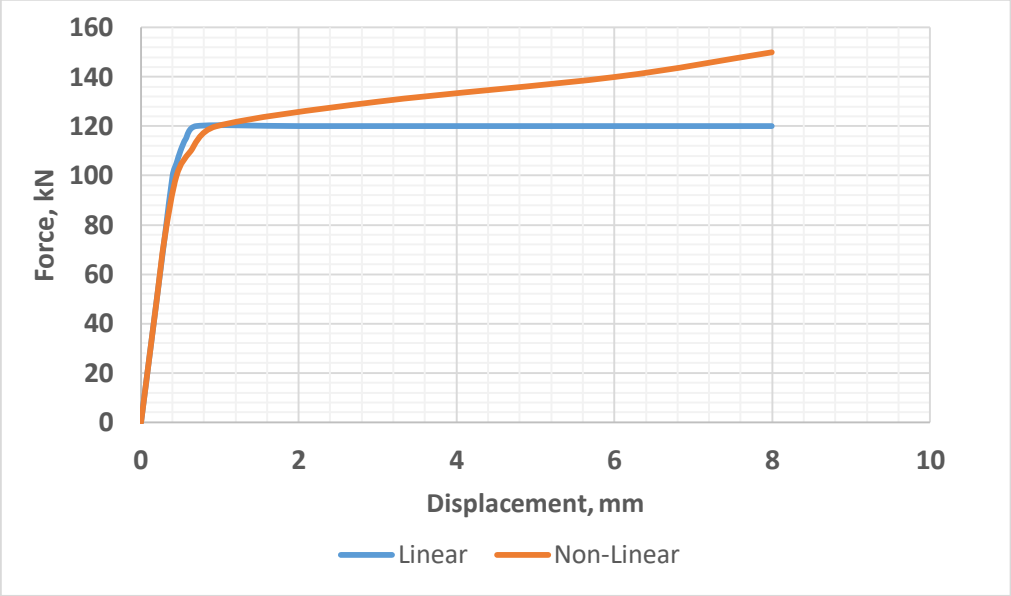

Figure 2.4. Load-displacement curve of linear and nonlinear analysis.

2.3.2. Buckling Modes of an I-Beam

Buckling modes of beams with I-shaped section is categorized as following [29]:

- Lateral-Torsional Buckling (LTB)
- Local Buckling
- Lateral-Distortional Buckling

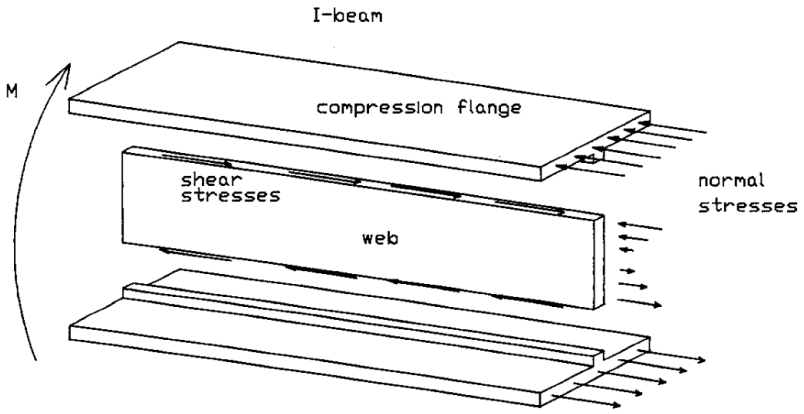

Figure 2.5. Representation of I-beam as Separate Flanges and web [8].

When a simply supported beam experience flexure load condition, the top flange of the I-beam is under compression, and the bottom flange of the I-beam in tension (Figure 2.5). Beams experience Lateral-Torsional Buckling (Figure 2.6. (a)) because of buckling of the under compression flange of a beam. Lateral buckling is combination of lateral displacement and twist of the beam without local buckling in the cross-section geometry [29]. The Lateral-Torsional Buckling can be prevented by suitable lateral bracing. The other factors that affect the Lateral-Torsional Buckling are the size and geometry of the beam, boundary conditions, initial imperfections of the geometry and material and the type of the loading.

Local buckling (Figure 2.6. (b)) subdivided into two failure mode, Flange Local Buckling and Web Local Buckling. It considered as changes in the cross-section geometry of the flanges and/or web without significant lateral displacement or twist. This type of buckling failure mode can be controlled by choosing acceptable width to thickness ratio of flanges and the web parts. Web Local Bucking occurs when the width-thickness ratio of web part is greater than the moment of the beam resistance limit. Local instability can take place in the web part of the beam due to shear loading because of bending load applied on beam (Figure 2.5.). When the web is slender enough, local buckling due to shear loading is governing [30]. Flange Local Buckling is precisely the same as Web Local Buckling, but in term of the flanges.

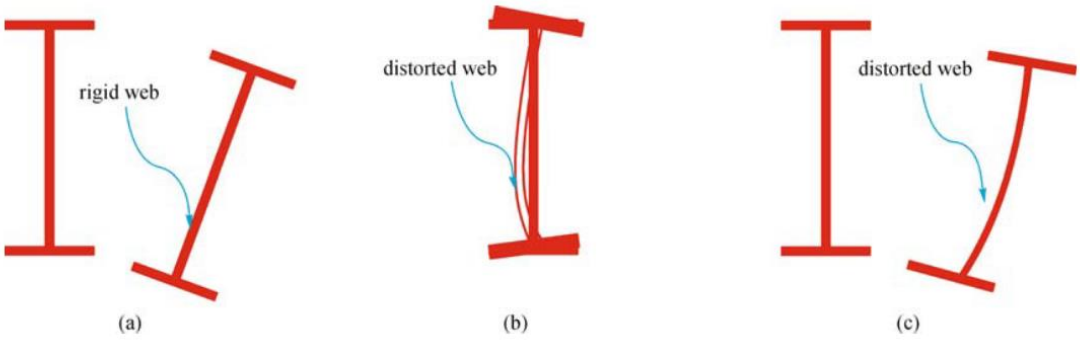

Figure 2.6. Buckling modes of steel I-beams. (a) Lateral-torsional buckling; (b) local buckling; (c) lateral-distortional buckling [26].

Lateral-Distortional Buckling (Figure.2.6. (c)) is combination of several buckle failure modes. Lateral displacement and twist, associated with local changes in the geometry of cross-section results in Lateral-Distortional Buckling. This kind of buckling usually occurs in intermediate length beams with thick flanges and thin webs. It has been shown [31, 32] that, Lateral-Distortional Buckling can lead to remarkable decreasing of the critical buckling load for beams with certain dimensions.

2.4. Laminated Composite Material

Aforementioned, materials have four main types as metals, plastics, ceramics, and composites. Composite materials are combinations of the first three types. Composite materials are made up of two or more materials which combined together in macroscopic scale to achieve desirable mechanical properties. Based on structures, there exist two types of composite materials, sandwich-structured and laminate-structured. In this study, laminated-structured composites are considered due to their suitability of I-beam shape structures.

A lamina or ply is a standard sheet of composite material which is plane or curved layer of unidirectional or woven fabric in a matrix [33] as shown in Figure 2.7. The laminae

are an orthotropic material therefore laminae have different mechanical properties based on their configuration of fibers. For instance, in fiber reinforced lamina, mechanical properties of ply depend on direction of the fibers inside the matrix as shown in Figure 2.8 [34]. Therefore, laminated composites have more than one Young's modulus, shear modulus and so on.

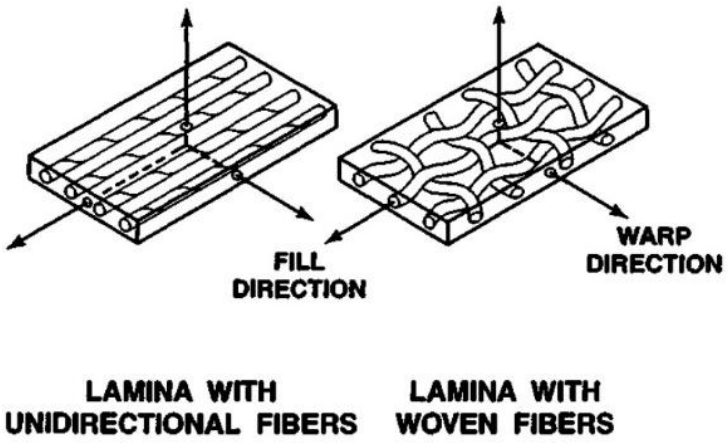

Figure 2.7. Different fiber arrangement in a lamina [35].

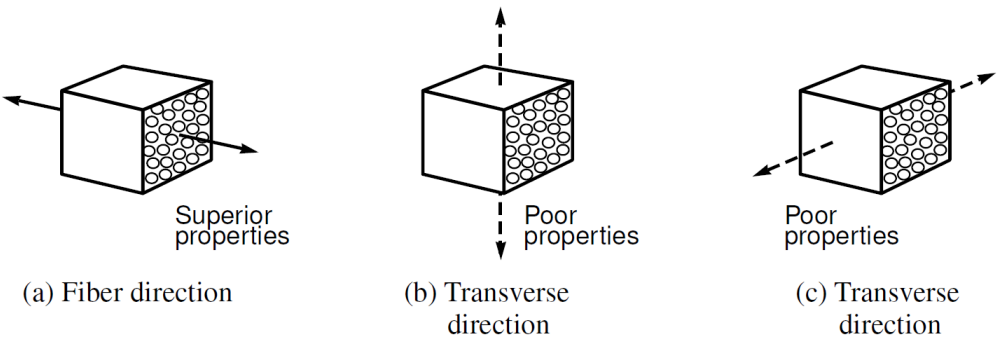

Figure 2.8. Direction dependent mechanical properties of fiber reinforced lamina [34].

To produce laminate with different stiffness and thickness. The laminate thickness is very small in contrast to other dimensions. The mechanical properties of a laminated

composite depend on the stacking sequence and the properties of its components such as reinforcement and matrix material. The laminate is assumed to have perfectly bonded laminae. Additionally, the bonds consider as non-shear deformable, and due to this the displacements are continuous across lamina boundaries [35].

2.4.1. Elastic Constitutive Relations for an Orthotropic Lamina

The state of stress at a small point of continuum materials under loading can be illustrated by nine stress components as σ_{ij} (where i, j = 1, 2, 3) as shown in Figure 2.9. At the same way deformation state can be illustrates as ε_{ij}. Generally, the stress and strain components are related by Hooke's law as following:

$$\sigma_{ij} = C_{ijkl}\varepsilon_{kl}, \tag{2.1}$$

$$\varepsilon_{ij} = S_{ijkl}\sigma_{kl}, \tag{2.2}$$

where i, j, k, l = 1, 2, 3, C_{ijkl}'s are stiffness components, and S_{ijkl}'s are compliance components. Thus, generally, we will need 81 elastic components to identify any material. However, since stress and strain tensors are symmetric ($\sigma_{ij} = \sigma_{ji}$ and $\varepsilon_{ij} = \varepsilon_{ji}$) the number of independent elastic constants reduce to 36 from 81. Thus, the stress-strain relations for an anisotropic material can be expressed as:

$$\sigma_i = C_{ij}\varepsilon_j, \tag{2.3}$$

$$\varepsilon_i = S_{ij}\sigma_j. \tag{2.4}$$

Where i, j = 1, 2, 3, …6, σ_i's are σ_1, σ_2, σ_3, $\sigma_4 = \tau_{23}$, $\sigma_5 = \tau_{13}$, and $\sigma_6 = \tau_{12}$ respectively, and ε_i's are ε_1, ε_2, ε_3, $\varepsilon_4 = \gamma_{23}$, $\varepsilon_5 = \gamma_{13}$, and $\varepsilon_6 = \gamma_{12}$ respectively.

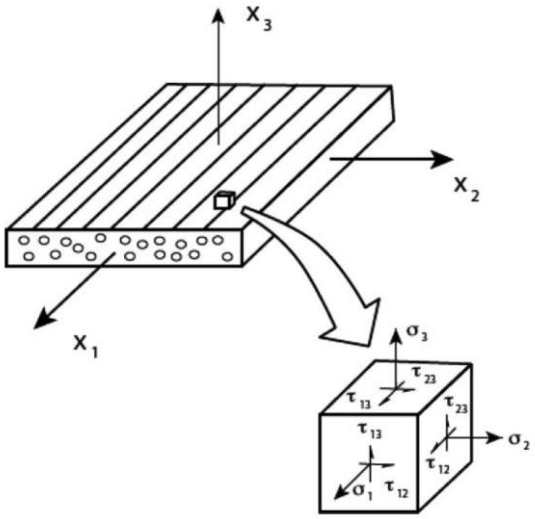

Figure 2.9. State of stress at a point of a continuum [36].

Additionally, stiffness and compliance tensors are symmetric, therefore the stress (or strain) components can be described by six independent constants. As a result, the constitutive equation can express by 21 independent elastic constants. For an orthotropic material, due to interrelation between stiffness and compliance terms, the number of independent constants is reduced to nine in constitutive equations. Thus, stress-strain relations in orthotropic material in the matrix form are:

$$\begin{bmatrix} \sigma_1 \\ \sigma_2 \\ \sigma_3 \\ \tau_{23} \\ \tau_{13} \\ \tau_{12} \end{bmatrix} = \begin{bmatrix} C_{11} & C_{12} & C_{13} & 0 & 0 & 0 \\ C_{12} & C_{22} & C_{23} & 0 & 0 & 0 \\ C_{13} & C_{23} & C_{33} & 0 & 0 & 0 \\ 0 & 0 & 0 & C_{44} & 0 & 0 \\ 0 & 0 & 0 & 0 & C_{55} & 0 \\ 0 & 0 & 0 & 0 & 0 & C_{66} \end{bmatrix} \begin{bmatrix} \varepsilon_1 \\ \varepsilon_2 \\ \varepsilon_3 \\ \gamma_{23} \\ \gamma_{13} \\ \gamma_{12} \end{bmatrix}, \tag{2.5}$$

and

$$\begin{bmatrix} \varepsilon_1 \\ \varepsilon_2 \\ \varepsilon_3 \\ \gamma_{23} \\ \gamma_{13} \\ \gamma_{12} \end{bmatrix} = \begin{bmatrix} S_{11} & S_{12} & S_{13} & 0 & 0 & 0 \\ S_{12} & S_{22} & S_{23} & 0 & 0 & 0 \\ S_{13} & S_{23} & S_{33} & 0 & 0 & 0 \\ 0 & 0 & 0 & S_{44} & 0 & 0 \\ 0 & 0 & 0 & 0 & S_{55} & 0 \\ 0 & 0 & 0 & 0 & 0 & S_{66} \end{bmatrix} \begin{bmatrix} \sigma_1 \\ \sigma_2 \\ \sigma_3 \\ \tau_{23} \\ \tau_{13} \\ \tau_{12} \end{bmatrix}. \tag{2.6}$$

Now, since most of the composite structure are used in the form of thin laminated it can be assumed the composite laminae are under plane stress condition. Consider the orthotropic lamina (Figure 2.10) that loaded in the plane of the lamina. In this condition out-of-plane stresses σ_3, τ_{23}, and τ_{13} are negligible.

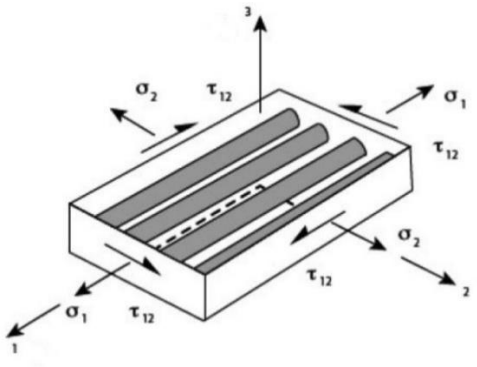

Figure 2.10. Composite lamina under plane stress condition [36].

Therefore, the orthotropic stress-strain equations become

$$\begin{bmatrix} \sigma_1 \\ \sigma_2 \\ 0 \\ 0 \\ 0 \\ \tau_{12} \end{bmatrix} = \begin{bmatrix} C_{11} & C_{12} & C_{13} & 0 & 0 & 0 \\ C_{12} & C_{22} & C_{23} & 0 & 0 & 0 \\ C_{13} & C_{23} & C_{33} & 0 & 0 & 0 \\ 0 & 0 & 0 & C_{44} & 0 & 0 \\ 0 & 0 & 0 & 0 & C_{55} & 0 \\ 0 & 0 & 0 & 0 & 0 & C_{66} \end{bmatrix} \begin{bmatrix} \varepsilon_1 \\ \varepsilon_2 \\ \varepsilon_3 \\ \gamma_{23} \\ \gamma_{13} \\ \gamma_{12} \end{bmatrix}, \tag{2.7}$$

or

$$\begin{bmatrix}\sigma_1\\ \sigma_2\\ \tau_{12}\end{bmatrix}=\begin{bmatrix}Q_{11} & Q_{12} & 0\\ Q_{12} & Q_{22} & 0\\ 0 & 0 & Q_{66}\end{bmatrix}\begin{bmatrix}\varepsilon_1\\ \varepsilon_2\\ \gamma_{12}\end{bmatrix}, \tag{2.8}$$

and

$$\begin{bmatrix}\varepsilon_1\\ \varepsilon_2\\ \gamma_{12}\end{bmatrix}=\begin{bmatrix}S_{11} & S_{12} & 0\\ S_{12} & S_{22} & 0\\ 0 & 0 & S_{66}\end{bmatrix}\begin{bmatrix}\sigma_1\\ \sigma_2\\ \tau_{12}\end{bmatrix}. \tag{2.9}$$

where, $Q_{ij} = C_{ij} - \frac{C_{i3}C_{j3}}{C_{33}}$ (i, j = 1, 2, 6).

Thus, the constitutive equations for an orthotropic lamina under plane stress condition can be represented by only four independent elastic constants for in-plane stresses and strains. These constants can be related to engineering constants by some considerations. If an orthotropic material is subjected to uniaxial tensile loading in the principal direction 1, σ_2 and τ_{12} are zero (Figure 2.11 (a)), from Equation (2.9) we get

$$\varepsilon_1 = S_{11}\sigma_1, \tag{2.10}$$

$$\varepsilon_2 = S_{12}\sigma_1, \tag{2.11}$$

$$\gamma_{12} = 0. \tag{2.12}$$

From engineering perspective, we have

$$\varepsilon_1 = \frac{\sigma_1}{E_1}, \tag{2.13}$$

$$\varepsilon_2 = -\frac{\upsilon_{12}}{E_1}, \tag{2.14}$$

$$\gamma_{12} = 0. \tag{2.15}$$

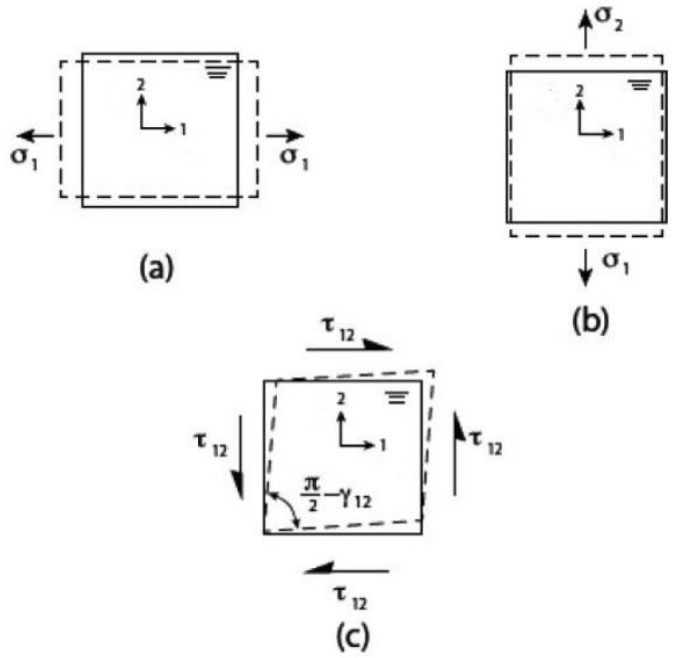

Figure 2.11. Loading condition of an orthotropic composite element (a) uniaxial tensile loading in direction 1; (b) uniaxial tensile transverse loading in direction 2; (c) pure shear loading [36].

where E_1 and υ_{12} are the effective elastic modulus and Poisson's ratio for loading in direction of 1 and plane 1-2 respectively. From Equations (2.10) - (2.15) compliance elements in Equation (2.9) can be identified as:

$$S_{11} = \frac{1}{E_1}, \tag{2.16}$$

$$S_{12} = \frac{-\upsilon_{12}}{E_1}. \tag{2.17}$$

Similarly, if the uniaxial tensile loading is in the transverse direction 2 (Figure 2.11 (b)), we have

$$S_{22} = \frac{1}{E_2}, \tag{2.18}$$

$$S_{12} = \frac{-\upsilon_{21}}{E_2}. \tag{2.19}$$

Finally, if the only loading is pure shear (Figure 2.12 (c)), τ_{12}, we only have

$$\gamma_{12} = \frac{\tau_{12}}{G_{12}}, \tag{2.20}$$

and as a result

$$S_{66} = \frac{1}{G_{12}}. \tag{2.21}$$

where G_{12} is the effective shear modulus of the composite material in the 1-2 plane.

In summary, the constants of compliance tensor can be written by engineering constants as following:

$$S_{11} = \frac{1}{E_1}, \tag{2.22}$$

$$S_{12} = \frac{-\upsilon_{12}}{E_1} = \frac{-\upsilon_{21}}{E_2}, \tag{2.23}$$

$$S_{22} = \frac{1}{E_2}, \tag{2.24}$$

$$S_{66} = \frac{1}{G_{12}}. \tag{2.25}$$

The Poisson's ratios in plane 1-2 and 2-1 are dependent by $\upsilon_{21} = \upsilon_{12}\frac{E_2}{E_1}$.

2.4.2. Classical Lamination Theory

Classical lamination theory includes a general set of mechanics of materials type of stress and deformation assumptions that leads to the force-strain-curvature and moment-strain-curvature relations. By use of this theory, the laminate properties can obtain directly from lamina's properties. This section follows ideas outlined in references [35] and [37].

The constitutive relations in principal material coordinates for an orthotropic lamina under plane stress are obtained in Equation 2.8, for other in plane coordinate system of the lamina, the relations between stress and strain can find by

$$\begin{bmatrix}\sigma_1\\ \sigma_2\\ \tau_{12}\end{bmatrix} = \begin{bmatrix}\overline{Q}_{11} & \overline{Q}_{12} & \overline{Q}_{16}\\ \overline{Q}_{12} & \overline{Q}_{22} & \overline{Q}_{26}\\ \overline{Q}_{16} & \overline{Q}_{26} & \overline{Q}_{66}\end{bmatrix}\begin{bmatrix}\varepsilon_1\\ \varepsilon_2\\ \gamma_{12}\end{bmatrix}. \tag{2.26}$$

Where, the transformed reduced stiffness matrix, $\bar{Q}_{ij}$, are obtained based on the reduced stiffness matrix and fiber angle for each ply.

$$\begin{cases}\bar{Q}_1 = Q_1\cos^4(\theta) + 2(Q_{12}+2Q_6)\sin^2(\theta)\cos^2(\theta) + Q_2\sin^4(\theta)\\ \bar{Q}_{12} = (Q_1+Q_2-4Q_6)\sin^2(\theta)\cos^2(\theta) + Q_{12}(\sin^4(\theta)+\cos^4(\theta))\\ \bar{Q}_{16} = (Q_1-Q_{12}-2Q_6)\sin(\theta)\cos^3(\theta) + (Q_{12}-Q_2+2Q_6)\sin^3(\theta)\cos(\theta)\\ \bar{Q}_2 = Q_1\sin^4(\theta) + 2(Q_{12}+2Q_6)\sin^2(\theta)\cos^2(\theta) + Q_2\cos^4(\theta)\\ \bar{Q}_{16} = (Q_1-Q_{12}-2Q_6)\sin^3(\theta)\cos(\theta) + (Q_{12}-Q_2+2Q_6)\sin(\theta)\cos^3(\theta)\\ \bar{Q}_6 = (\bar{Q}_1+\bar{Q}_2-2\bar{Q}_{12}-2\bar{Q}_6)\sin^2(\theta)\cos^2(\theta) + Q_6(\sin^4(\theta)+\cos^4(\theta))\end{cases} \tag{2.27}$$

The Equation 2.27 can consider as stress-strain relations for k^{th} ply of a laminate. Therefore, the Equation 2.27 can rewrite as

$$\{\sigma\}_k = [\bar{Q}]_k\{\varepsilon\}_k. \tag{2.28}$$

Some assumptions are considered in defining the classical lamination theory, which are:

- Laminae are perfectly bonded inside of the laminate
- The bonds are infinitesimally thin and they are not shear-deformable
- Displacements in lamina boundaries are continuous

These assumptions required $\gamma_{xz} = \gamma_{yz} = 0$ and $\varepsilon_z = 0$, where z is the direction as shown in Figure 2.12.

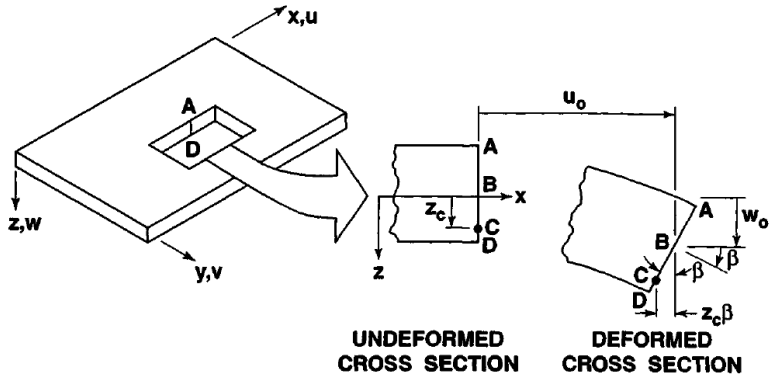

Figure 2.12. Geometry of deformation in the x-z plane of a lamina [35].

The displacements field in x, y, and z direction respectively shown as u, v, and w, and they can derive as shown in Figure 2.12 as

$$u_c = u_0 - z_c\beta. \tag{2.29}$$

where $\beta = \frac{\partial w_0}{\partial x}$ is the slope of the middle surface of laminate in the x direction and subscript '0' is used to represents middle surface values of variables. Therefore, the Equation 2.20 can be rewrite for u at any z point through the laminate thickness as

$$u = u_0 - z\frac{\partial w_0}{\partial x}. \tag{2.30}$$

And similarly, the displacement field v in the y direction can be written as

$$v = v_0 - z\frac{\partial w_0}{\partial y}. \tag{2.31}$$

Since $\varepsilon_z = \gamma_{xz} = \gamma_{yz} = 0$, the remaining strains by using linear elasticity are defined in terms of displacement.

$$\begin{cases} \varepsilon_x = \dfrac{\partial u}{\partial x} \\ \varepsilon_y = \dfrac{\partial v}{\partial y} \\ \gamma_{xy} = \dfrac{\partial u}{\partial y} + \dfrac{\partial v}{\partial x} \end{cases} \tag{2.32}$$

By using Equations 2.21 and 2.22, the strains are

$$\begin{cases} \varepsilon_x = \dfrac{\partial u_0}{\partial x} - z\dfrac{\partial^2 w_0}{\partial x^2} \\ \varepsilon_y = \dfrac{\partial v_0}{\partial y} - z\dfrac{\partial^2 w_0}{\partial y^2} \\ \gamma_{xy} = \dfrac{\partial u_0}{\partial y} + \dfrac{\partial v_0}{\partial x} - 2z\dfrac{\partial^2 w_0}{\partial x \partial y} \end{cases} \tag{2.33}$$

or in matrix form

$$\begin{bmatrix} \varepsilon_x \\ \varepsilon_y \\ \gamma_{xy} \end{bmatrix} = \begin{bmatrix} \varepsilon_x^0 \\ \varepsilon_y^0 \\ \gamma_{xy}^0 \end{bmatrix} + z\begin{bmatrix} \kappa_x \\ \kappa_y \\ \kappa_{xy} \end{bmatrix}. \tag{2.34}$$

where ε_x^0, ε_y^0, and γ_{xy}^0 are middle surface strains and κ_x, κ_x, and κ_{xy} are the middle surface curvatures. Equations 2.19 and 2.25 show that the stress variation through the laminate thickness is not always linear against the linearity of strain variation.

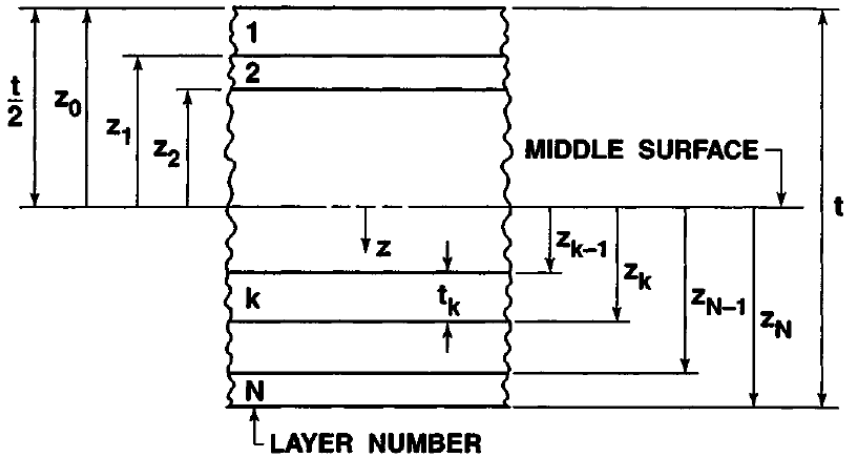

Figure 2.13. Geometry of an N-layered laminate [35].

The resultant forces and moments acting on a laminate with N layers as shown in Figure 2.13 can be get by integrating stresses in each ply over the laminate thickness and summation of these integrations.

$$\begin{bmatrix} N_x \\ N_y \\ N_{xy} \end{bmatrix} = \int_{-t/2}^{t/2} \begin{bmatrix} \sigma_x \\ \sigma_y \\ \tau_{xy} \end{bmatrix} dz = \sum_{k=1}^{N} \int_{z_{k-1}}^{z_k} \begin{bmatrix} \sigma_x \\ \sigma_y \\ \tau_{xy} \end{bmatrix} dz, \tag{2.35}$$

and

$$\begin{bmatrix} M_x \\ M_y \\ M_{xy} \end{bmatrix} = \int_{-t/2}^{t/2} \begin{bmatrix} \sigma_x \\ \sigma_y \\ \tau_{xy} \end{bmatrix} z dz = \sum_{k=1}^{N} \int_{z_{k-1}}^{z_k} \begin{bmatrix} \sigma_x \\ \sigma_y \\ \tau_{xy} \end{bmatrix} z dz, \tag{2.36}$$

where z_k is distance of k^{th} layer of laminate from middle surface of it. By integrating Equations 2.29, 2.35, 2.36, and 2.37 the forces and moments become

$$\begin{bmatrix} N_x \\ N_y \\ N_{xy} \end{bmatrix} = \sum_{k=1}^{N} \begin{bmatrix} \overline{Q}_{11} & \overline{Q}_{12} & \overline{Q}_{16} \\ \overline{Q}_{12} & \overline{Q}_{22} & \overline{Q}_{26} \\ \overline{Q}_{16} & \overline{Q}_{26} & \overline{Q}_{66} \end{bmatrix}_k \left[\int_{z_{k-1}}^{z_k} \begin{bmatrix} \varepsilon_x^0 \\ \varepsilon_y^0 \\ \gamma_{xy}^0 \end{bmatrix} dz + \int_{z_{k-1}}^{z_k} \begin{bmatrix} \kappa_x \\ \kappa_y \\ \kappa_{xy} \end{bmatrix} z dz \right], \tag{2.37}$$

$$\begin{bmatrix} M_x \\ M_y \\ M_{xy} \end{bmatrix} = \sum_{k=1}^{N} \begin{bmatrix} \overline{Q}_{11} & \overline{Q}_{12} & \overline{Q}_{16} \\ \overline{Q}_{12} & \overline{Q}_{22} & \overline{Q}_{26} \\ \overline{Q}_{16} & \overline{Q}_{26} & \overline{Q}_{66} \end{bmatrix}_k \left[\int_{z_{k-1}}^{z_k} \begin{bmatrix} \varepsilon_x^0 \\ \varepsilon_y^0 \\ \gamma_{xy}^0 \end{bmatrix} z dz + \int_{z_{k-1}}^{z_k} \begin{bmatrix} \kappa_x \\ \kappa_y \\ \kappa_{xy} \end{bmatrix} z^2 dz \right]. \tag{2.38}$$

If laminate sensitive to environmental factors such as temperature gradient and moisture gradient, the effects of them should added to Equations 2.28 and 2.29. Therefore, they written as

$$\begin{bmatrix} N_x \\ N_y \\ N_{xy} \end{bmatrix} = \begin{bmatrix} A_{11} & A_{12} & A_{16} \\ A_{12} & A_{22} & A_{26} \\ A_{16} & A_{26} & A_{66} \end{bmatrix} \begin{bmatrix} \varepsilon_x^0 \\ \varepsilon_y^0 \\ \gamma_{xy}^0 \end{bmatrix} + \begin{bmatrix} B_{11} & B_{12} & B_{16} \\ B_{12} & B_{22} & B_{26} \\ B_{16} & B_{26} & B_{66} \end{bmatrix} \begin{bmatrix} \kappa_x \\ \kappa_y \\ \kappa_{xy} \end{bmatrix}, \tag{2.39}$$

$$\begin{bmatrix} M_x \\ M_y \\ M_{xy} \end{bmatrix} = \begin{bmatrix} B_{11} & B_{12} & B_{16} \\ B_{12} & B_{22} & B_{26} \\ B_{16} & B_{26} & B_{66} \end{bmatrix} \begin{bmatrix} \varepsilon_x^0 \\ \varepsilon_y^0 \\ \gamma_{xy}^0 \end{bmatrix} + \begin{bmatrix} D_{11} & D_{12} & D_{16} \\ D_{12} & D_{22} & D_{26} \\ D_{16} & D_{26} & D_{66} \end{bmatrix} \begin{bmatrix} \kappa_x \\ \kappa_y \\ \kappa_{xy} \end{bmatrix}, \tag{2.40}$$

where

$$\begin{cases} A_{ij} = \sum_{k=1}^{N} \left(\bar{Q}_{ij}\right)_k (z_k - z_{k-1}) \\ B_{ij} = \frac{1}{2} \sum_{k=1}^{N} \left(\bar{Q}_{ij}\right)_k (z^2{}_k - z^2{}_{k-1}) \\ D_{ij} = \frac{1}{3} \sum_{k=1}^{N} \left(\bar{Q}_{ij}\right)_k (z^3{}_k - z^3{}_{k-1}) \end{cases} \tag{2.41}$$

where A_{ij}, B_{ij}, and D_{ij} are the extensional stiffness, bending-extension coupling stiffness, and bending stiffness matrix respectively.

2.4.3. Beam Theories for Composite Laminates

Beams defined as structures which one of its dimensions is much larger than the other two. The main axis of the beam is defined in longitudinal direction of the beam, and a cross-section normal to the main axis. There exist different theories for considering and analyzing beams, such as Euler-Bernoulli and Timoshenko theory. These theories well-suited for beams with isotropic materials. Generally, beam theories consists of the reduction of a three-dimensional elasticity problem to a one-dimensional one. As composite beams have become very popular in industries like automobile, aerospace, and so on. The needs for theories of composite beams get attention. In this section summary of theories for isotropic beams and composite beams is given.

2.4.3.1. Euler-Bernoulli Beam Theory.

Euler-Bernoulli beam theory also known as classical beam theory is a simplifies form of linear theory of elasticity for beams. The Euler-Bernoulli beam theory can predict the load or the deflection under flexural loading and the stress and strain field as well. There are underlying assumptions for the Euler-Bernoulli beam theory. The first one is the cross-

section of the beam is infinitely rigid in its own plane, the second is, during deformation the cross-section is assumed to remain plane, and finally, the cross-section is assumed to keep normal to the deformed axis of the beam [38]. In this theory, shear deformations are neglected and beam deflections are assumed to be single. Therefore, it is only valid for high length-thickness ratios.

The Euler-Bernoulli theory show the elastic behavior of beams by Hooke's law. The solution can be modified for composite beams by integration the lamination theory. The Euler-Bernoulli equation is related applied load and beam's deflection, and describes the relations between them as:

$$EI\frac{d^4w(x)}{dx^4} = q(x) \tag{2.42}$$

where $w(x)$ is deflection of the neutral axis, $q(x)$ is the applied load, E is the elastic modulus, and I is the second moment inertia of the beam's cross-section.

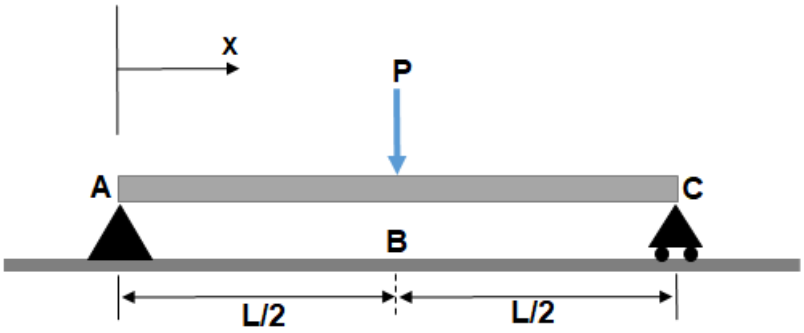

Figure 2.14. Three-point bending of beam with constant cross-section over the length.

The analytical results of maximum deflection for a three-point bending is obtained as [39]:

$$w = \frac{PL^3}{48EI} \tag{2.43}$$

where P is applied load in the middle of the beam, and L is the total length of the beam as shown in Figure 2.14.

2.4.3.2. Timoshenko Beam Theory.

The model in the Timoshenko beam theory considers shear deformation and rotational bending effects, unlike Euler-Bernoulli beam theory, and makes it well-suited for analyzing short thick beams and sandwich composite beams. Generally, Timoshenko beam theory estimates stiffness of the beam lower than theoretical value and as a result larger deflections occur. The Timoshenko equation for bending of beam with isotropic material is of forth order, but there is a second-order partial derivative. For constant cross-section isotropic beam, the Timoshenko's equation is [40]:

$$EI\frac{d^4w(x)}{dx^4} = q(x) - \frac{EI}{\kappa AG}\frac{d^2q}{dx^2} \tag{2.44}$$

Where A is the area of cross-section, G is shear modulus, and κ is shear correction factor. Shear correction factor is defined as:

$$\kappa = \frac{Average\ shear\ strain\ on\ a\ section}{Shear\ strain\ at\ the\ centroid} \tag{2.45}$$

The main difference between Euler-Bernoulli and Timoshenko beam theories is in their assumptions. In Euler-Bernoulli theory the cross-section is consider perpendicular to

the flexural line, but in the Timoshenko theory rotation is between the cross-section and flexural line is allowed, which comes from shear deformation assumption in Timoshenko theory. Therefore, the Euler-Bernoulli beam is stiffer. However, If the length-thickness ratio is large enough the error between both theories is small.

2.4.3.3. Bean Theories for Laminated Composite.

Recent advances in composite materials technology leads to the various application of laminated composite beams as an element in engineering structures. Against isotropic beams, composite beams show coupling between extensional, bending, and twisting modes of deformation. Because of this characteristic of composite beam-like structures, it is required to develop a simple and applicable analysis theory for them. The beam theory for laminated composite beams is rooted in the shear deformable laminated plate theory.

In laminated composite beams, the transverse shear deformation has great effects on the transverse displacements, the natural frequencies of vibration, and buckling loads. Euler-Bernoulli beam theory due to ignoring transverse shear deformations results in high error percentage in analyzing laminated composite beams. Beam theories for laminated composite categorized as first-order shear deformation laminate theory and higher-order laminated beam theories. First-order shear deformation laminate theory is simply Timoshenko beam theory which presumes laminate as discrete layer with constant shear strains through the thickness. Higher-order laminated beam theories derived from usage of power series expansion in the thickness coordinate of the beam and includes parabolic shear deformation theories, Lo-Christensen-Wu type higher order theories, and layerwise (discrete layer) theories [41].

Parabolic shear deformation theories are layer wise shear deformation theory which presume transverse shear stress distribution inside each layer of laminate as parabolic for symmetric cross-ply laminates. Lo-Christensen-Wu type higher order theories are included the effects of transverse normal strain and transverse displacement assigned with transverse shear deformation for laminated plates which consist of eleven displacement variables. They

are obtainable by finite element solutions. Layer wise (discrete layer) theories are particular forms of lamination theory which discussed in section 2.4.2. [41].

2.4.4. Failure Mechanism of Laminated Composites

Composite materials, especially laminated-composites, have anisotropic mechanical properties. Due to this characteristic of composite materials, the behavior of them at failure is highly related to the direction. Failure occurrence is not a single level event in composite laminates. It is a series of failure mechanisms that develop until the laminate collapse. Failure mechanism of composites can be considered in two different point of view, microscopic and macroscopic failure event. Macroscopic failure of a fiber composite is a result of one or more microscopic failure events. Microscopic failure events affect when their frequency is really high. Figure 2.15 is displayed the development of microscopic failure in a composite laminate.

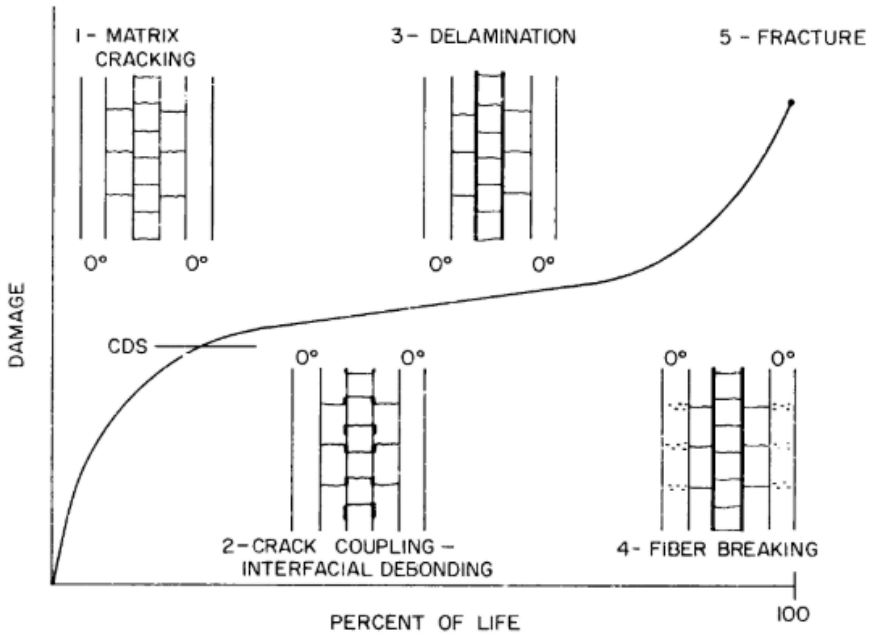

Figure 2.15. Development of damage in composite laminates until fracture [42].

Different failure modes in composite lamina strongly depends on the stress condition, tensile or compressive loading, and whether the lamina has unidirectional fibers or woven fabric (Figure 2.7). Most common failure modes under in-plane loading are fiber tensile or compressive failure, matrix tensile or compressive failure, and shear failure (Figure 2.16) [36]. Matrix cracking, debonding, delamination and fiber breaking are the main microscopic failure events in tensile loading, while kinking is usual failure mode in compressive loading. Table 2.1 presents failure of unidirectional composites based on type of loading. All failures under different loading condition are combination of microscopic failure events.

Table 2.1. Failure mechanism of unidirectional composites based on type of loading.

Failure of Unidirectional Composites					
Microscopic Failure events	**Failure under longitudinal tensile loads**	**Failure under longitudinal compressive loads**	**Failure under transverse tensile loads**	**Failure under transverse compressive loads**	**Failure under in-plane shear loads**
Breaking of fibers	Fiber breaks at its weakest cross section	Transverse tensile failure (transverse splitting	Matrix failure and/or interface failure	Matrix shear failure	Matrix shear failure
Debonding or separation of fibers and matrix at the interface	Brittle failure	Fiber micro-buckling or the local buckling of fibers		Component debonding	Component debonding
Matrix micro cracking	Brittle failure with fiber pullout	Gross shear failure		Fiber crushing	Combination of the first two failure mechanism
Fiber pullout	Brittle failure with debonding and/or matrix failure				
Delamination in laminates					

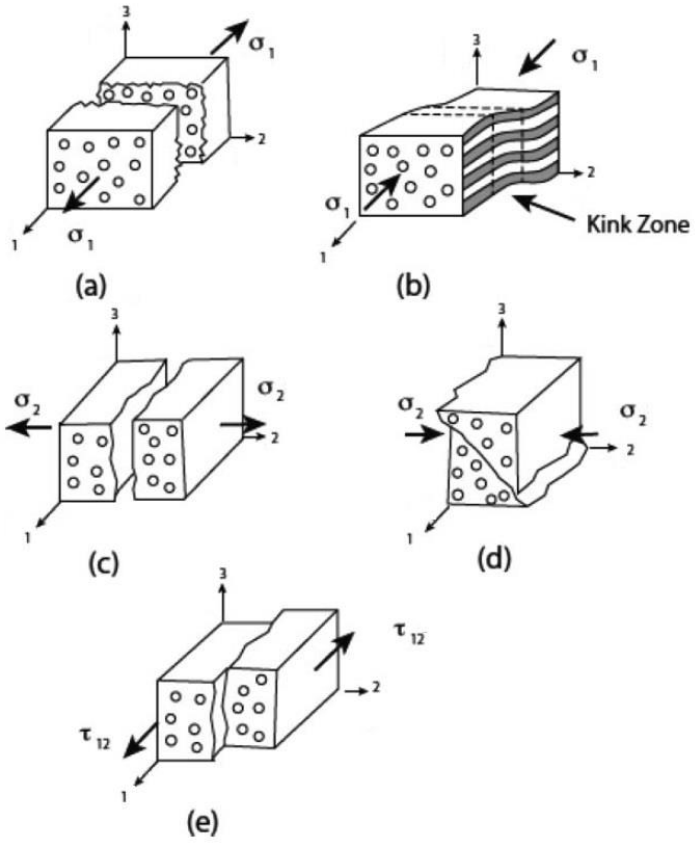

Figure 2.16. Failure modes of unidirectional composite under different loading condition (a) fiber tensile failure, (b) fiber compressive failure, (c) matrix tensile failure, (d) matrix compressive failure (e) shear failure [36].

Microscopic failure events that lead to different failure is described in following paragraphs.

1) *Matrix Cracking or Transverse Cracking*: This failure (Figure 2.16 (c-d)) is usually the first damage mechanism that occur in fiber-reinforced composites. Matrix cracking initiates in the direction of the fibers and in the thickness direction of laminate [43]. Matrix cracking commonly happens due to high stresses produced by transverse loads. It does not affect the capacity of the fibers to carrying the load, but it has effects on the mechanical and thermal properties of the structure. Matrix cracking leads to activate for further failure mechanisms and speed up environmental degradation of laminate.

2) *Debonding or Crack Coupling*: The interface between fiber and matrix in lamina is subject to separating from each other because of inherent stress. When a laminated composite is loaded transversely, stress concentration areas between fibers and matrix leads to micro-cracks due to different mechanical properties of the elements of lamina. These micro-cracks growth resulted in separation of fibers and matrix and this process called debonding. Debonding become easier in laminated composites with weaker interface between fibers and matrix.

3) *Delamination*: It is one of the well-known out-of-plane failure mechanism, which occurs when two adjacent layers separate. Delamination occurs due to bending load or fatigue loading that applied on the laminates [44]. In laminated structures, delamination commonly initiates from discontinuities of material such as cracks in matrix or imperfections od materials that resulted as manufacturing process. It can decrease the mechanical properties of the laminate such as stiffness and strength of the structure, but the presence of the delamination usually does not lead to the complete failure of the structure and sometimes it can delay the final failure of the structure since it provides stress relief [45].

4) *Fiber breaking*: Fibers in laminated composite structures are responsible for carrying loads. Therefore, fiber breaking is an important event in failure mechanism which leads to the collapse of the structures under tension (Figure 2.16(a)). A fiber in tensile loading breaks when the load is sufficiently high. In a unidirectional laminated composite more than single fiber will break and some fibers may fracture at several point along it.

5) *Kink-band*: The dominant compressive failure mode in unidirectional laminated composites is kink-band (Figure 2.17) or localized compressive buckling. The composite compression procedure triggers from elastic deformation and ends with fracture. This process can be divided into four staged as shown in Figure 2.18. At the first stage, the composite structure deformed under compressive loading uniformly. However, due to structure or loading imperfections, uniform deformation progress

into elastic instability slowly and because of low yield strength of the matrix, plastic deformation initiate in the structure. Plastic deformation causes local instability, kink-band. At the final stage by increasing the load level, the composite structure fails associated by the shear failure [47].

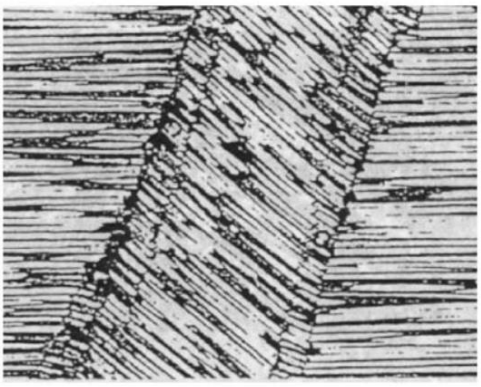

Figure 2.17. Micrography of a unidirectional composite kink-band [48].

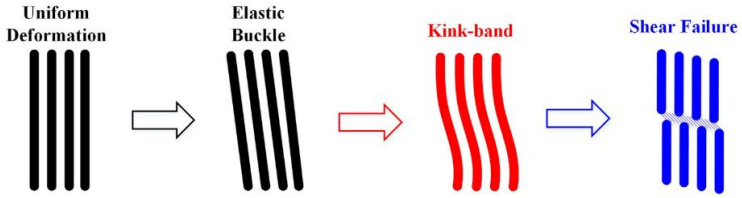

Figure 2.18. Schematic kink-band formation under compressive loading [47].

2.4.5. Failure Criteria of Laminated Composites

At the first, it should be clarified that failure criteria are not derived from any physical failure theory. Mechanics of materials failure criteria simply defined based on a stress or strain upper limit which materials fail at that level. Practically, all of them are originated from assumptions of homogeneity and linear stress-strain behavior of material during failure.

There are exist plenty of failure theories for composite structures. These theories categorized into three group. Limit or non-interactive theories (i.e. maximum stress and strain failure criteria), interactive theories (i.e. Tsai-Hill and Tsai-Wu), and partially interactive or physically based theories (i.e. Hashin-Rotem and Punk) [49].

Limit or non-interactive criteria anticipate the failure load for modes of failure by comparing stresses and strains of lamina with related strength. In the limit criteria, interaction between stresses or strains is not accounted. Interactive criteria suppose that all the stress components have effect on the failure of composite at the same time. Partially interactive or physically based criteria consider matrix and fiber failure mode separately [50].

The reliability and applicability of each failure criterion rigorously depend on the its ease to apply and compatibility of the result with valid experimental data, that makes it somehow hard to decide selecting one theory between others. Commonly, there are four widely used failure criteria for laminated-composite materials which described as following. These criteria are based on the hypothesis that laminated fiber composites are orthotropic continua.

2.4.5.1. Maximum Stress Failure Criterion.

The maximum stress failure criterion is usually based on the uniaxial strength and stress in the principle material coordinate (Figure 2.19) of a unidirectional lamina. Failure is predicted when one of the following conditions is satisfied:

$$\sigma_1 \geq X_t \quad \text{or} \quad \sigma_2 \geq Y_t \qquad \text{(For tensile stresses)} \qquad (2.46)$$

$$\sigma_1 \leq -X_c \quad \text{or} \quad \sigma_2 \leq -Y_c \qquad \text{(For compressive stresses)} \qquad (2.47)$$

$$|\tau_{12}| \geq S_{12} \qquad \text{(For shearing stress)} \qquad (2.48)$$

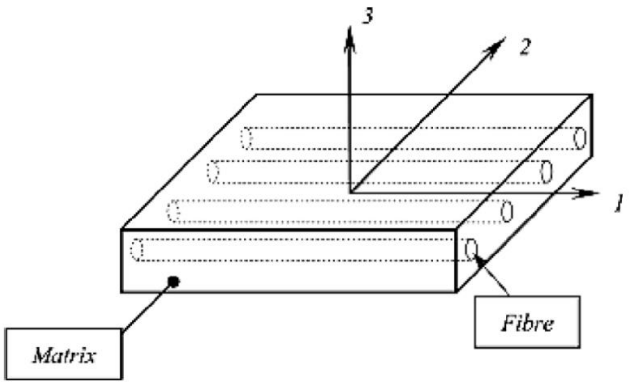

Figure 2.19. Principal material coordinates of a typical lamina [51].

For a two-dimensional state of stress with $\tau_{12} = 0$, in a unidirectional lamina, the maximum stress failure criterion region has the form of a rectangle as shown in Figure 2.20.

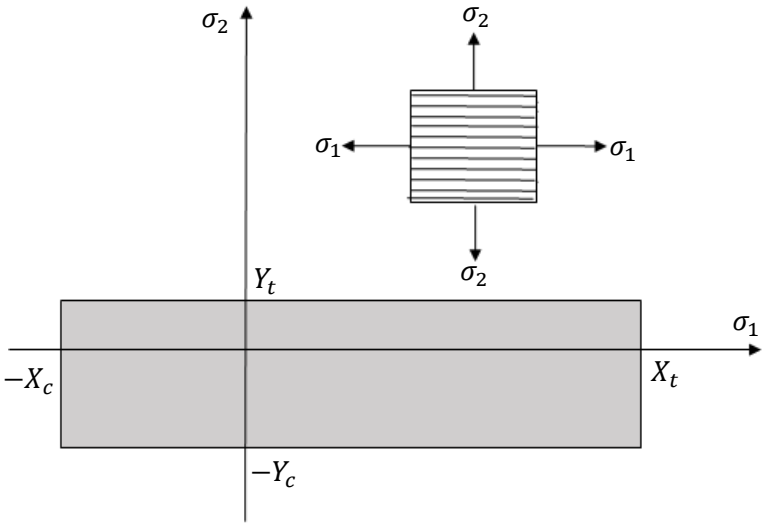

Figure 2.20. Failure region for unidirectional lamina under biaxial normal loading in maximum stress theory.

Due to its simplicity, there are wide application of this failure criterion. Absence of interaction between the stress components which is normally observed in the experiments is one of the great pitfalls of this failure criterion [52].

2.4.5.2. Maximum Strain Failure Criterion.

The maximum strain failure criterion is an alternative to the maximum stress failure criteria. Failure occurs when one of the strain components along the principal material coordinates goes over the ultimate strain in the same direction. It can be expressed mathematically in the form of following equations:

$$\epsilon_1 \geq \epsilon_{1t}^u \quad \text{or} \quad \epsilon_2 \geq \epsilon_{2t}^u \qquad \text{(For tensile stresses)} \qquad (2.49)$$

$$\epsilon_1 \leq -\epsilon_{1c}^u \quad \text{or} \quad \epsilon_2 \leq -\epsilon_{2c}^u \qquad \text{(For compressive stresses)} \qquad (2.50)$$

$$|\gamma_{12}| \geq \gamma_{12}^u \qquad \text{(For shearing stress)} \qquad (2.51)$$

For a two-dimensional state of stress with $\tau_{12} = 0$, in a unidirectional lamina, the maximum strain failure criterion region has the form of a parallelogram as shown in Figure 2.21.

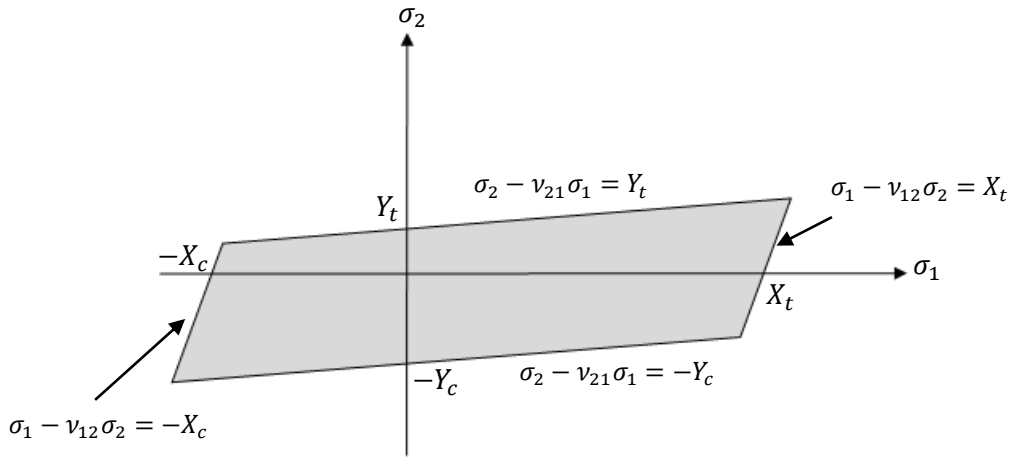

Figure 2.21. Failure region for unidirectional lamina under biaxial normal loading in maximum strain theory.

2.4.5.3. Tsai-Hill Failure Criterion.

This failure criterion also known as the deviatoric strain or distortional energy theory. The deviatoric or distortional energy has been suggested by numerous researchers such as von Mises in different forms as a failure criterion for isotropic metals [33]. Hill [53] adjusted it for the anisotropic ductile metals. Azzi and Tsai [54] modified it to orthotropic composite materials. The Tsai-Hill criterion is a modified form of von Mises yield criterion. Following equations describes Tsai-Hill failure criterion for a case of plane stress.

$$\frac{\sigma_1^2}{X^2} - \frac{\sigma_1\sigma_2}{X^2} + \frac{\sigma_2^2}{Y^2} + \frac{\tau_{12}^2}{S_{12}^2} = 1 \tag{2.52}$$

where,

$$X = X_t \text{ for } \sigma_1 > 0 \quad \text{and} \quad X = -X_c \text{ for } \sigma_1 < 0 \tag{2.53}$$

$$Y = Y_t \text{ for } \sigma_2 > 0 \quad \text{and} \quad Y = -Y_c \text{ for } \sigma_2 < 0 \tag{2.54}$$

The Tsai-Hill failure criterion, against maximum stress and maximum strain failure criterion, proposed a single criterion instead of several sub-criteria. Additionally, it permits appreciable interchange between stress components.

2.4.5.4. Tsai-Wu Failure Criterion.

Tsai-Wu failure criterion is a more general form of Tsai-Hill failure criterion. It is get from von Mises yield criterion like Tsai-Hill. Tsai-Wu failure criterion is tried to give a general failure theory for anisotropic materials without previous theories drawbacks. Tsai-Wu failure criterion is operationally simple and easily compliant to computational procedures. Its equation takes the form

$$\frac{\sigma_1^2}{X_t X_c} + \frac{\sigma_2^2}{Y_t Y_c} + \frac{\tau_{12}^2}{S_{12}^2} + 2F_{12}\sigma_1\sigma_2 + \frac{\sigma_1}{X_t} - \frac{\sigma_1}{X_c} + \frac{\sigma_1}{Y_t} - \frac{\sigma_1}{Y_c} = 1 \quad (2.55)$$

where F_{12} accounts for the interaction among σ_1 and σ_2. Because of this the Tsai-Wu failure criterion needs biaxial test results.

Table 2.2 gives a summary of the four failure criteria and compare them base on physical basis, operational convenience, and required experimental input.

For fiber-dominated laminates composites, maximum stress and maximum strain criteria exhibits better performance than others. They are not sensitive to variations in matrix strengths which obtaining them is so difficult. On the other hand, for matrix-dominated laminates, Tsai-Hill and Tsai-Wu failure criteria are sensitive to variations in matrix strengths. Due to interaction between stress components, sudden changing of failure modes results in the fitful failure region [50]. Figure 2.22 shows the failure regions for unidirectional lamina under biaxial normal loading which obtained by different criteria. Additionally, Figure 2.23 exhibits the failure regions for same lamina under transverse normal and shear loading.

Table 2.2. Comparison of Failure Criteria [33].

Theory	Physical basis	Operational convenience	Required experimental input
Maximum stress	Tensile behavior of brittle material No stress interaction	Inconvenient	Few parameters by simple testing
Maximum strain	Tensile behavior of brittle material Some stress interaction	Inconvenient	Few parameters by simple testing
Tsai-Hill	Ductile behavior of anisotropic materials "Curve fitting" for heterogeneous brittle composites	Can be programmed Different functions required for tensile and compressive strengths	Biaxial testing is needed in addition to uniaxial testing
Tsai-Wu	Mathematically consistent Reliable "curve fitting"	General and comprehensive Operationally simple	Numerous parameters Comprehensive experimental program needed

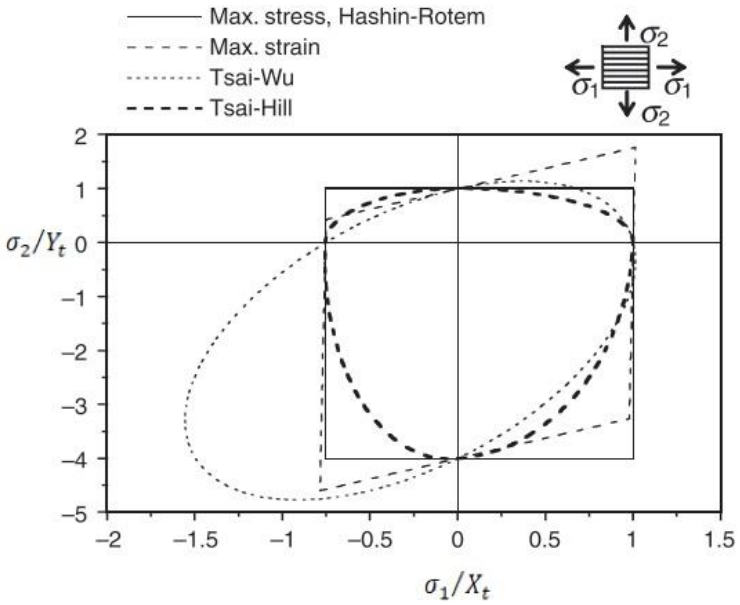

Figure 2.22. Failure regions for unidirectional lamina under biaxial loading [49].

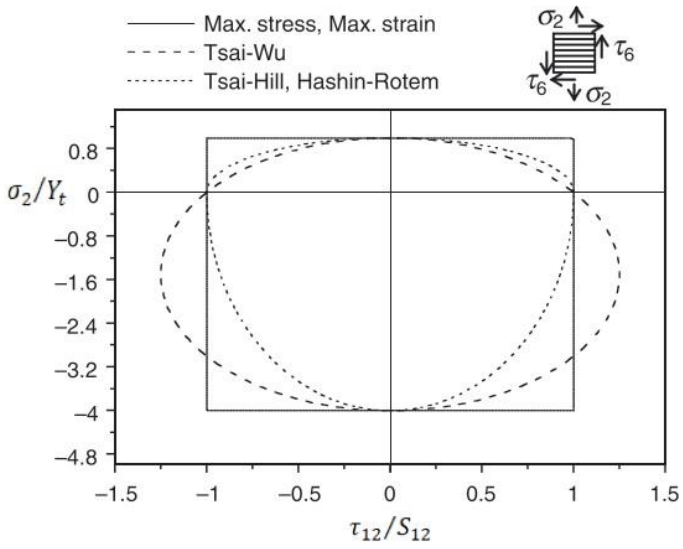

Figure 2.23. Failure regions for unidirectional lamina under transverse normal and shear loading [49].

2.5. Finite Element Method

Prediction of mechanical behaviors of engineering structures has a great importance during design, fabrication, and operation of the system. The finite element method (FEM) was basically developed for analysis of structural mechanic's problems. The finite element method is broadly used method for solving problems in engineering field. The finite element method starts by discretizing physical geometric domain into a number of smaller elements. These small parts called finite elements. Each sub-domain is solved individually and the results combined to reach the final solution of physical geometric domain. FEM is used to simulating realistic problems in computers which leads to reducing cost (time and money) of the manufacturing and testing the structure. Because of different sectors in industries, various finite element modeling software developed to meet the demands.

The FEM procedure of analyzing a model consists of four steps, modeling of the geometry, meshing, specifying of material property, and specifying of boundary, initial, and loading conditions. Several types of analysis can be handled by the finite element modeling software, such as static, dynamic, buckling and so on. Each analysis type can be applied linearly or nonlinearly as before mentioned in buckling analysis type section.

In this method, against traditional methods, we formulate mathematical equations for each finite elements and gather them to get a final solution for the entire system. Generally, there are two approaches affiliated with this method in structural mechanic's problems. One approach is the force or flexibility method and the other one is displacement or stiffness method. The first approach uses internal forces as the unknowns, and the second one uses the displacement if the nodes as the unknowns in equilibrium and compatibility equations of the problem [55].

It has been shown [56] that, for computational engineering purposes, the second approach, displacement or stiffness method, is more advantageous due to its simple

formulation for structural problems. Additionally, most of the commercial finite element programs have integrated this approach for solving structural problems.

The most common methods used for solving finite element equations are Newton-Raphson method and the Arc-Length method. Load controlled Newton-Raphson method was one of the earliest methods, but it fails in vicinity of convergence points. To vanquish this pitfall, displacement controlled algorithms were developed. However, for structures with snap-through or snap-back behavior, these algorithms fail. Another method to overcome this difficulty is developing a procedure to shift between load and displacement controls by giving up the equilibrium iterations in the neighborhood of convergence point. As a result, the Arc-Length method introduced by Riks and Wempner for structural analysis [57].

Against load controlled or displacement controlled algorithms in which the load or displacement increments are kept fixed during the analysis, the Arc-Length method is modified the load increment or load factor for each iteration. Because of this modification solver goes through some distinct path until solution converges.

In some non-linear analysis such as non-linear buckling analysis, Newton-Raphson method is resulting in convergence difficulties. The Arc-Length method unlike Newton-Raphson method is very useful in solving non-linear equations system.

2.6. Optimization Method

Optimization basically is selecting the best design among the numerous available means. The main goal of the optimization is to minimize a function, namely objective function, that subjected to some constraints. Generally, there exists three types of optimization:

- Size or cross sectional optimization
- Topology optimization
- Geometric or shape optimization

Type of the optimization directly related to the design variables. In this thesis, the optimization process done through topology optimization.

Additionally, there are two different optimization methods, Gradient-based and Heuristic methods. Gradient-based optimization methods such as steepest descent, quasi newton, and conjugate gradient, against Heuristic methods utilize gradient data of objective function and constraint to find the optimum solution of the problems. Gradient-based optimization techniques included linear programming (LP), non-linear programming (NLP), and dynamic programming (DP). However, they have several drawbacks which involve that they can only find a local optimum, they have complicated algorithms that are difficult to use efficiently, and they have difficulty in solving discrete optimization problems [59]. Because of these drawbacks another types of algorithms, Heuristic optimization approaches, generated. Heuristic approaches are usually used to solve complicated optimization problems that are difficult to solve with Gradient-based approaches. The most common Heuristic approaches include simulated annealing, tabu search, genetic algorithm, evolutionary algorithms, and so on [60].

In the last decades, fiber reinforces polymer composite (FRPC) materials has been used in many engineering applications. In the absence of the design standards for the fiber

reinforced composite structures in the field of engineering, the optimization methods and finite element analysis have a great effect on design of acceptable structures.

The design of fiber reinforced composite structures is not end with their size or geometric design, the material and their composition should be in the process of designing structures too. The optimization process of composite structures is a complex process due to large set of design variables. Because of this reason, composite material optimization process usually cannot handle by the Gradient-based optimization algorithms. Optimization methods that used generally in fiber composite design are [61]:

1) Design Sensitivity Analysis (DSA)

Design Sensitivity method has been used mainly in automotive applications. This method needs the calculation of the gradient of the objective function and the constraints with respect to design variables of the problem

2) Genetic Algorithm (GA)

Because of it capability to deal with complex and vast design variables problems, Genetic Algorithm has been used widely in the optimization of structure designs. GA are typically used to get high-quality solutions. John Holland presented GA in 1960 based on the Darwin's theory of evolution concept; later, David E. Goldberg developed GA in 1989 [62].

3) Simulated Annealing Method (SA)

Simulated annealing is an approach for finding solution of unconstrained optimization problems. This approach imitates the process of heating a solid and then decreasing the temperature slowly and in controlled way to lower defects, and consequently minimizing the energy of the system. We discuss thoroughly about this in later sections.

4) Reliability Based Design Optimization (RBDO)

Reliability Based Design Optimization is developed for solving the problem with reliability constraints. The RBDO approach incorporated two optimization method at the same time. The first one is seeking the feasible solution in an original random space, and the second one change the probability distribution into nonlinear mapping and finds the optimum solution within standard random space [63]. RBDO considers the uncertainty of the optimization design in fiber reinforced composite structure problems.

5) Particle Swarm Optimization Algorithm (PSOA)

Particle Swarm Optimization Algorithm is similar to the Genetic Algorithm method, but rather than focusing on a single individual execution, a numerous of individuals, called swarm, is considered instead. PSOA is based on swarm intelligence. The population move around trying to find a potential solution.

6) Ant Colony Optimization (ACO)

Ant Colony Optimization method is based on the ant's capability to find the shortest path from food resource to their colony. An ant wanders randomly from one place to another to finally reach the destination. The primary algorithm is based on the swarm intelligence to solve the complex problems. In ACO, against GA, artificial ants try to set up the solution step by step.

7) Multi-objective Robust Design Optimization (MRDO)

There are other optimization methods that used in the design of fiber reinforced composite structures, but the prominent ones mentioned.

2.6.1. Modified Simulated Annealing

Consider a Travelling Salesman Problem [64] with a vast number of cities. Searching among a giant number of potential solutions to seek the optimum one can be an adversity. The number of potential solutions can be numerous. Because of this, solution that is close enough to optimum solution is satisfying. As a result, we need a approach or algorithm that can get a good enough solution in a rational amount of time with lower cost. One of the most suited algorithm to these conditions is Simulated Annealing Algorithm.

Simulated Annealing is well known local search heuristic approach that used to solve discrete and continuous optimization problems [65]. Simulate Annealing is gained its name due to its similarity to the process of physical annealing process in metallurgy. This process involves heating solid until it reaches its melting point, and slowly cooled down it in a controlled cooling behavior to increase the crystallic size and minimize their defects.

The final properties of the material strongly depend on the cooling process that applied. Different designs of the optimization problem represent different positioning of the atoms. The cost of a design represents the lowest energy state [66].

Simulated Annealing Algorithm process starts with setting a temperature variable to simulate the heating process. Simulated Annealing Algorithm will assign it a high initial value to generate a random initial solution and then slowly lower the temperature. As the algorithm run it will frequently accept solutions which are worse than our current solution as long as this temperature variable is high. By doing this, algorithm allow itself to pass over any local optimums. The possibility of accepting worse solutions will decrease as the temperature become lower. Because of this, algorithm is slowly focus on an area of search space in which a solution that is close to optimum one can be found.

The prominent advantages of using this approach can be sorted as follows [67]:

- A mathematical model is not required
- It does not require gradient information of objective function and constraints
- It is not easily tricked by local optimum point
- It can solve highly non-linear optimization problems with large number of constraints

3. FINITE ELEMENT MODELING

Finite element method (FEM) is a preferred and efficient numerical technique for analyzing structure behaviors. Numerical techniques help to solve complex engineering problems by simulating real-world structures that cannot be analyzed using. analytical methods.

In this study, the mechanical behavior of I-beam is analyzed by developing a FE model using ANSYS Mechanical APDL (ANSYS Parametric Design Language), which is a powerful commercial CAE software that can perform various complicated engineering analyses in different fields. ANSYS is capable of analyzing geometrically linear or non-linear problems associated with small or large displacement by considering material or geometric linearity or non-linearity. The key steps to construct a finite element model in ANSYS APDL software are

- Initialization of the program
- Specifying the analysis type
- Defining the material property
- Specifying the element type
- Defining the key points of geometry
- Creating the area or volume by using the pre-defined key points
- Generating finite element (FE) mesh
- Applying suitable boundary conditions
- Getting the result

3.1. General Design Parameters of I-beam

The main objective of this thesis is to develop optimized design of composite I-beams with rib-reinforced web part under three-point bending load condition. The beam is simply supported. Suitable values for general dimensions of web/flanges width and thickness are chosen by a parametric study and optimization is performed for shape of the ribs on the web.

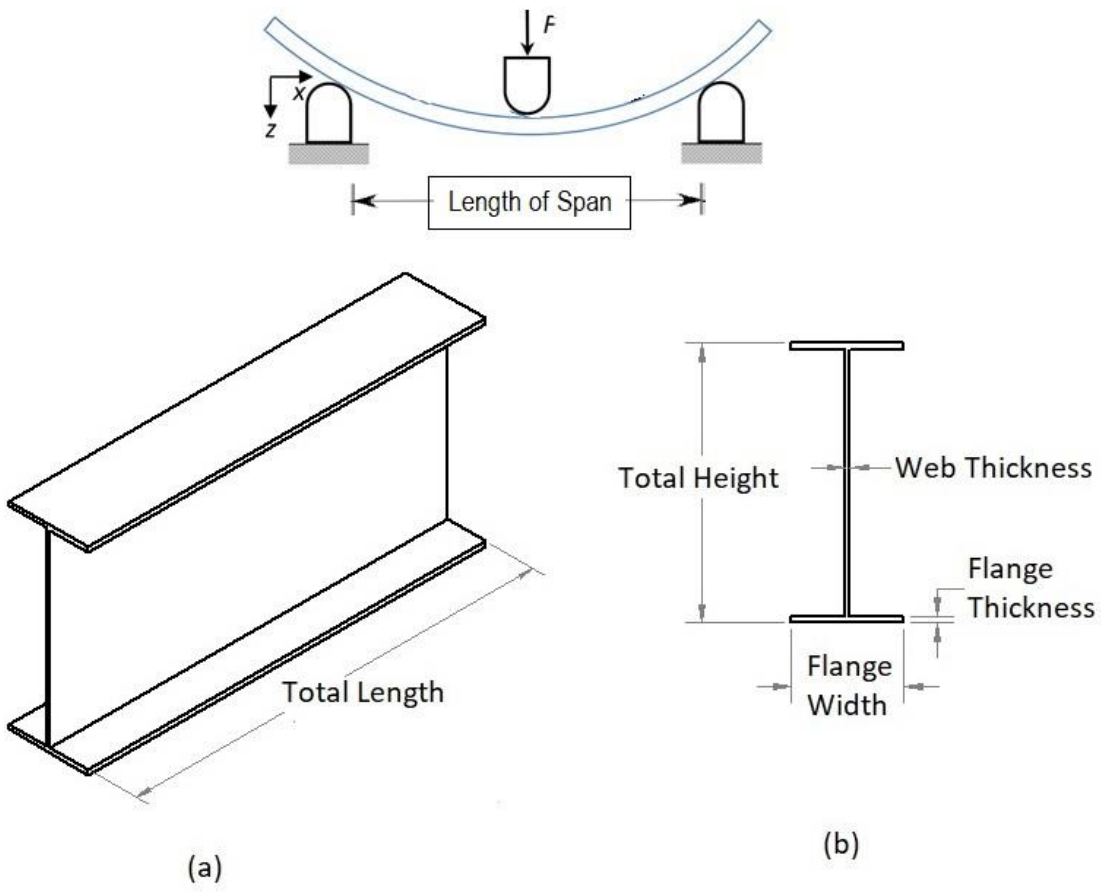

Figure 3.1. A schematic of an I-beam under three-point bending, (a) isometric view (b) cross-sectional view.

The general dimensions of I-beam are defined by its length, L_b, total height, H_b, thickness of the web, t_c, thickness of the flanges, t_s, and width of the beam, L_1, as shown in

Figure 3.1. The dimensions defined within are given in Table 3.1. All the dimensions are specified parametrically which make them capable to change easily inside the code.

Table 3.1. The general dimensions of the I-beam.

Total Height, H_b	500 [mm]
Flange Thickness, t_s	12 [mm]
Web Thickness, t_c	2 [mm]
Total Length, L_b	2400 [mm]
Width of Flange, L_1	200 [mm]
Length of Span, L	2000 [mm]

At first, the areas of the structure are defined then the shell elements are defined in two-dimension (2D), then section properties such as number of plies and fiber orientation in each layer are defined. ANSYS gives three offset options for shells thickness which are top, middle, and bottom. The whole thickness created towards up or down when top or bottom options are selected, respectively for a shell element. Otherwise, if the middle option is chosen for that element, the total defined thickness is separated equally and created in both sides of the element. As shown in Figure 3.2, the shell thickness offsets are specified as top and bottom for top flange or bottom flange, respectively, and middle for the web part of the I-beam. The shell element will be explained in detail in the next section.

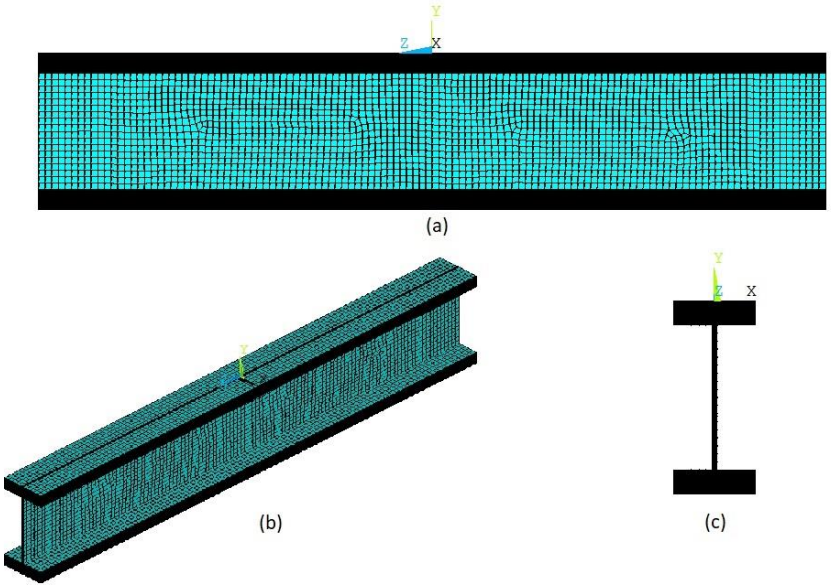

Figure 3.2. Shell thickness offset of I-beam. (a) Right view, (b) isometric view (c) front view.

3.2. Element Type

Considering that I-beams have high width-to-thickness ratio, they can be modelled by shell elements to reduce the computational time of analysis. Main goal of using shell elements are their suitability for structural applications as one direction thickness is considered to be small than the other. As a result, plane stress condition is imposed, allowing reduced number of degrees of freedom and computational time.

Considering that I-beams have high width-to-thickness ratio, they can be modelled by shell elements to reduce the computational time of analyses. This study analyzes a continuous fiber-reinforced laminated structure. ANSYS provides two different shell elements, SHELL-181 and SHELL-281 (Figure 3.3). They are both suitable to use in this study, since both elements support orthotropic material properties for structural analysis and they are capable of analyzing thin to moderately- thick shell structures. SHELL-181 is a four-node element and SHELL-281 is an eight-node element. Both have six degrees of freedom (displacements in x, y, and z directions, and rotations about x, y, and z axes) at each

node. Both of them are compatible for linear, large rotation, and/or large strain non-linear applications [68].

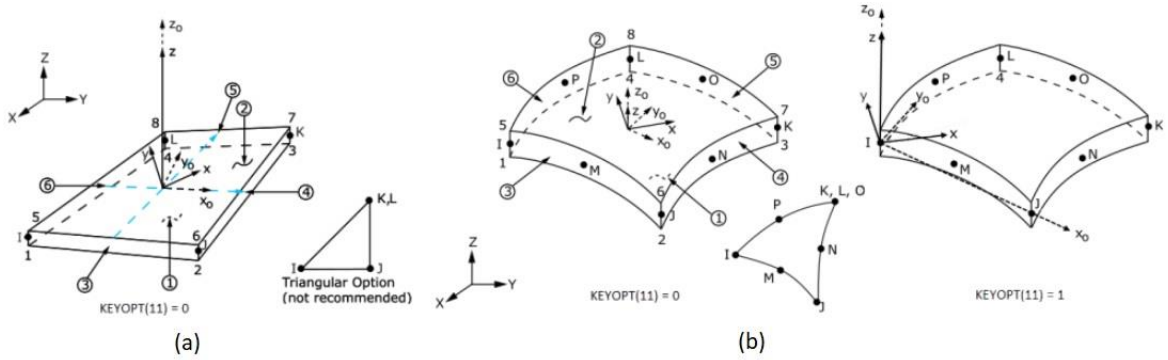

Figure 3.3. Geometry, node locations, and the coordinate system related to each element for (a) SHELL-181 and (b) SHELL-281 [68].

These shell elements can be used for analyzing layered structures made of composite materials. They are based on the first-order shear deformation theory. The only difference between them is in the number of nodes which has a great effect on analysis time.

In this study, SHELL-181 is selected as the element type due to reduced analysis time. SHELL-281 element with eight-node is appropriate to accurately determine the stress state in complex shaped structure unlike I-beams.

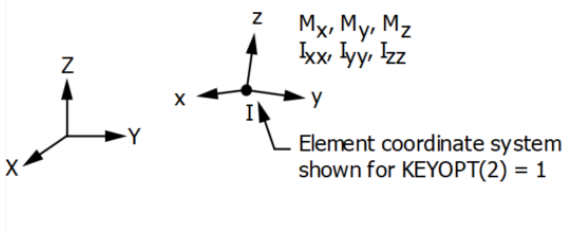

Figure 3.4. MASS21 element type [68].

Additionally, in this study another element type is used to define constraint equation and loading condition. This element type is MASS21, which stands for structural mass. MASS21 is a point element that has six DOFs, displacements in x, y, and z directions and rotations about x, y, and z axes. Definition of MASS21 element does not have any effect on static analysis solution [68]. Figure 3.4 depicts this element type.

3.3. Material Properties

In this study, IM7/8522 CFRP is chosen for the I-beam. Kaddour et al. [70] gave detailed and complete information about mechanical properties of this material. IM7/8552 CFRP's mechanical properties are given in Table 3.2. Ply thickness is 0.125 mm and the density of material is 1600 Kg/m^3 [70].

Table 3.2. Mechanical properties of IM7/8552 laminae [70].

Parameter	**Value**
Fiber Volume Fraction V_f [%]	60
Longitudinal Modulus E_1 [GPa]	165
Transverse Modulus E_2 [GPa]	9
Through-Thickness Modulus E_3 [GPa]	9
In-Plane Shear Modulus G_{12} [GPa]	5.6
Transverse Shear Modulus G_{13} [GPa]	5.6
Through-Thickness Shear Modulus G_{23} [GPa]	2.8
Major Poisson's Ratio υ_{12}	0.34
Major Transverse Poisson's Ratio υ_{13}	0.34
Through-Thickness Poisson's Ratio υ_{23}	0.5
Longitudinal Tensile Strength σ_{1t} [MPa]	2560
Longitudinal Compressive Strength σ_{1c} [MPa]	1590
Transverse Tensile Strength σ_{2t} [MPa]	73
Transverse Compressive Strength σ_{2c} [MPa]	185
Through-Thickness Tensile Strength σ_{3t} [MPa]	63
Through-Thickness Compressive Strength σ_{3c} [MPa]	185
In-Plane Shear Strength τ_{12} [MPa]	90
Transverse Shear Strength τ_{13} [MPa]	90
Through-Thickness Shear Strength τ_{23} [MPa]	57
Longitudinal Tensile Failure Strain ε_{1t} [%]	1.551
Longitudinal Compressive Failure Strain ε_{1c} [%]	1.1
Transverse Tensile Failure Strain ε_{2t} [%]	0.81
Transverse Compressive Failure Strain ε_{2c} [%]	3.2
Through-Thickness Tensile Failure Strain ε_{3t} [%]	0.7
Through-Thickness Compressive Failure Strain ε_{3c} [%]	3.2
In-Plane Shear Failure Strain γ_{12}^{u} [%]	5
Transverse Shear Failure Strain γ_{13}^{u} [%]	5
Through-Thickness Shear Failure Strain γ_{23}^{u} [%]	2.1

As mentioned in Chapter 2, compressive and tensile normal stresses develop in the top flange and bottom flange of an I-beam in three-point bending, respectively, which are the results of section bending moment arising due to the transverse forces (Figure 2.7.). Consequently, flanges should consist of primarily 0° plies to withstand normal stresses in the axial direction of the beam. On the other hand, the web part of the I-beam under transverse loading experience shear stresses (Figure 2.7.). According to Fleuret et al. [71] the layers of this part should consist of plies with ±45° orientations of fibers for improved buckling strength.

In this thesis, the dimension given in Table 3.1 and the number of plies and layup sequences given in Table 3.2 are taken constant. The schematic representations of the lay-ups of each ply cluster are shown in Figure 3.5 and Figure 3.6.

Table 3.3. Configurations and lay-up of used materials

	Flanges	**Web**
Lay-up	$[+45°/0°/-45°/0°]_s$	$[+45°/-45°]_s$
Number of Plies	96	16
Thickness [mm]	12	2

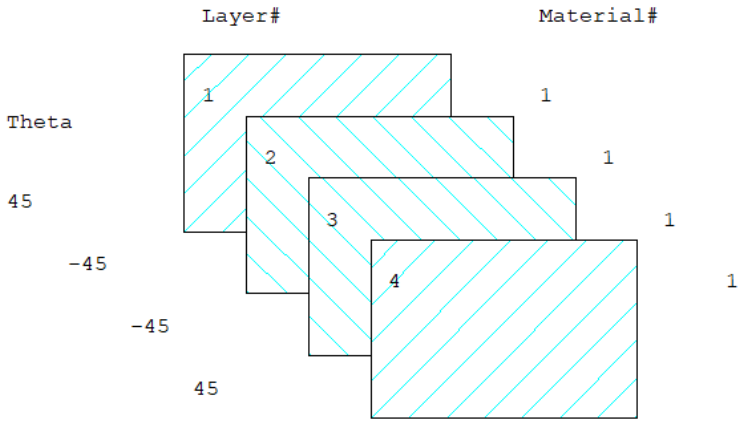

Figure 3.5. Stacking sequences of each ply cluster of the web.

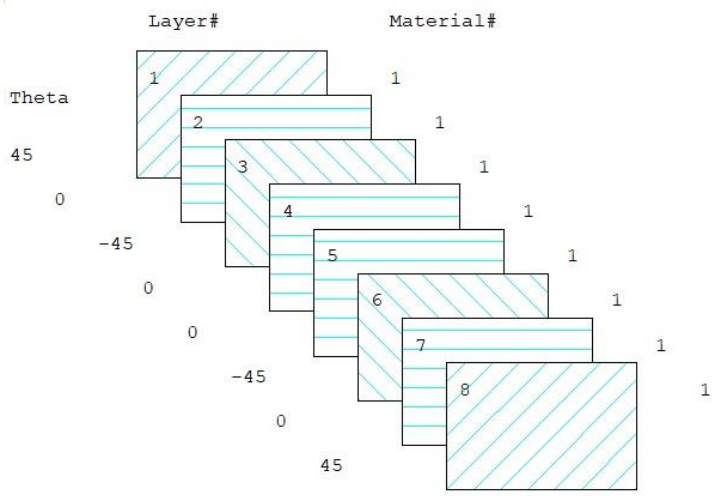

Figure 3.6. Stacking sequences of each ply cluster of the flanges.

3.4. Meshing

After creating the model geometry, and assigning the material properties to the model, the next step is to generate the finite element meshes. In finite element modelling, meshing is an indispensable stage of modeling. In the meshing procedure, the mesh type, size, and shape are the important factors, since they are directly related to the accuracy and computational time of the analysis.

Fine meshes result in accurate outcomes, but increase the cost of analysis. On the other hand, coarse meshes lead to inaccurate and untrustworthy results, but yield results in a shorter time [72].

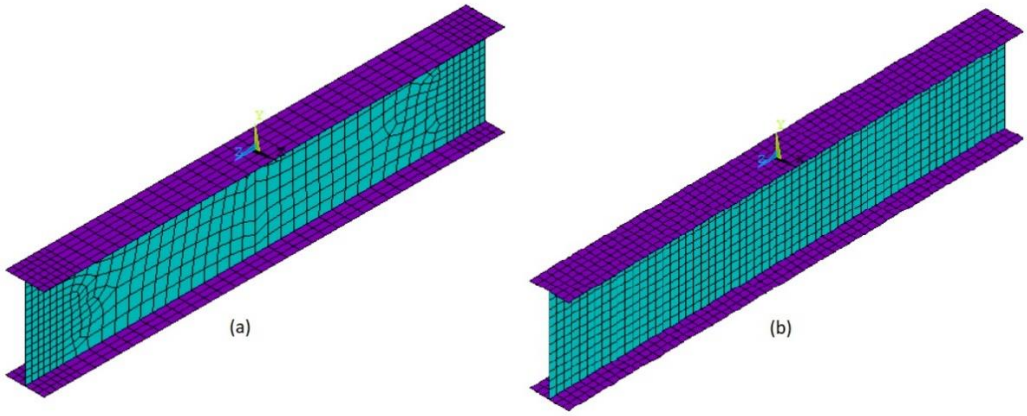

Figure 3.7. (a) Free mesh vs. (b) Mapped mesh.

There are two main meshing methods in ANSYS APDL, which is free and mapped mesh. Each one has its own disadvantages and advantages over another. In free mesh, there is not any restriction on the shape of elements, and mesh does not follow any pre-defined pattern, which makes it well-suited for models with complex shape. On the other hand, mapped mesh restricts element shapes to quadrilaterals and hexahedra for areas and volumes, respectively, which are the more accurate compared to triangular or tetrahedral elements. However, it is applicable to relatively simple geometries. Figure 3.7 gives a comparison between mapped and free mesh.

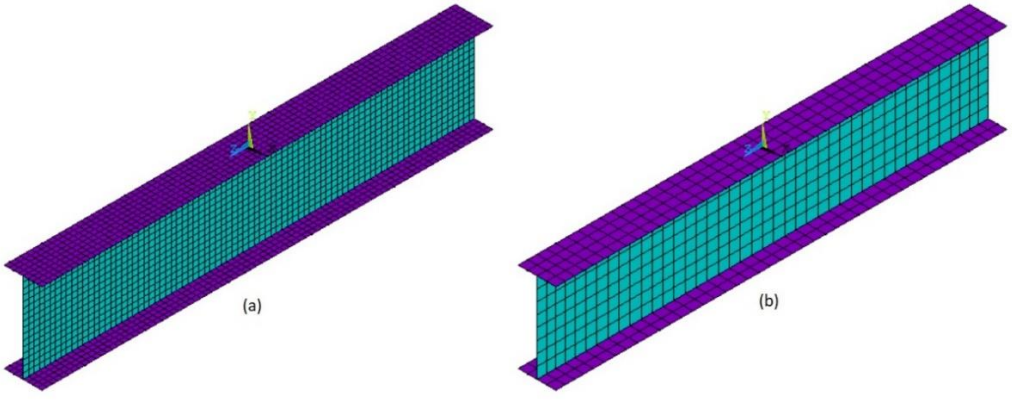

Figure 3.8. Two different mesh size for Finite Element Model (a) mesh size=30[mm] (b) mesh size=60[mm].

In this study, mapped mesh and free mesh methods are applied. Mesh convergence and model validation are discussed in next chapter.

3.5. Boundary Conditions

The boundary condition in a finite element model represent the external effects on the structure in terms of the applied forces and displacements. Accurate representation of the external effects is necessary for predicting the actual response of the structure.

The boundary conditions can be applied to key-points, lines, areas, nodes, and elements. For a particular node in a finite element model, either load or displacement can be applied, but not both of them.

In this study, a rib-reinforced I-beam under three-point bending condition is considered; therefore, it is necessary to apply suitable boundary conditions simulating the loading condition in three-point bending test. As shown in Figure 2.1, the specimen under three-point bending test is rigidly constrained in the transverse direction at the bottom at both ends. Then, the nodes at these locations are restricted from movement in the Y direction (UY=0). Because there is no force applied along the width direction, friction forces are sufficient to prevent movement in this direction in real test conditions. Accordingly, movement in the X direction is also restrained in these nodes (UX=0). In real tests, there is no restriction along the longitudinal direction of specimen, but in FE modeling, rigid motion must be prevented. Accordingly, in the longitudinal direction of the beam (UZ=0). Rotational degrees of freedom are not restrained since the specimen undergoes bending during the test. Additionally, for the top flanges two constraints, movement in the X direction and rotation about the Z direction is restrained to prevent the I-beam experiences torsional-lateral buckling.

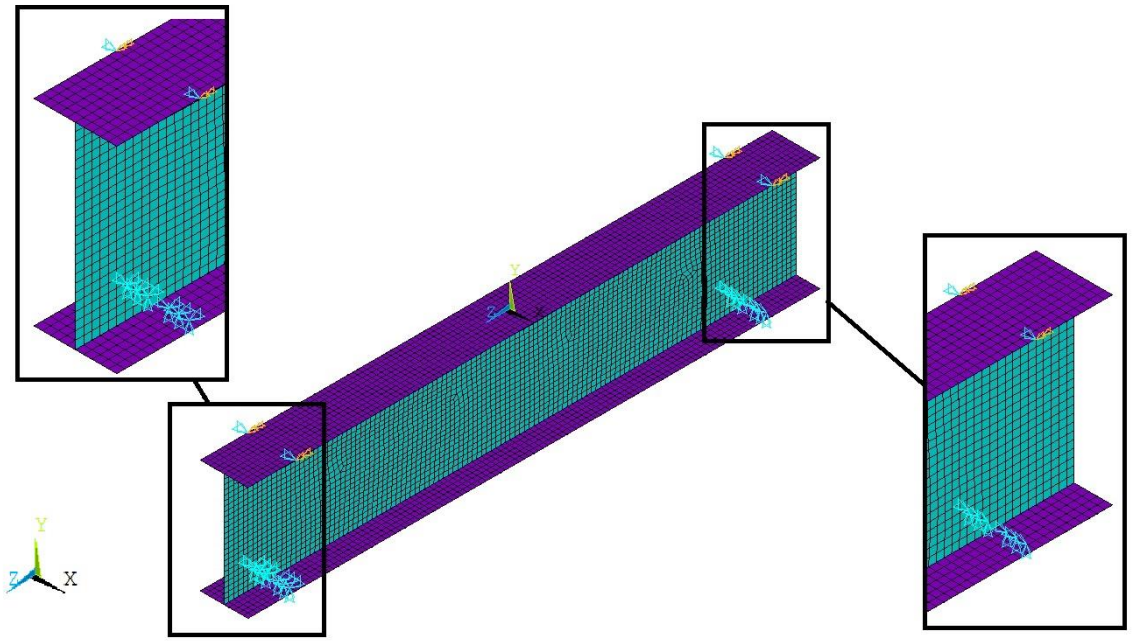

Figure 3.9. Boundary conditions of finite element model.

3.5.1. Constraint Equations

Constraint equations are equations defined to relate and restrict the value of slave nodes or elements degrees of freedom (DOF) to the value of reference node. Generally, there exist three types of constraint equations:

- Constraints Equations (CEs)
- Couples (CP)
- Multipoint Constraint (MPC)

The CEs are generally imposed to the model to establish a connection between DOFs of system. CP is an equation that makes all DOFs equal to each other at a specified node. In other words, CP constraints the movement of group of elements to be the same as the movement of a reference or master point. CP is a special kind of the CE. MPCs are an advanced feature of an analysis system which allow to tie and relate different nodes and DOFs together in the system.

The applications of these kind of equations are

1) To replace parts of the structures which are not modeled
2) Restricting meshes which haven't same sizes and geometries
3) To apply distributed loads and constraints
4) Generating rigid regions

As in this study, the roller which introduce the loading to the structure is omitted, the constraint equations are used for replacing it.

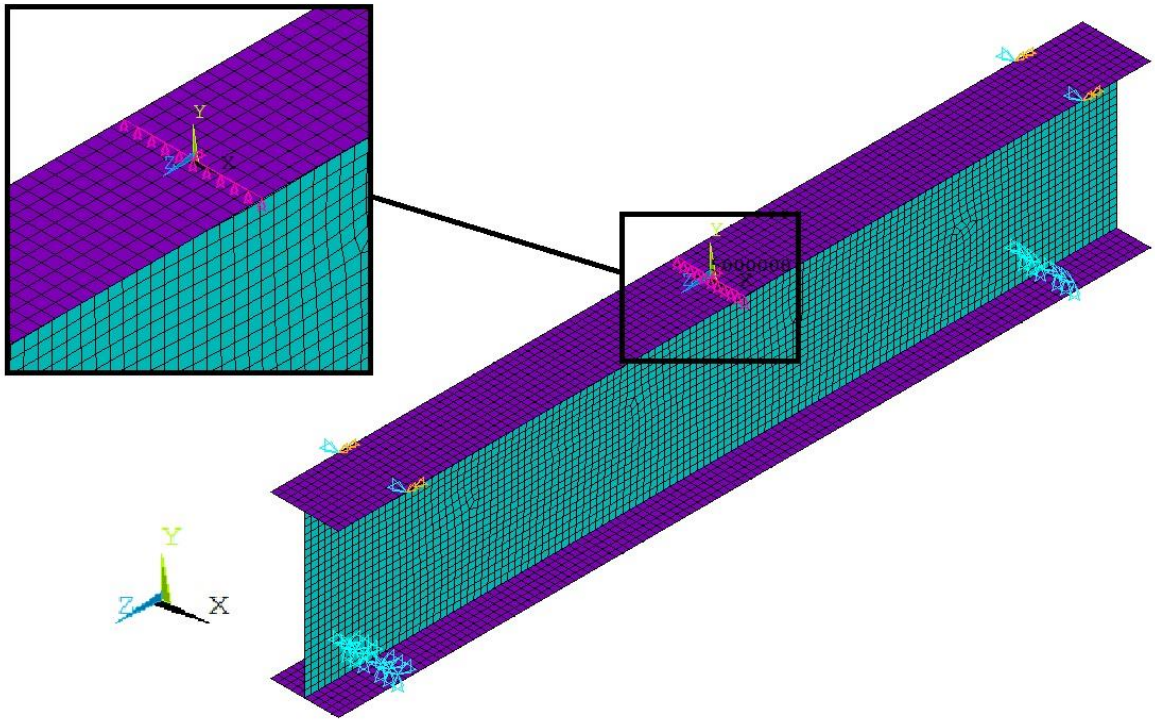

Figure 3.10. Generating rigid region by defining constraint equation.

3.5.2. Application of the force on the mid-span using constraint equations

In three-point bending test, the force on the middle part of the specimen is applied by a pin or roller as shown in Figure 2.1. In order to model this loading condition in the finite

element model, two different methods can be used. The first one is to include the roller or pin in the model and slowly move it downwards. In this method, contact features between the roller and the specimen are defined and then displacement rate of the pin is specified. The second one is to exclude the roller and apply the force directly on the nodes that the roller has contact on the top of the specimen. In this study, the second approach is adopted to apply the force due to simplicity and reduced computational time.

In order to apply the distributed force on the mid-span of the beam, a CE command is used, because the roller of three-point bending test used to apply force on the mid-span is excluded from the model to decrease the cost of analysis. The force is applied to a master node and a rigid connection is defined between this node and the nodes on which the roller has contact. As shown in Figure 3.9, by using CERIG command in ANSYS APDL and defining a key-point as a reference point on the mid-span, the displacement of all nodes which located at the loading section are tied together.

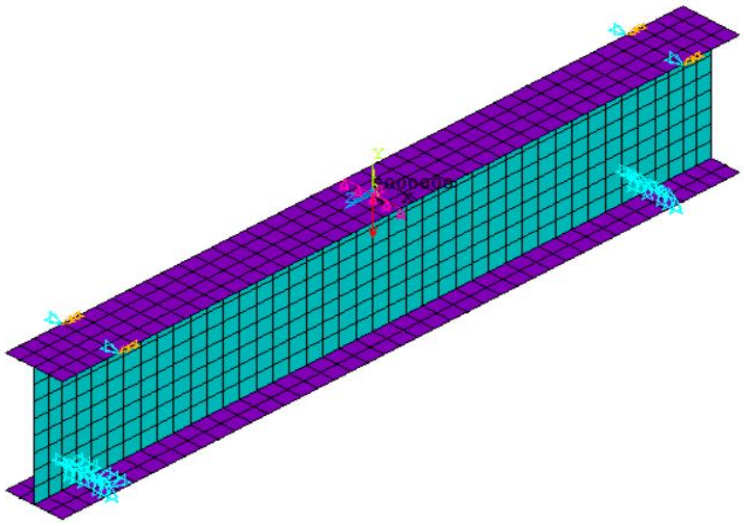

Figure 3.11. The applied loading on specimen from the isotropic view.

3.6. ANSYS Parametric Design Language (APDL) Commands Used to Create the Finite Element Model

The basic commands of APDL code used to define the model and analyze the structure are provided in this section. Table 3.5 is a list of commands for generating the geometry of the model including key-points, lines, and areas. At first, key-points are defined, then by using these key-points, areas generated, and finally the areas are created by pre-defined lines and glue together to get final geometry.

Table 3.4. ANSYS APDL commands for generating the geometry.

Command	Description
K,NPT,X,Y,Z	Define a point with reference number as NPT, and location at (X,Y,Z) in active Cartesian coordinate system
L,P1,P2	Generating line between two points, P1 and P2
A,P1,P2,…,P18	Defines an area by using key-points from P1 to P18, the minimum number of key-points are three and the maximum is 18
AGLUE, All	Merging the areas which are not connected

After generating the geometry of the model, SHELL-181 elements are created on the defined areas using free-mapped quadratic elements. The mesh is generated on the model by using the commands in Table 3.6. Because the mesh size has a great effect on the accuracy of the result, it should be verified that mesh size is sufficiently small to obtain accurate results. In the chapter on the validation of the finite element model, this will be explained.

Table 3.5. Meshing generator commands in ANSYS APDL.

Command	Description
CM,Cname,Entity	Make component by grouping the geometry items such as volumes (VOLU), areas (AREA), lines (LINE), and so on
ESIZE,SIZE	Specifies the size of elements by SIZE
AMESH,All	Mesh all the selected areas by predefined mesh size

After generating the model geometry and defining the mesh, the boundary conditions are imposed to the lines and nodes using the commands in Table 3.7.

Table 3.6. ANSYS APADL commands for imposing boundary and loading conditions to the model.

Command	Description
DL,Nodenum,UX,0	Define displacement in X direction as zero for node, Nodenum
DL,Nodenum,UY,0	Define displacement in Y direction as zero for node, Nodenum
DL,Nodenum,UZ,0	Define displacement in Z direction as zero for node, Nodenum
F,All,FY,VALUE	Specifies force load, VALUE, at all selected nodes in direction of Y
NSEL,S,Loc,Z,VALUE1	Select those nodes which their Z coordinates are equal to VALUE1
NSEL,S,Loc,Y,VALUE2	Reselect those node from previously selected group of nodes which their Y coordinates are equal to VALUE2
ALLSEL	Commands that allows the user to select all items in the modeling space
CERIG,Maste,Slave,Ldof	Generating rigid region to define constraint equation

4. VALIDATION OF THE FINITE ELEMENT

4.1. Model Verification and Validation

In this period of technology, due to the high capacity of computer's computing capability, complex equations and simulations can be solved easily. As a result, finite element analysis software is used commonly in any field especially in the mechanical engineering field to analyze engineering structures and their mechanical behavior. However, simulation models are not an accurate and exact imitation of real-world behavior of simulated systems. Because of this problem, any simulated model should be verified and validated based on its requirements and objectives.

Verification of a simulated model is a means of ensuring that the model accurately represents the behavior of the system. Generally, validation of any simulation models is a three-step procedure [76]:

- Step 1: Design a model which represents the real-world structure
- Step 2: Consider the validation and verification of real-world systems in simulated model
- Step 3: Compare the outcomes of simulated model with the results of the real model

In this study, the finite element model developed in ANSYS APDL is first validated by performing mesh convergence analysis; secondly, by comparing its numerical results with the results of an experimental study.

4.1.1. Validation Using the Experimental Results of Takayanagi et al. [74]

The finite element model developed in this study is verified by comparing its predictions with the outputs of an experimental study. Takayanagi et al. [74] conducted an experimental study on the behavior of CFRP I-beams under three-point bending test. Their main objective was to investigate the shear-lag effect in composite I-beams under transverse loads. They chose three different configurations of I-beams and compared the experimental results with the results of two different beam theories, modified beam theory (MBT) and composite beam theory (CBT).

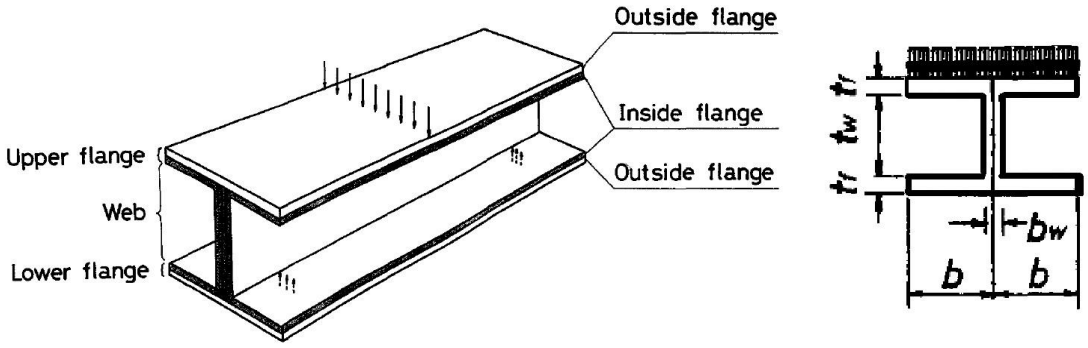

Figure 4.1. Schematic view of the specimen used by Takayanagi et al. [74].

All three specimen have the same length of 500 mm. Their cross-sectional dimensions and the stacking sequences at their flange and web are given in Table 4.1 and Table 4.2 respectively. The schematic view of a specimen is shown in Figure 4.1.

Table 4.1. Cross-sectional dimensions of the specimens [74].

Specimen	b	b_w	t_f	t_w
A	27.36	2.48	2.10	60.17
B	28.32	2.24	2.00	60.17
C	28.36	2.46	2.06	60.17

Table 4.2. Stacking sequences of the CFRP I-beams [74].

Specimen	Flange		Web
	Outside	Inside	
A	UD: $[0]_8$	AP: $[\pm 45]_4$	AP: $[(\pm 45)_4]_s$
B	QI: $[45/0/-45/90]_2$	AP: $[\pm 45]_4$	AP: $[(\pm 45)_4]_s$
C	AP: $[\pm 45]_4$	AP: $[\pm 45]_4$	AP: $[(\pm 45)_4]_s$

The I-beams in that study were fabricated from Toray P3060 (T300/3601) prepreg cured at 180℃. Each ply had a thickness of about 0.125 mm, and each laminate included 16 plies with different stacking sequences. The material properties of the composite material are given in Table 4.3.

In that study, the I-beams were tested using a three-point bending test setup depicted in Figure 4.2. They used three gages to measure the deflection at three different points, one in mid-span and two others at Points A as shown in Figure 4.2.

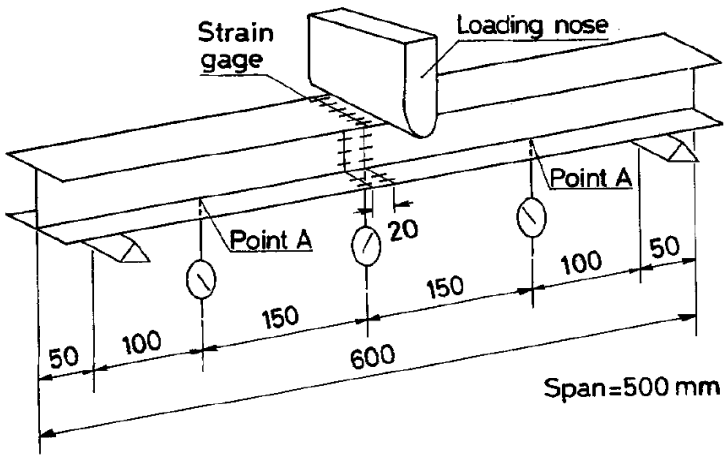

Figure 4.2. Schematic of the I-beam specimen under three-point bending test [74].

Table 4.3. Mechanical properties of Toray P3060(T300/3601) prepreg cured at 180° laminae [74].

Parameter	Value
Fiber Volume Fraction V_f [%]	66
Longitudinal Modulus E_1 [GPa]	150
Transverse Modulus E_2 [GPa]	9.1
Through-Thickness Modulus E_3 [GPa]	9.1
In-Plane Shear Modulus G_{12} [GPa]	4.6
Transverse Shear Modulus G_{13} [GPa]	4.6
Through-Thickness Shear Modulus G_{23} [GPa]	3.05
Major Poisson's Ratio υ_{12}	0.32
Major Transverse Poisson's Ratio υ_{13}	0.32
Through-Thickness Poisson's Ratio υ_{23}	0.49
Longitudinal Tensile Strength σ_{1t} [MPa]	1900
Longitudinal Compressive Strength σ_{1c} [MPa]	1900
Transverse Tensile Strength σ_{2t} [MPa]	68
Transverse Compressive Strength σ_{2c} [MPa]	490
Through-Thickness Tensile Strength σ_{3t} [MPa]	58
Through-Thickness Compressive Strength σ_{3c} [MPa]	490
In-Plane Shear Strength τ_{12} [MPa]	90
Transverse Shear Strength τ_{13} [MPa]	90
Through-Thickness Shear Strength τ_{23} [MPa]	57

4.1.2. Modeling and Simulation

The finite element model developed in this study using ANSYS APDL is adapted to simulate the three-point bending testing of these specimen. The geometry, material properties, layup sequence, and boundary conditions are taken the same as in the experimental study. Other features of the simulation are the same as explained in Chapter 3.

4.1.3. Comparison of Numerical and Experimental Results

In the experimental study, three different stacking sequences for material of I-beams considered. As shown in Figure 4.3 specimen B shows best accuracy when compare to MBT and it is able to suffer largest loading among other three specimens before fracture happens. Takayanagi et al. [74] conducted three-point bending test for each I-beam and plot the Load-Deflection plot for related I-beam and they compared the results with MBT and CBT at the same graph.

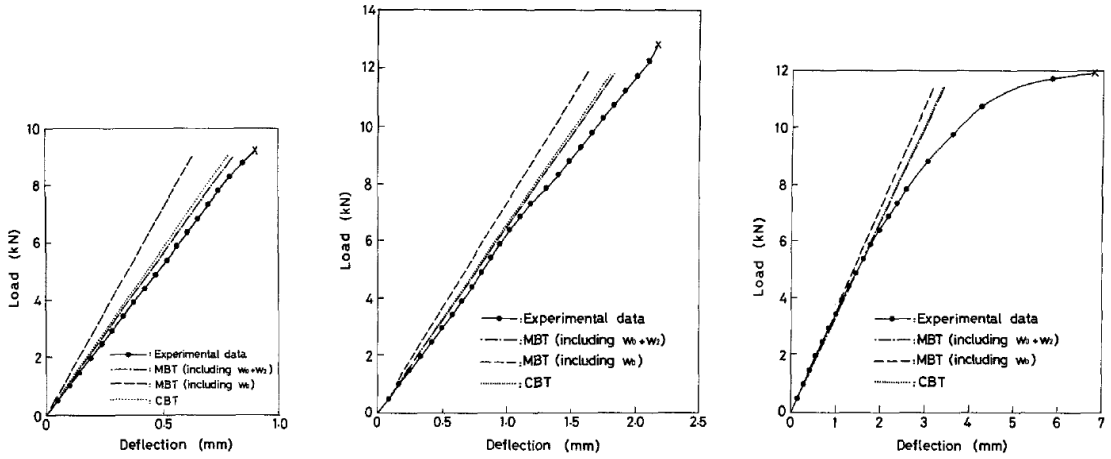

Figure 4.3. Load-Deflection curve for three different specimens under three-point bending test [74].

The values of deflection reported by Takayanagi et al. [74] were obtained by subtracting the measured deflection at point A (Figure 4.2) from the measured deflection at mid-span in order to compensate the effect of flange flattering under loading.

The specimens B and C are chosen for comparison. First, a mesh convergence analysis is carried out to ensure that errors of discretization are limited. The results of simulation are close to results of experimental which the errors of simulation mostly are under 1.5%.

Although, in smaller loads the errors increases due to decrease in flexural rigidity because of shear-lag effect [74].

4.2. Mesh Convergence Analysis

Selecting an appropriate mesh size in finite element analysis (FEA) is a key step in the modeling procedure. The reason of importance of mesh size is its direct relation with accuracy of the results, computing time, and cost of analysis. Based on FEA theory, the finite element (FE) models with small element sizes result in quite accurate outcomes with long computational times, but when larger mesh sizes are used, the accuracy of the outcomes decreases besides analysis time.

Because of importance of mesh size, mesh convergence analysis should be performed for the finite element model to reach the proper mesh size, which yields accurate results with reasonable analysis time [72]. Analysis of mesh convergence and mesh density is recommended for each different geometry to get accurate results. Therefore, mesh convergence analysis is performed for the I-beam under three-point bending loading.

In order to establish appropriate mesh size, the following steps should conducted

- Perform simulation for different mesh sizes.
- Refine mesh sizes in regions where high deformations or high stresses occur.
- Assemble information of analysis for each mesh size, such as results of displacements and stresses, node number, and computing time
- Compare the collected information to select the best mesh size for the finite element model

The errors in deformation, displacement and rotation, are small in comparison with the errors of in stresses. Based on finite element analysis theory, displacements are more

accurately predictable than stresses, since stresses are calculated from the results of displacements [72].

In this study, several element sizes are tried to check convergence of results. In Tables 4.4 and Table 4.5 the deflection results of different mesh sizes are given for specimen B and C, respectively. As shown in Tables 4.4 and 4.5 for mesh sizes under 4 mm the differences in the results are low, therefore the numerical model becomes mesh independent.

Table 4.4. The convergence results for different mesh sizes for specimen B.

Load	**Result of Deflection for Different Mesh Sizes [mm]**						**Experimental**	**MBT Results**
[N]	**8**	**6**	**4**	**3**	**2.5**	**2**	**Result [mm]**	**[mm]**
1000	0.161	0.161	0.160	0.156	0.156	0.156	0.170	0.155
3000	0.485	0.486	0.482	0.468	0.468	0.470	0.500	0.465
5000	0.810	0.812	0.806	0.782	0.772	0.785	0.800	0.775
7000	1.137	1.141	1.132	1.098	1.089	1.102	1.140	1.095
9000	1.468	1.473	1.451	1.418	1.401	1.415	1.540	1.405
11000	1.801	1.809	1.771	1.740	1.721	1.730	1.900	1.725

Table 4.5. The convergence results for different mesh sizes for specimen C.

Load	**Result of Deflection for Different Mesh Sizes [mm]**						**Experimental**	**MBT Results**
[N]	**8**	**6**	**4**	**3**	**2.5**	**2**	**Result [mm]**	**[mm]**
1000	0.305	0.303	0.302	0.303	0.303	0.303	0.300	0.300
3000	0.919	0.911	0.908	0.911	0.910	0.911	0.890	0.890
5000	1.515	1.524	1.518	1.519	1.517	1.517	1.470	1.470
7000	2.158	2.142	2.132	2.140	2.143	2.144	2.220	2.090
9000	2.785	2.765	2.752	2.761	2.767	2.766	3.140	2.710
11000	3.340	3.335	3.310	3.315	3.287	3.283	4.510	3.300

Figures 4.4 and 4.5 present the load-deflection curve for specimens B and C obtained numerically with 4 mm mesh size using the FE model developed in this study and the experimental load-deflection curve and modified beam theory (MBT) results reported by Takayanagi et al. [74].

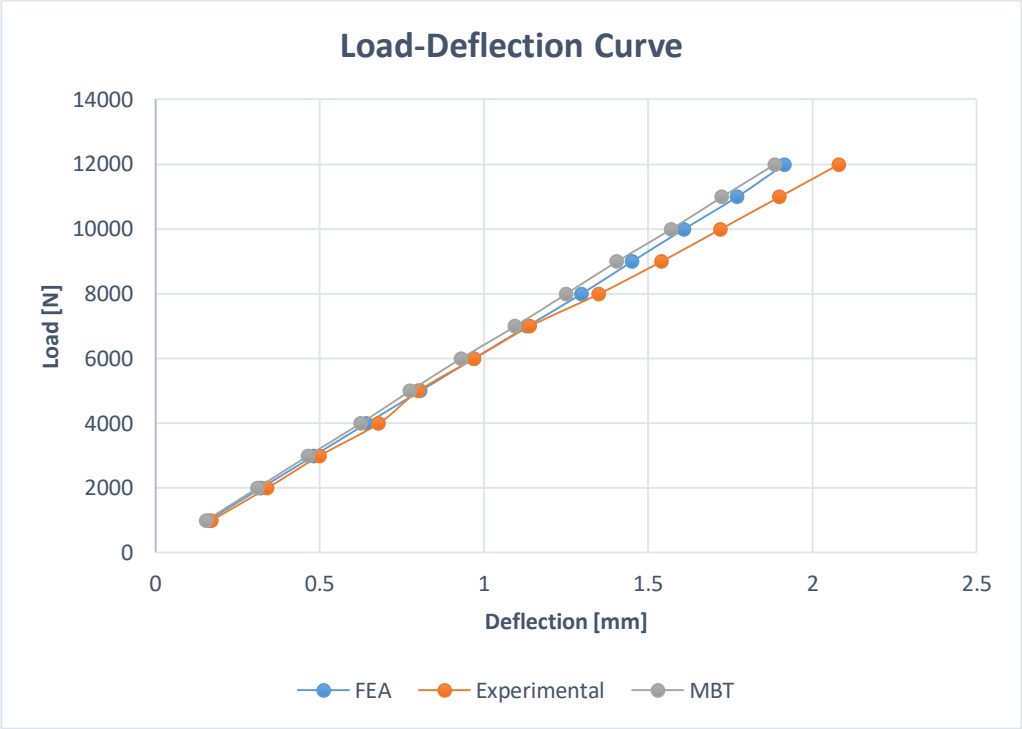

Figure 4.4. The load-deflection curves for specimen B. Experimental and analytical MBT results are reported by Takayanagi et al. [74]. The FEA results are obtained with mesh size equal to 4 mm.

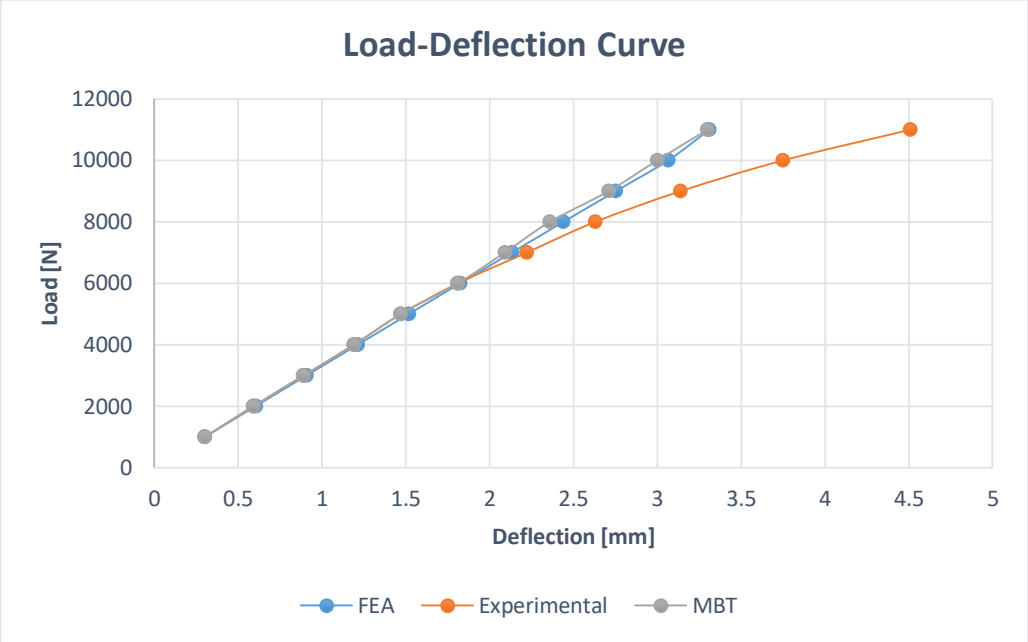

Figure 4.5. The load-deflection curves for specimen C. Experimental and analytical MBT results are reported by Takayanagi et al. [74]. The FEA results are obtained with mesh size equal to 4 mm.

As shown in Figures 4.5 and 4.6, the difference between the experimental results and the numerical one is small at lower load levels. The numerical and experimental curves deviate at higher loads. The nonlinear region in the experimental curve can be attributed to initiation and progression of damage in the specimens during testing. Due to damage stiffness of the specimens decrease. On the other hand, the FE model does not account for damage and associated stiffness degradation. It should be noted that web buckling does not occur in the specimens. The FE model also does not predict web buckling for the load levels applied on the specimens. In a typical buckling curve, load-deflection curve is almost linear up to a point, and then suddenly load drops and a large displacement occur at buckling point. As a result, buckling did not occur in the I-beam. Nevertheless, the FE model developed in this study accurately predicts deflections as long as no significant damage occurs in the beam.

5. OPTIMIZATION PROCEDURE

5.1. Introduction

For most of the human activities there is an inclination to get the most profits and best results with minimum efforts or investments. For instance, in the aviation industry perspective, maximum safety and profit are craved with minimum cost, or in the business outlook maximum gain is desired with minimum investment. The main goal of optimizing a design or structure is to reach the best favorable configuration based on the restrictions and needs of the problem. For each problem in engineering applications, there exist various solutions. The process of selecting the best one among them starts by defining a suitable objective function based on the requirements of the problem. Besides, some restrictions exist that should be satisfied by potential solutions of the problem.

In this study, the rib-reinforced I-beam is optimized using modified simulated annealing (MSA) algorithm. The objective is to obtain the optimum design with the maximum buckling strength-to-weight ratio by optimizing the shape and size of the ribs.

5.2. Objective Function

In this study, the objective function includes both the weight of the rib-reinforced I-beam and the magnitude of the buckling force. Accordingly, a multi-objective optimization is conducted. The optimization procedure tries to maximize buckling strength, while at the same time minimizing the weight of the structure by systematically trying different values for the design variables. The objective function used in this study is

$$f = C_1\left(\frac{LF_0}{LF}\right) + C_2\left(\frac{W}{W_0}\right). \tag{5.1}$$

where, LF is the buckling load factor for a given configuration of rib-reinforced I-beam, LF_0 is the buckling load factor of the I-beam without ribs, W is the total weight of the rib-reinforced I-beam, W_0 is the weight of the I-beam without ribs, and C_is are the weight coefficients. The values of C_is, are chosen depending on the importance that the designer gives to individual term of the objective function. Because the optimization algorithms are configured to minimize the objective function as standard and the buckling load factor is maximized in this study, the objective function includes "$1/LF$" not "LF". Besides, LF and W are normalized with corresponding values of I-Beam with flat web so that discrepancy in their units and magnitudes is removed. The weight of the structure is calculated as

$$W = \rho g V. \tag{5.2}$$

where, ρ is the density of the material ($\frac{kg}{m^3}$), g is the gravitational acceleration ($\frac{m}{s^2}$) and V is the volume of the structure which is calculated automatically by ANSYS APDL.

5.3. Optimization Variables and Constraints

In this thesis, the shape of the ribs is optimized; for this reason, the cross sectional dimensions of the I-beam and its length are taken constant during the optimization process. Besides, number of plies and layup sequence are not varied. Only the variables defining the geometry of the ribs on the web of the I-beam are optimized. Accordingly, four optimization variables are used, which includes height (H_{rib}), length (L_{rib}), width (w_{rib}), and orientation angle of the ribs (θ_{rib}). There exists some restriction for number, length, width and angle of ribs due to dimensions of web. These restrictions are as following

$$H_l \leq H_{rib} \leq H_u \qquad [mm], \tag{5.4}$$

$$L_l \leq L_{rib} \leq L_u \qquad [mm], \tag{5.5}$$

$$w_l \leq w_{rib} \leq w_u \qquad [mm], \tag{5.6}$$

$$\theta_l \leq \theta_{rib} \leq \theta_u. \tag{5.7}$$

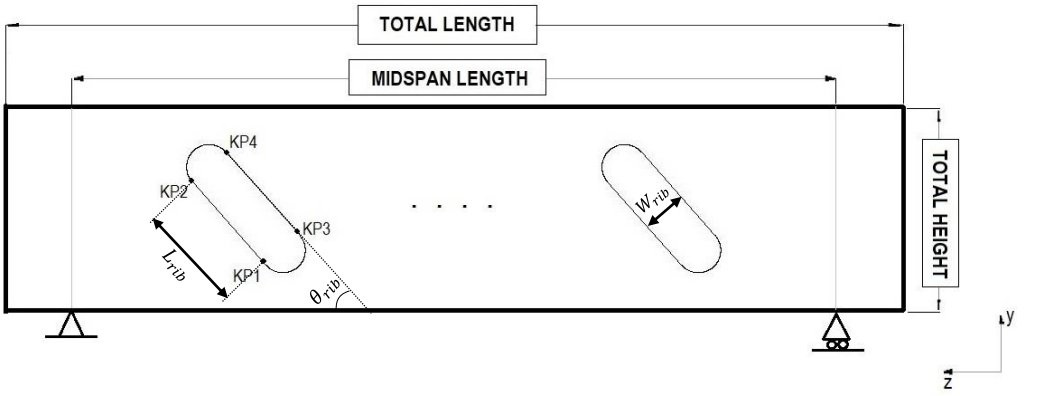

Figure 5.1. The key points of the ribs on the web from normal to web view.

The location and the size of the ribs are defined by four key points. Figure 5.1 shows the key points of a rib on the web. The coordinates of key point one ($KP1$) are specified depending on the chosen location of the rib. The position of other three key points depends on the position of the first key point as well as values of the optimization variables as in Equations 5.8 and 5.9.

$$\begin{cases} y_{KP2} = y_{KP1} + L_{rib} \sin\theta_{rib} \\ y_{KP3} = y_{KP1} + W_{rib} \cos\theta_{rib} \\ y_{KP4} = y_{KP1} + W_{rib} \cos\theta_{rib} + L_{rib} \sin\theta_{rib} \end{cases}, \tag{5.8}$$

$$\begin{cases} z_{KP2} = z_{KP1} + L_{rib} \cos\theta_{rib} \\ z_{KP3} = z_{KP1} - W_{rib} \sin\theta_{rib} \\ z_{KP4} = z_{KP1} - W_{rib} \sin\theta_{rib} + L_{rib} \cos\theta_{rib} \end{cases}. \tag{5.9}$$

Additionally, the position of the key points in the x-direction is the same as that of the web, since they are located on the web. Whenever the values of the optimization variables are changed by the search algorithm, a new shape design is generated.

The positions of the key points are restricted to be within a pre-defined region, which is called search domain as shown in Figure 5.2 with red boxes. When the algorithm randomly selects a set of values for the optimization variables, the corresponding key points are checked. If they are outside the search domain, the configuration is rejected and a new configuration is generated. The key points in the symmetric part of the web have the same y-coordinate as their counterparts, but negative z-coordinate. The optimum shape design for rib-reinforced I-beam is obtained by determining the optimum values of the variables, L_{rib}, W_{rib}, H_{rib},and θ_{rib} via optimization algorithm so that the minimum value of the objective function is attained.

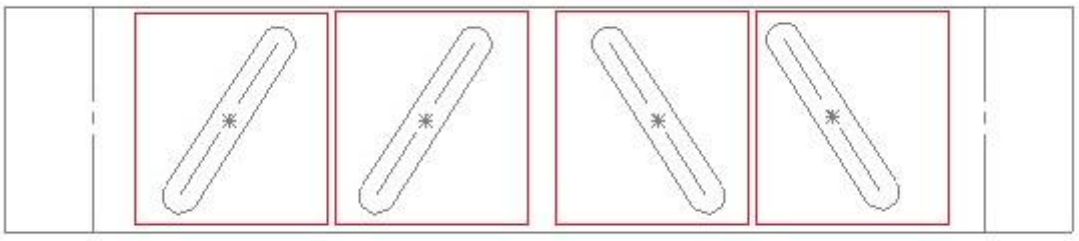

Figure 5.2. Pre-defined search domain for position of key points in optimization algorithm.

5.4. Optimization Technique

In order to find the optimum design of the rib-reinforced I-beam, a modified simulated annealing (MSA) method is used which is presented by M. Akbulut and F. O. Sonmez [5-1]. In this method against ordinary simulated annealing algorithm which just vicinity of a single point is searched, the vicinity of all the current points in the set is searched. In other words, the MSA algorithm creates a new set of configuration in every iteration, the good

configurations are kept in the set. After that, by comparing the objective function value of newly generated configuration with current one, it replaces over the worse one.

In this study there are four parameters which affected on the shape of the design as discussed in the Section 5.3, therefore the number of design variables is four.

$$\mathrm{n} = 4. \tag{5.10}$$

Where n is the number of design variables in this thesis. Changing the position of the key points and number of ribs results in generating a new shape design. The X_{kp} and Y_{kp} are the coordinate of the Kth moving key point of the selected configuration, their values updated by

$$X_{kp} = X_k + C_{rand}R_x, \tag{5.11}$$

$$Y_{kp} = Y_k + C_{rand}R_y. \tag{5.12}$$

Where X_k and Y_k are the coordinates of the current Kth key point, C_{rand} is randomly generated number in the range of $(-1,1)$, R_x and R_y present the maximum distance that each key point can move with different directions. Based on search domain of the study, the position of new key-points depend on the previous key points. The precision of the optimized shape depends on the number of design variables and definition inside the optimization algorithm. In the beginning of the optimization procedure, some shapes are generated randomly. The number of these configurations are related to number of design variables, as

$$N_{conf} = 9 \times n. \tag{5.13}$$

A set of current configuration is kept during the MSA optimization procedure unlike the ordinary SA, which just maintains just one. Newly generated configuration is replaced on the worse ones, if it has accepted value of objective function. The acceptability of newly generated trial set of configuration, which its objective function value calculated by using Equation 5.1, is evaluated by the following criterion:

$$A_t = f(x) = \begin{cases} 1, & f_O < f_h \\ \exp(\frac{f_h - f_O}{T_i}), & f_O \geq f_h \end{cases}. \tag{5.14}$$

Here f_h is the objective function value of one of the current configurations which has highest amount among others. Based on Equation 5.10. if each new design configuration has an objective function value lower than f_h, it is acceptable. Otherwise, the acceptance of new configuration depends on the value of A_t. After calculating the value of A_t, its value will be compared with a randomly generated number P_r which its value is between 0.0 and 0.1. If its value is greater than P_r, the new configuration is accepted. But, if it is lower than P_r, it is rejected. The accepted configuration replaces with inferior configuration. Therefore, after each iteration the objective functions value of current configuration are updated.

The acceptance probability the new configuration is controlled by using a control parameter T_i. At the first stages of optimization procedure, the control parameter has high values which resulted in any configuration is accepted regardless of its objective function value. Taking value for control parameter so large at the beginning of the process leads the search algorithm considers the entire domain. The set of configurations which are generated with constant value of control parameter, T_i, is called Markov chain. Markov chain's minimum length, Lt, is depended on the design variables number:

$$Lt = 3n, \tag{5.15}$$

The length of current Markov chain is controlled by the step size ratio according to Equation 5.12. According to Equation 5.12, the length of current Markov chain is Lt when the step size ratio goes to 0, while at the beginning it is equal to $3n$.

$$Lt_c = nint\left(Lt\left(1 + 2\left(\frac{rs}{rs_{in}}\right)\right)\right), \tag{5.16}$$

where Lt_c is the length of current Markov chain, $nint$ is an command in ANSYS APDL which find nearest integer to the value within the parenthesis, rs and rs_{in} are current and initial step sizes, respectively. Choosing of the initial step size, rs_{in}, depends on the search domain. If the f_o is less than the best configuration during a Markov chain, the current chain is ended and a new one starts. But, if the f_o is less than the worse configuration, it indicates that there is an improvement in the chain. The number of the improvements change according to

$$N_{im} = N_{im} + 1., \tag{5.17}$$

where N_{im} is the number of improvements inside a Markov chain. If the number of improvement is less than 10% of the number of trials, in the other words if there is not acceptable improvement inside the loop, the current step size, rs, reduces such that:

$$rs = 0.9rs, \tag{5.18}$$

In the final step of Markov chain, control parameter (temperature) is decreased as following

$$T_i = \alpha_i T_{i-1}, \tag{5.19}$$

where, α is the temperature reduction factor, T_i and T_{i-1} are the values of the control parameter in the i^{th} and $(i-1)^{th}$ Markov chain, respectively.

$$R_a = \frac{A_m}{in}, \tag{5.20}$$

where R_a is the ratio of the accepted movement and A_m is the number of the accepted points.

$$R_s = \left(\frac{rs}{rs_{in}}\right) + 0.01, \tag{5.21}$$

which R_s is the step size ratio for each iteration. The temperature reduction factor, α_i,is calculated as

$$\alpha_i = \begin{cases} \alpha_{min}, & if\ R_s < R_a \\ \alpha_{max}, & if\ R_a < R_s \end{cases}, \tag{5.22}$$

where, α_{min} is taken as 0.9 and α_{max} is taken as 0.9999. at the final step of the optimization procedure, the worse and best configurations will be compared, if the current control parameter is less than "5e-04" and the difference between the objective function values of the best and worse one is less than "5e-08", the optimization procedure will stop; otherwise the control parameter is decreased again as

$$ck = alfa * ck. \tag{5.23}$$

6. RESULTS AND DISCUSSION

6.1. Finite Element Modeling Results

In the Chapter 4, the model validated and verified. In this part of this chapter the I-beam without rib-reinforced analysis results are discussed. Finite element modeling of this thesis problem is discussed in the Chapter 3. The Table 3.1 gave the dimensions of the I-beam and the Table 3.2 represented the mechanical properties of material which is used in this current study.

During this part two different analysis are discussed, the first one is eigenvalue or linear buckling analysis and the second one is non-linear buckling analysis which considers non-linearity of the geometry. The first analysis done was eigenvalue linear analysis for determination of critical buckling load and buckling modes. After eigenvalue buckling analysis is done, the non-linear buckling analysis conducted to get the near real world result since in the real world tests there exist imperfections in the geometry of the specimen.

6.1.1. Eigenvalue Buckling Analysis Results

As discussed in the Chapter 2, buckling is the rapid change in the shape of structural elements under loading. There exists two different buckling analysis type, eigenvalue buckling and non-linear buckling analysis. The eigenvalue buckling analysis anticipate the theoretical buckling load of a structure without any imperfection.

The eigenvalue buckling analysis is conducted for the I-beam without rib-reinforcement. Figure 6.1 represents first mode of buckling of an I-beam under three-point bending test. As shown in Figure 6.1 the loading factor is 0.580967, and the load applied on the structure is 10 [KN]. Therefore, the theoretical critical load of buckling for this model is 5809.67 [N], which it is obtained by multiplication of loading factor and applied load.

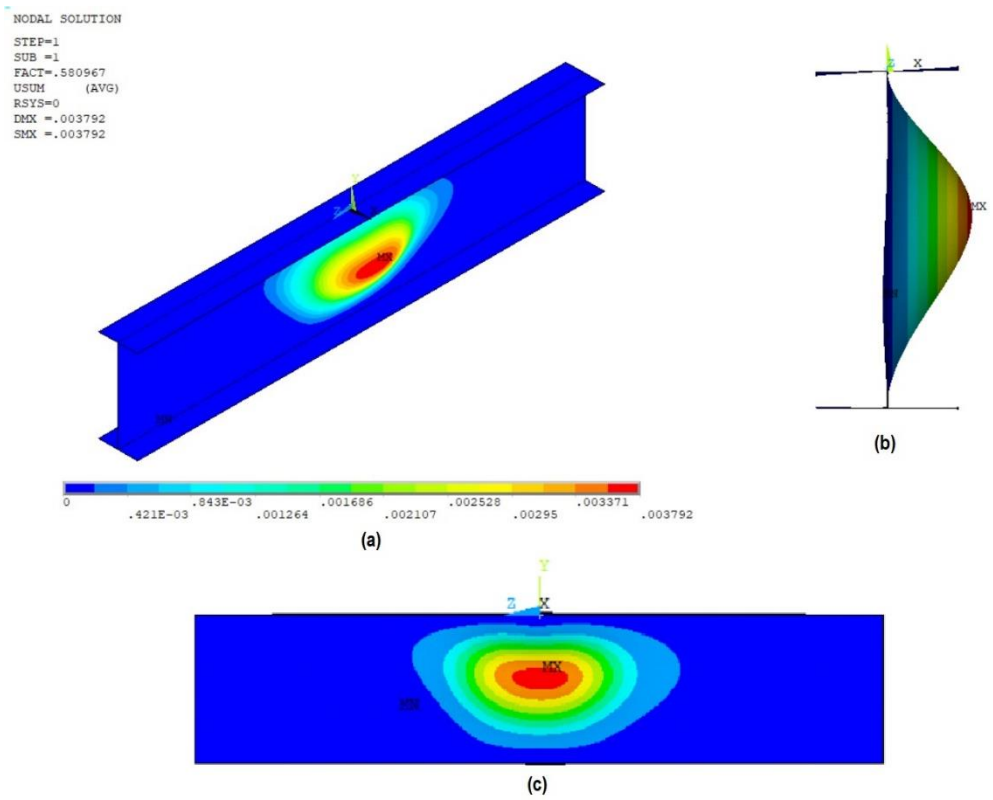

Figure 6.1. First mode of buckling of the I-beam without rib-reinforcement from (a) Isometric view, (b) Right view, (c) Front view.

6.1.2. Non-Linear Buckling Analysis Results

After conducting linear buckling analysis, and finding the theoretical critical buckling load, the non-linearity of the geometry is considered. Non-linear buckling analysis considers imperfections in the geometry and it is more realistic in compare with linear buckling one.

Figure 6.2 represents displacement in the normal to web of the I-beam direction versus time. As one can see at the time around 0.5446 the displacement increased instantly which indicates at this point the structure undergoes to buckling. Since the total loading which applied on structure during total time 1 is 10 [KN], therefore the structure's critical buckling load when non-linearity of the geometry is considered becomes 5446 [N]. Figure 6.3 shows

the displacement contour diagram of the I-beam without rib-reinforcement at the time 0.5446.

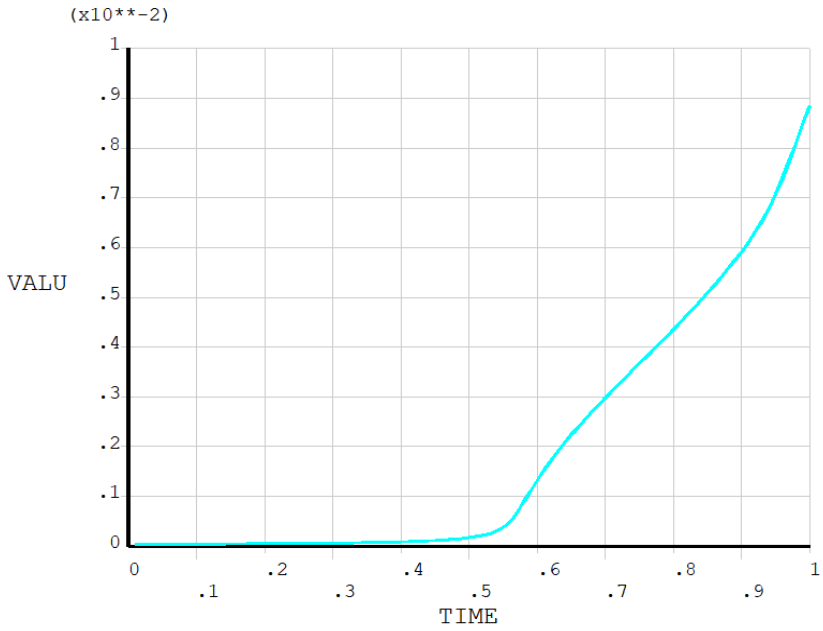

Figure 6.2. Displacement-Time diagram in the middle of the I-beam without rib-reinforcement.

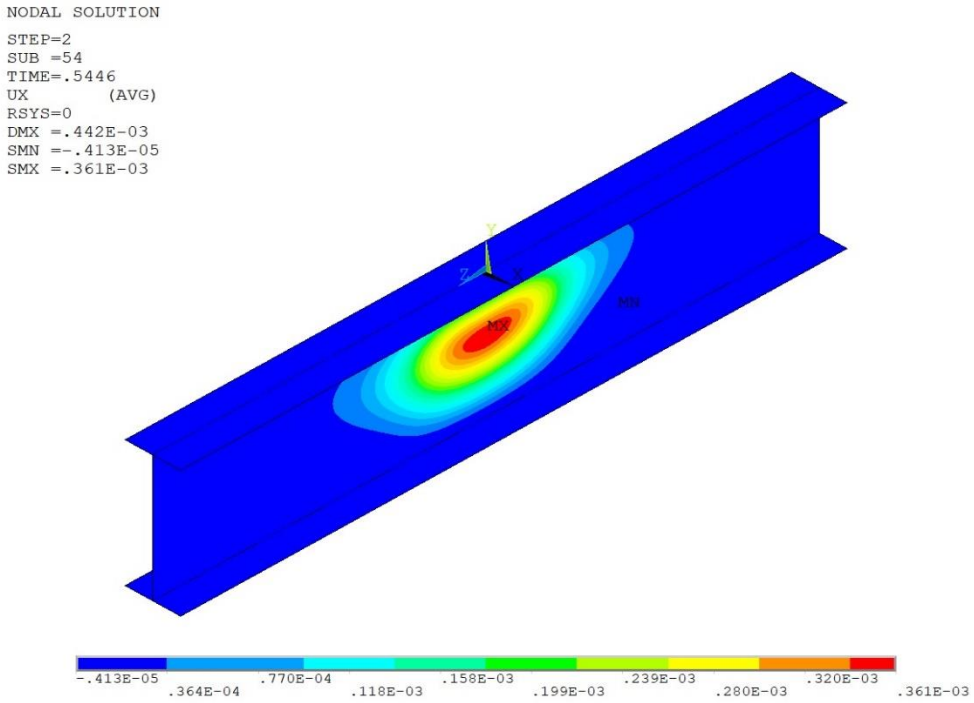

Figure 6.3. Maximum displacement of the I-beam without rib-reinforcement at the time 0.5446.

As shown in Figure 6.4, the Tsai-Wu failure index of the structure in all points of the structure is less than 1. As discussed in the Chapter 2, the Tsai-Wu index for buckling failure should be less than 1, otherwise the dominant failure mode isn't buckling.

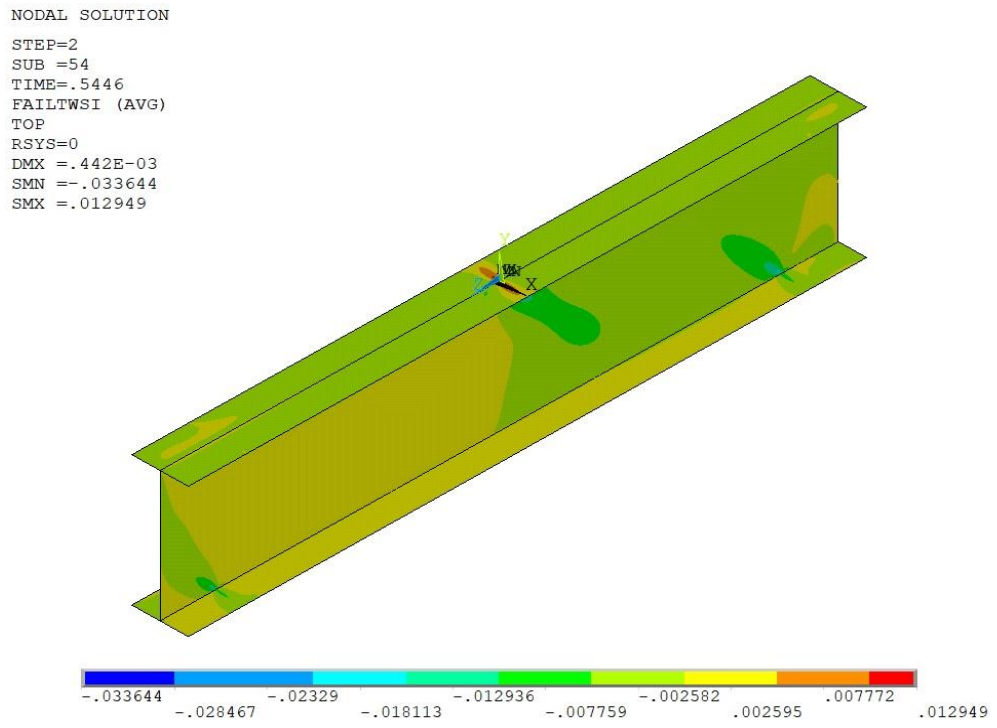

Figure 6.4. Tsai-Wu failure index of the I-beam without rib-reinforcement.

In the conclusion, the theoretical critical buckling load based on the linear analysis is 5809.67 [N] where the theoretical critical buckling load in non-linear analysis is 5446 [N]. The difference between two value is due to considering geometrical non-linearity of the structure in non-linear buckling analysis. Therefore, the result of the non-linear analysis is more realistic than eigenvalue buckling analysis.

6.2. Parametric Study of Rib-Reinforced I-Beam

In this study two different parametric study is done. The first one is for the geometry of the ribs to get the best possible rib configuration and simultaneously to find the upper and lower limits for their length, width, orientation angle, and height. The second parametric study is conducted to survey the effect of the fiber orientation angle of the web of the rib-reinforced I-beam on the critical buckling load. The results of these parametric studies are given in the upcoming section.

6.2.1. Parametric Study of the Ribs Geometry

The main objective of this study is to introduce ribs to the web of an I-beam, and optimize the geometry and number of the ribs to get the best optimized configuration for the ribs. For this reason, three different configurations are considered and analyzed in this study. In the following section the parametric study conducted for these three configurations, and the best one is chosen to implement in the optimization process. Additionally, the upper and lower limits for design variables are calculated.

The first configuration which is considered in this study is ribs in the same orientation angle as shown in Figure 6.5. Different lengths, widths, orientation angles, and number of ribs are analyzed to get best upper and lower limits for them.

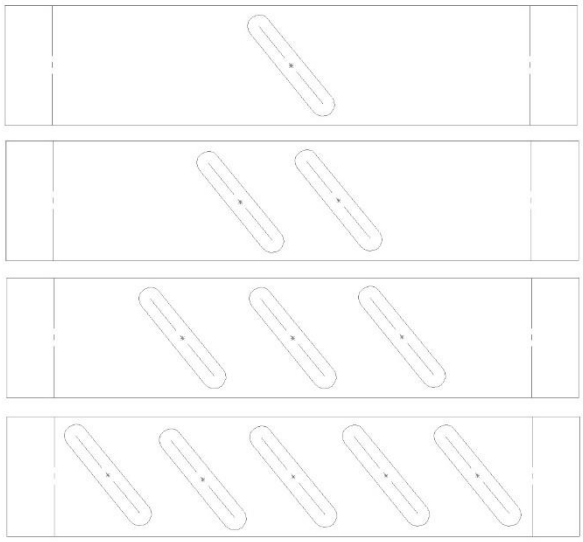

Figure 6.5. First configuration of ribs on the I-beam.

The code of the I-beam is modified to simulate the rib-reinforced I-beam. Figure 6.6 represents simulation of the ribs on the web of the I-beam. Different simulations are done to get the results for various design variable values.

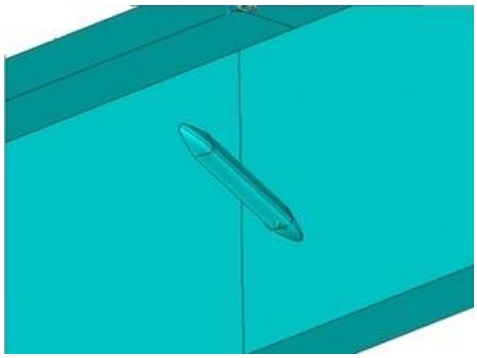

Figure 6.6. Rib simulation on the web of the I-beam.

For the first configuration, the parametric study results are shown in Figure 6.7. Different number of ribs for this configuration modeled and the buckling analysis is done for them. As seen in the Figure 6.7 for the first configuration of the ribs, by increasing the number of the ribs the load factor value decreases. For odd number of ribs, it is decreased dramatically, since there is not any rib in the middle of the rib which has great effect on the increasing the buckling resistance of the I-beam. The best result is obtained when there is a rib which is in the middle of the web of the rib-reinforced I-beam.

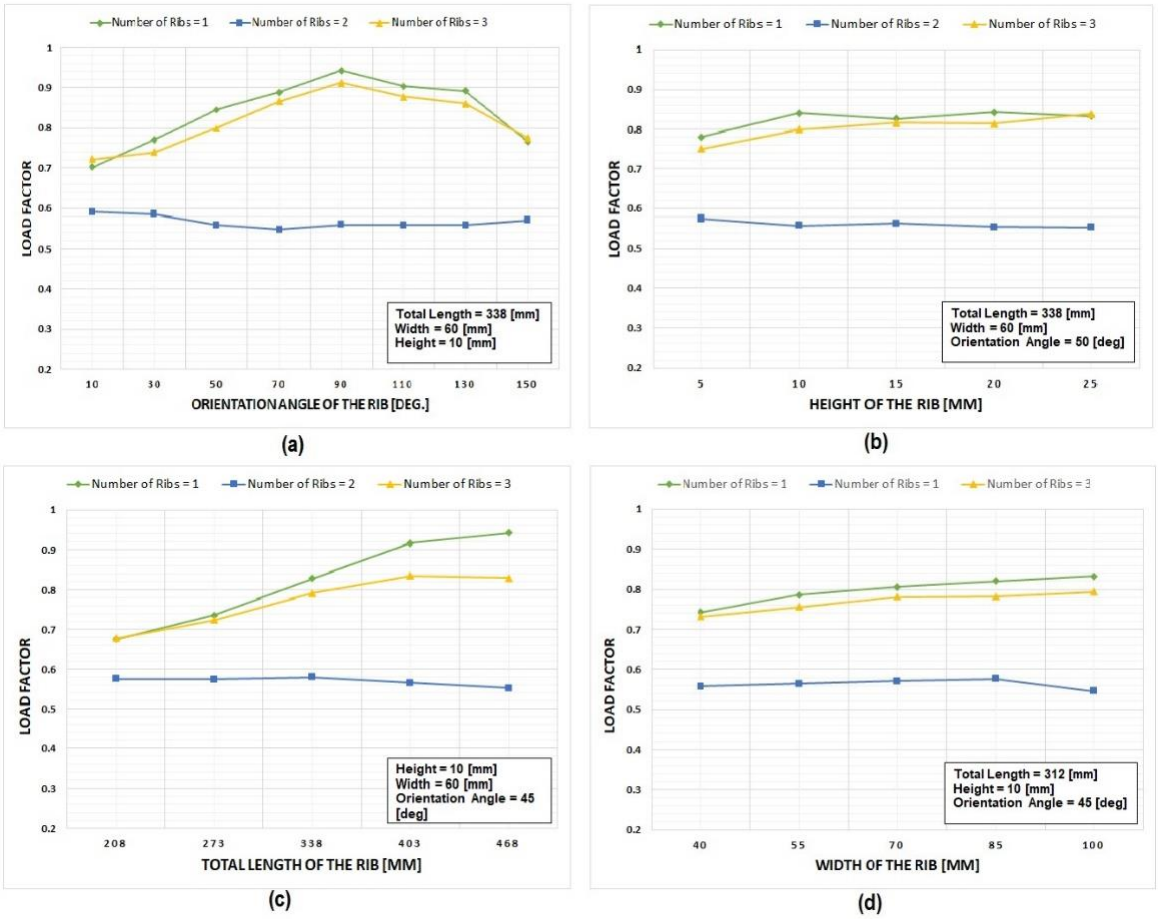

Figure 6.7. The relations between the design variables and effect of them on the critical buckling load for the rib-reinforced I-beam first configuration with different number of ribs, effects of (a) orientation angle, (b) height, (c) total length, (d) width of the ribs.

The next configuration which is considered in this study is ribs which are mirrored about to the middle of the I-beam as shown in Figure 6.8. They have same design variables values; the only difference is their orientation angles about the longitudinal axes of the beam. Different lengths, widths, orientation angles, and number of ribs are analyzed to get best upper and lower limits for them.

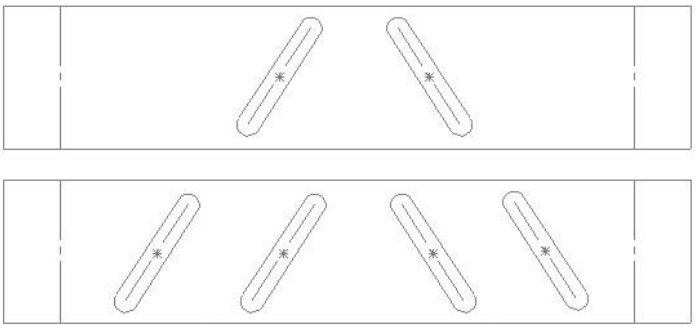

Figure 6.8. Second configuration of ribs on the I-beam.

The final configuration which is considered in this study is ribs which are mirrored about to the middle of the I-beam as shown in Figure 6.9. The difference between this configuration and previous one is the orientation angle sign of the ribs is changed one after another. They have same design variables values. Different lengths, widths, orientation angles, and number of ribs are analyzed to get best upper and lower limits for them.

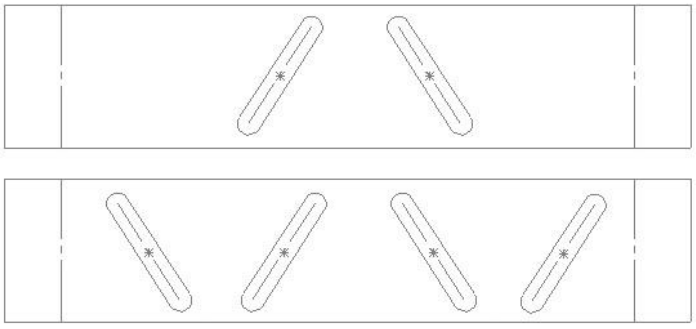

Figure 6.9. Third configuration of ribs on the I-beam.

The individual effects of the design variables on the theoretical critical buckling load of the I-beam is probed in which one parameter is changed at a time and others are considered as constant. The result of the parametric study for the second and third configuration and the best results of the first configuration are presented in the Figure 6.10.

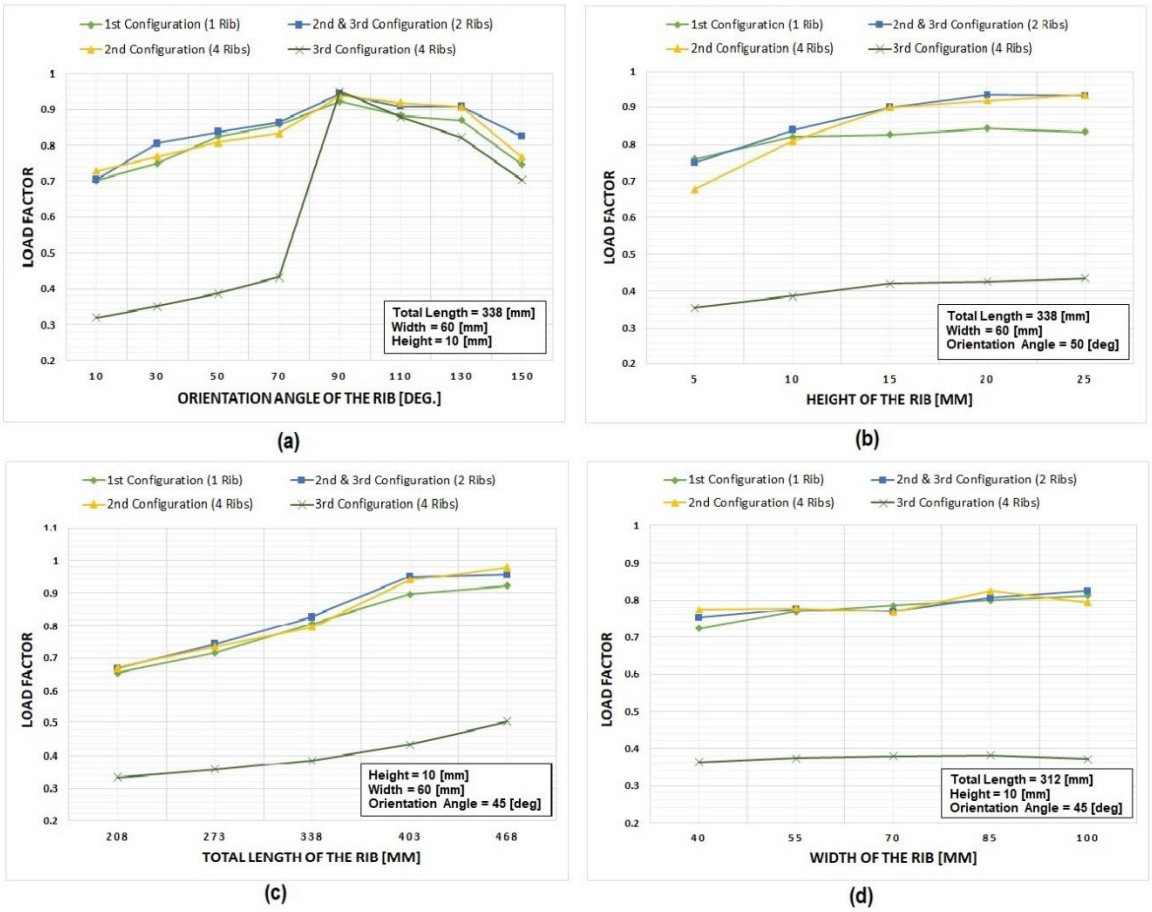

Figure 6.10. The relations between the design variables and effect of them on the critical buckling load for the rib-reinforced I-beam for three different configurations, effects of (a) orientation angle, (b) height, (c) total length, (d) width of the rib.

As shown in Figure 6.10 (a), by increasing the orientation angle of the ribs the critical buckling load of the I-beam increased for all configurations, but after $90°$ the amount of load factor decreased. In Figure 6.10 (b), the height of the rib's effects on the load factor is shown, which by increasing the height of the ribs the load factor increased for all three configurations, but since there exist manufacturing problem for higher values for ribs in composite materials it is not suitable to go beyond the 25 $[mm]$. In Figure 6.10 (c) the total length of the ribs effect on load factor is presented. As one can see, greater value for total length is resulted in greater load factor value, but due to geometry of the web of I-beam, it cannot go farther. The Figure 6.10 (d) shows the relation between the width of the rib and load factor which shows the effect of width size on the load factor in the comparison with other design variables is not considerable. In all of this analysis which are presented in Figure

6.10 the one design variable is changed at a moment and other variables are considered as a constant value.

The parametric study is done for three different rib configurations. As shown in the Figure 6.10, the values for the second configuration in comparison with other configurations is greater, therefore the second one is chosen for the optimization process.

6.2.2. Parametric Study of Fibers Orientation Angle of the Web

After parametric study of the ribs configuration is done and the best possible configuration is selected, a parametric study is conducted for fibers orientation angle of the web. The five different sequences are considered for the fiber orientation angle which are shown in Table 6.1.

Table 6.1. Fiber orientation angle of the web of rib-reinforced I-beam.

Configurations of fiber orientation angle of web
$[+15^{\circ}/-15^{\circ}/-15^{\circ}/+15^{\circ}]_4$
$[+30^{\circ}/-30^{\circ}/-30^{\circ}/+30^{\circ}]_4$
$[+45^{\circ}/-45^{\circ}/-45^{\circ}/+45^{\circ}]_4$
$[+60^{\circ}/-60^{\circ}/-60^{\circ}/+60^{\circ}]_4$
$[+75^{\circ}/-75^{\circ}/-75^{\circ}/+75^{\circ}]_4$

The parametric study for fiber orientation angle for the second configuration with same values for ribs geometry. The length, width, and height of the ribs is considered as a constant value (Total Length is 338[mm], Width is 60[mm], and the Height of the ribs is equal to 10[mm]), but the ribs orientation angle varied for each fiber orientation angle of the web. The result of this parametric study is given in Figure 6.11.

As seen in the Figure 6.11, the best values for the load factor is obtained when the fiber orientation angle is 45°, which the previous parametric study for the rib geometry is conducted for 45° fiber orientation angle.

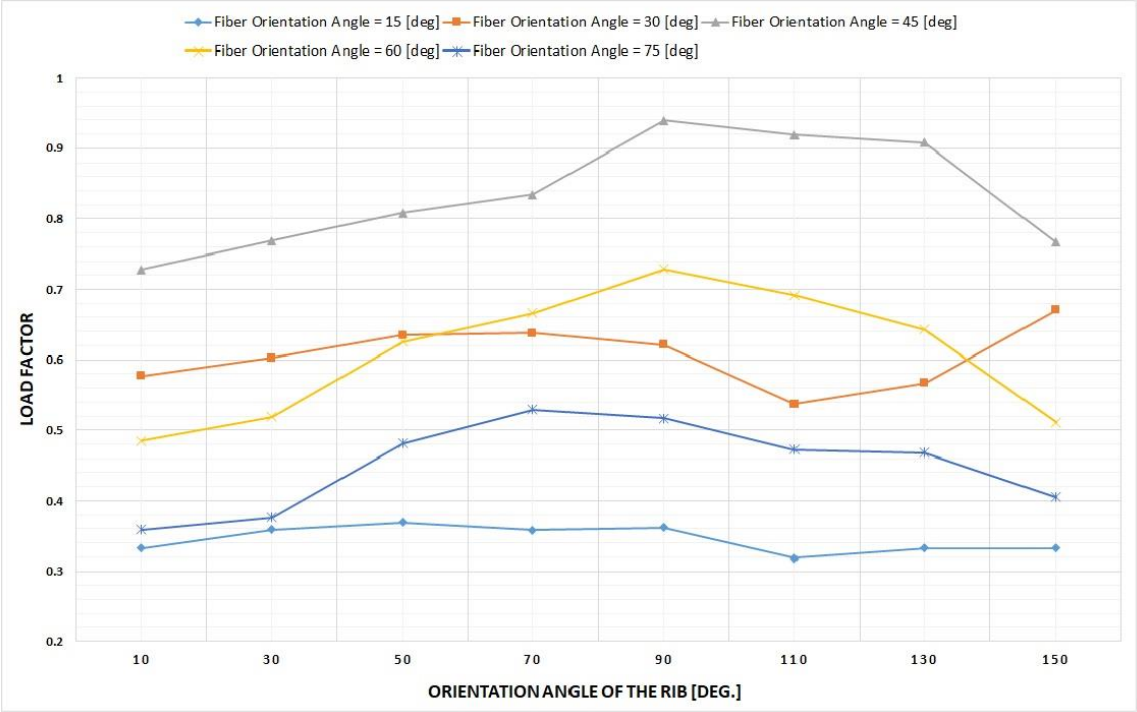

Figure 6.11. Parametric study of the fiber orientation angle.

6.3. Optimization Results of the Rib-Reinforced I-beam

The best configuration of the ribs geometry and the fiber orientation angle is obtained in the previous section. Now, the configuration should go through the optimization process to get the most optimized rib-reinforced I-beam by using the modified simulated annealing algorithm with commercial finite element software ANSYS APDL.

The material used for this study is fiber-reinforced composite. Its mechanical properties are given in Table 3.2. The flange of the I-beam contains 96 plies; the thickness of each ply is 0.125 mm with a total thickness of 12 mm. The web part of the I-beam and ribs contain 16 plies and the total thickness of them are 2 mm. The dimensions of the I-bean

and stacking sequence are chosen for this composite material is given in Table 3.1 and Table 3.2 respectively. The geometry of the flanges is kept constant during the optimization process.

The major goal for the optimization to increase the local buckling resistance in the middle of the web with minimum use of the material. In this study, the optimization process is performed on the rib-reinforced I-beam for a static loading. To begin with optimization algorithm, the relative weights of the terms in the objective function are decided by choosing $C_1 = 0.85$ and $C_2 = 0.15$ in Equation 5.1.

As investigated in the previous parametric study in section 6.2, the best rib configuration and the best number of ribs are chosen. During the optimization process, as shown in Figure 6.12 in some points the buckling failure shifts from the middle of the web to the end parts of the web. To solve this problem, another two ribs added to the web part to prevent this shifts.

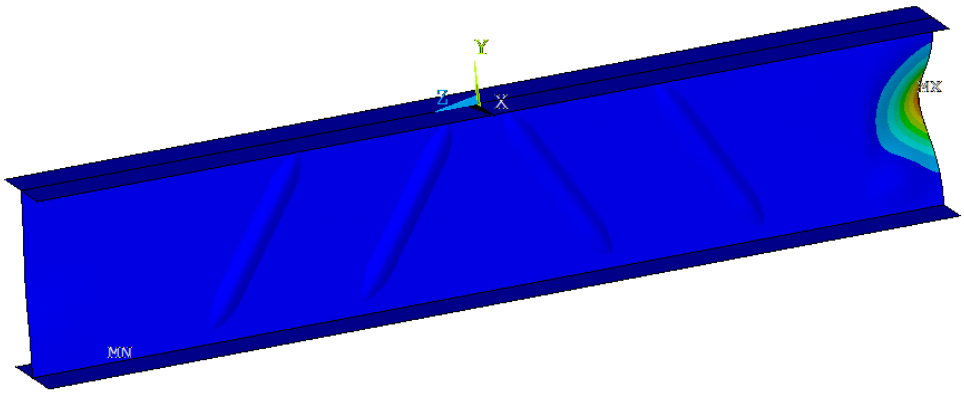

Figure 6.12. Shift of the buckling failure to the both ends of the I-beam from middle of the web.

At the first step, the six ribs are considered with the same distance from each other, but in several configurations they interference with each other as shown in Figure 6.13. For solving this problem two different distancing configuration for the ribs is considered as shown in Figure 6.14, but for distancing (b) in Figure 6.14 the results are better than the distancing (a). Therefore, the second distancing method is used in the optimization

procedure. Additionally, for investigating effect of the other rib number a rib-reinforced with ten ribs is considered during this study.

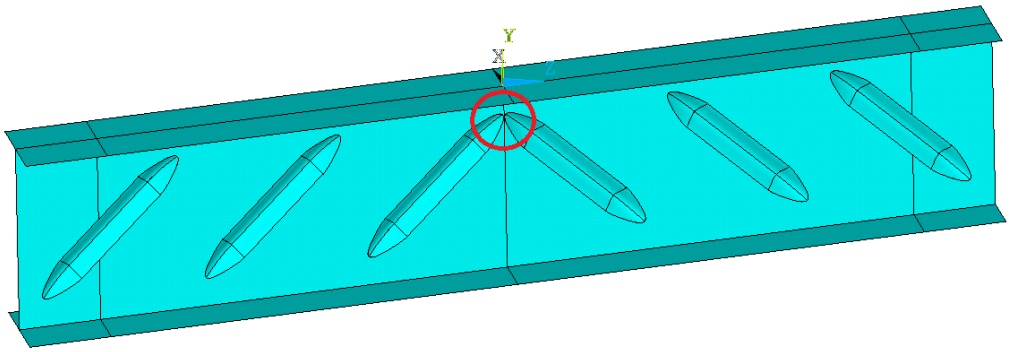

Figure 6.11. The interference of ribs on the web with equal distancing from each other.

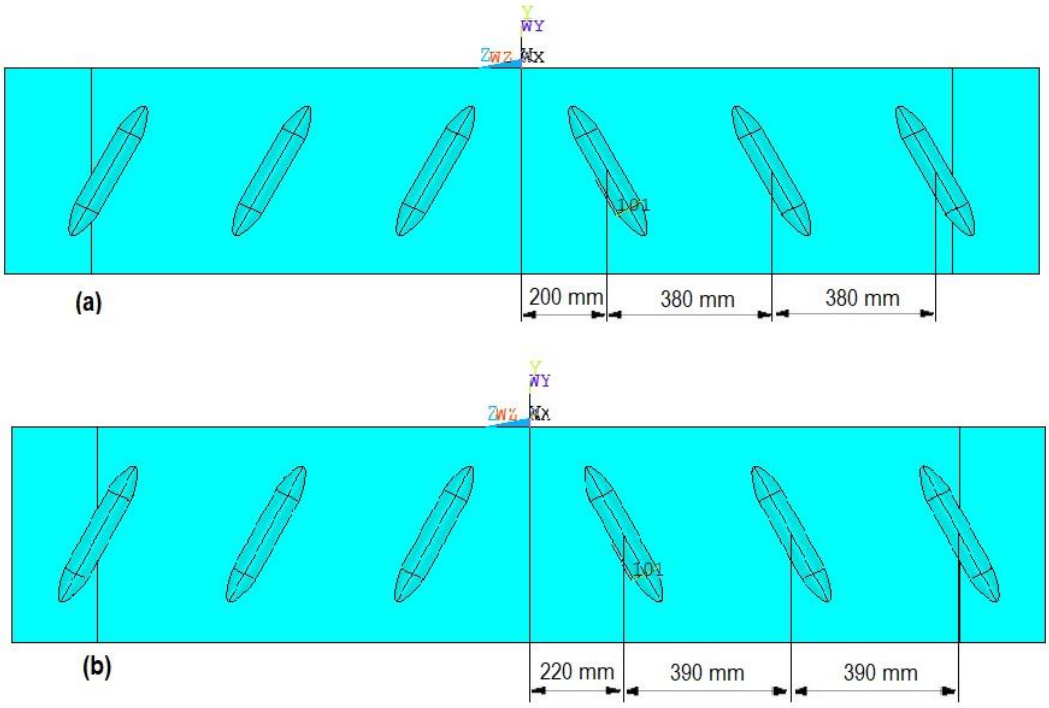

Figure 6.12. The two different distancing for the ribs configurations.

Different limits for optimization variables are considered. Additionally, different directions for rib projection from the web of I-beam are considered. The result for these simulations are presented in Table 6.2.

Table 6.2. The result of different best configurations simulation ("Active" means the constraint is active, i.e., the optimum value is equal to constraint limit.).

Best Configuration	**A**	**B**	**C**	**D**	**E**
Number of Ribs	6	6	6	6	10
Height, H [mm]	25 (Active)	25 (Active)	25 (Active)	25 (Active)	25 (Active)
Length, L [mm]	537.7	532.6	535.7	522.6	559.0
Width, W [mm]	119.8	199.9	296.3	260.8	160.0
Rib Orientation, θ [deg]	44.7	51.3	49.3	50.9	51.1
Buckling Load [N]	26263	30113	40041	40420	66772
Mass (kg)	33.570	33.349	33.242	33.267	33.760
Protrusion in Two Direction	No	No	No	Yes	Yes

The results of best configuration for different optimizations are presented in Table 6.2. The optimization procedure started with configuration A (Figure 6.14 (A)). The height and the width of the ribs are equal to upper limit of the constraint and the other optimization variables are inside the constraint limits. Since the value of the height of the rib is limited by the manufacturing process it is considered as active constraint and further improvement is not possible for it, but for width of the ribs the upper limit of the constraint increased to 200 mm. In optimization process B (Figure 6.14 (B)) again the result of best configuration reaches to the upper limit of width constraint and further improvement is needed. For optimization procedure C (Figure 6.14 (C)) which upper limit for width is considered as 320 mm, the best configuration width value is obtained as 296.3 mm which is inside the constraint limits and because of that the further improvement is not needed for it. As shown in Figure 6.14 (D) the new configuration is considered for rib protrusion (in two different direction) and same analysis is done for it. For further consideration, the rib-reinforced I-beam with protrusion of ten ribs in two different directions is investigated as shown in Figure 6.14 (E).

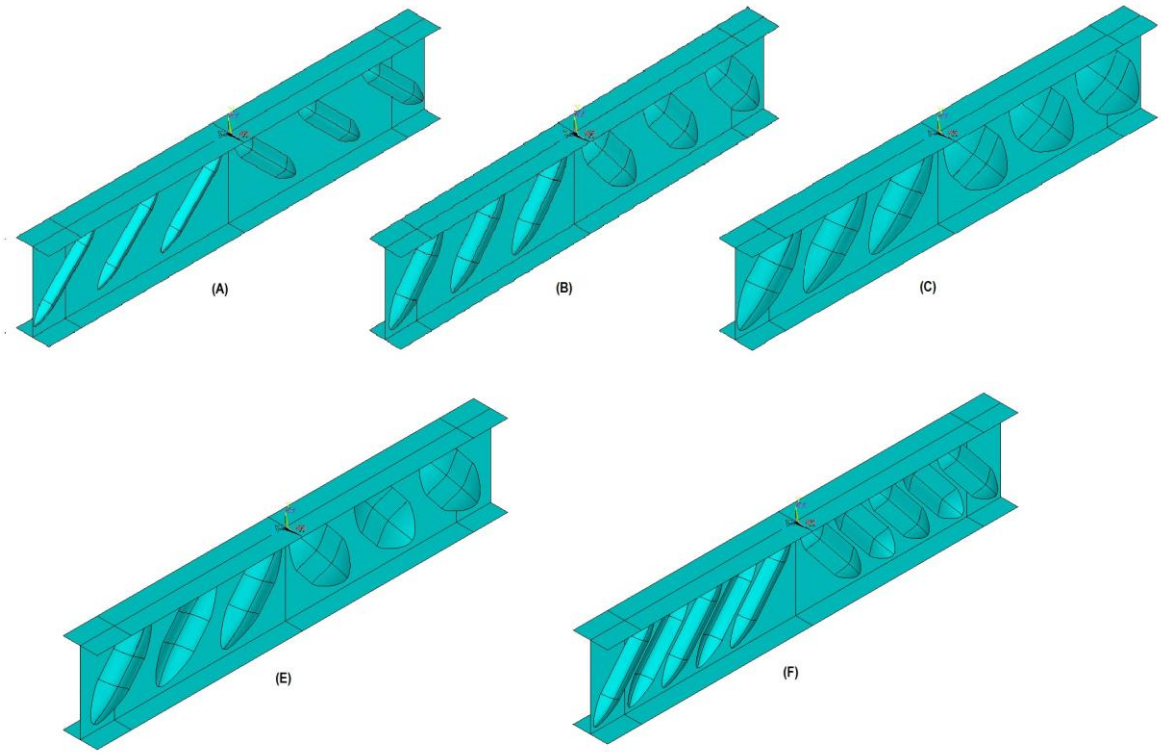

Figure 6.13. The five different configuration of optimization procedure (A), (B), and (C) ribs protrude in positive X-direction (E) and (D) ribs protrude in two different directions.

Figure 6.15 and Figure 6.16 are shown the eigenvalue buckling result and Tsai-Wu failure index respectively for five different configurations. As seen in Table 6.2 and Figure 6.15 the value buckling load is increased by increasing the upper limit of width constraint. In configurations C and D which the difference is their rib protrusion direction, the configuration with protrusion in two different direction gave better results. Additionally, when the number of ribs increased to ten with different protrusion direction the value of buckling load increased about 1.5 times of in comparison with configuration with six ribs where the mass of the structure increased only 1.5%.

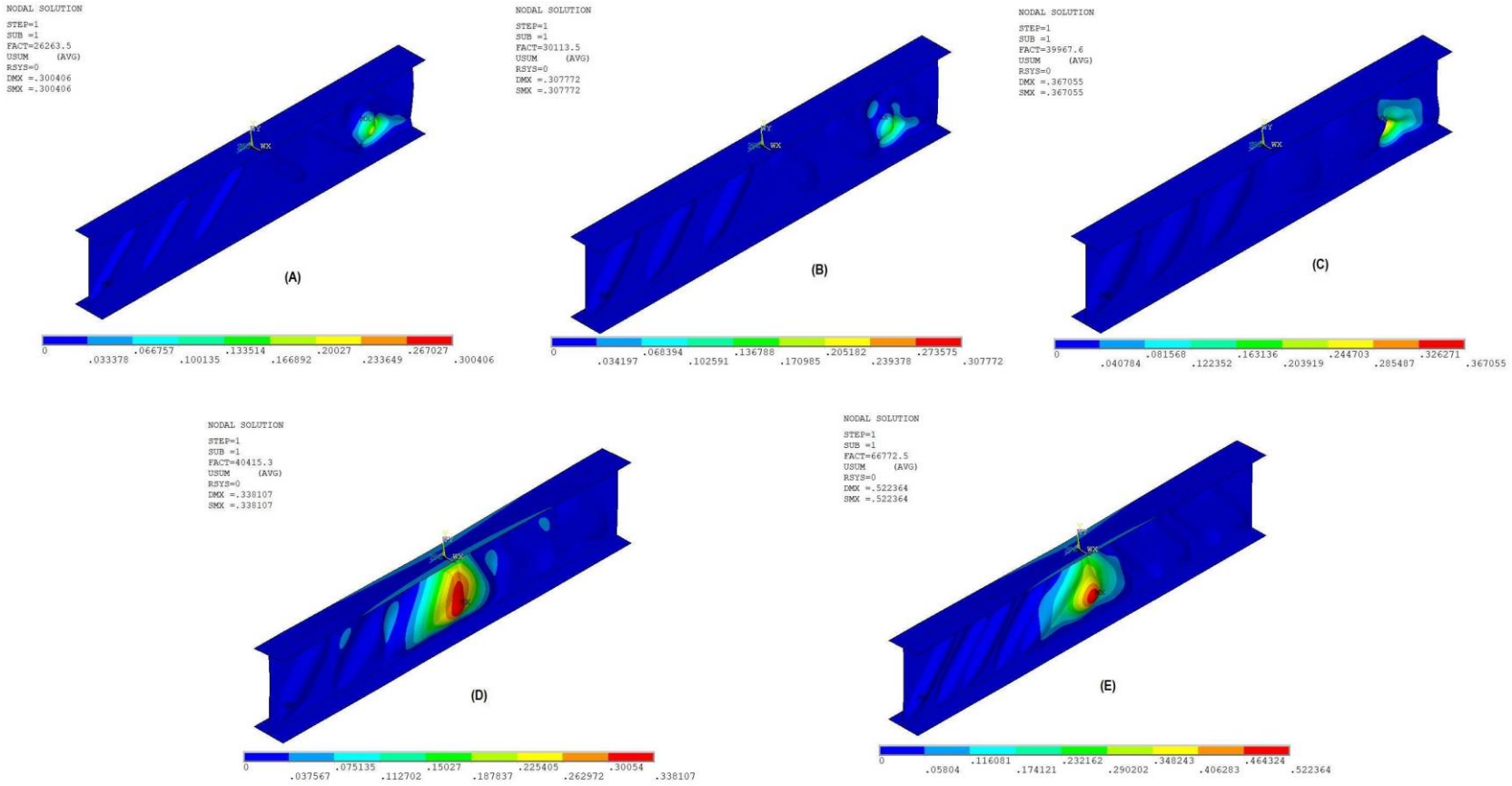

Figure 6.14. Displacement results in normal to web direction of eigenvalue buckling analysis of the five different configuration of optimization procedure, (A), (B), and (C) ribs protrude in positive X-direction (E) and (D) ribs protrude in two different directions.

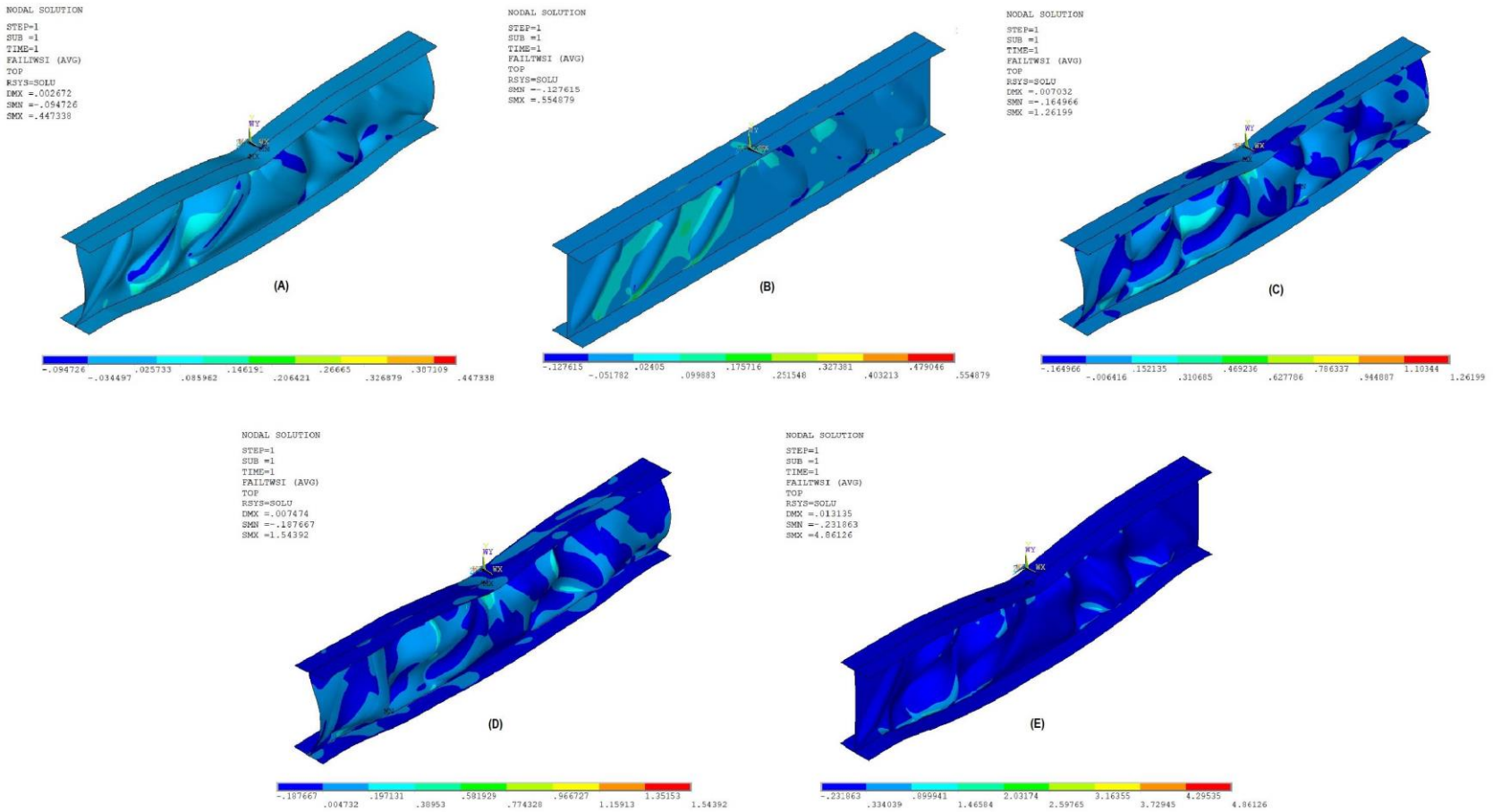

Figure 6.15. Tsai-Wu failure index result of the five different configuration of optimization procedure, (A), (B), and (C) ribs protrude in positive X-direction (E) and (D) ribs protrude in two different directions.

The Figure 6.16 is presented the Tsai-Wu failure index of the configurations. For first three configurations the amount of the Tsai-Wu failure index is lower than one, which is indicated that the dominant failure mode is buckling for these three configurations. As shown in Figure 6.16 (D) and (E), for configurations D and E this value is greater than one only in some local points. The reason of this is loading condition which introduced only on a line over the structure which is in real-world tests the area which loaded is bigger. For solving this problem, one can introduce more layer of material as stiffener on that locations.

The two best results among the five different configurations are configurations D and E. Non-linear buckling analyses is conducted for them. Figures 6.17 and 6.18 depicted the displacement in the normal to web of the configuration D and E, respectively, versus Time. For specimen D, as shown in Figure 6.17 the buckling started at time equal to 0.52 due to instant increase in displacement of the I-beam. Since the total loading which applied on structure during total time 1 is 40.4 kN as mentioned in Table 6.2, therefore the structure's critical buckling load when non-linearity of the geometry is considered becomes 21 kN.

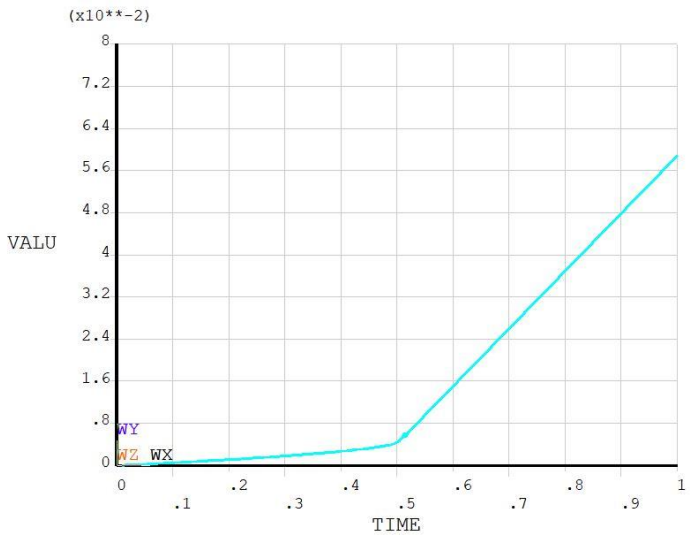

Figure 6.17. Displacement-Time diagram in the middle of the rib-reinforced I-beam, D configuration. Time is the sub-steps which total load is applied over the structure.

For specimen E, as shown in Figure 6.18 the buckling started at time equal to 0.78 due to instant increase in displacement of the I-beam. Since the total loading which applied on structure during total time 1 is 66.7 kN as mentioned in Table 6.2, therefore the structure's critical buckling load when non-linearity of the geometry is considered becomes 52 kN.

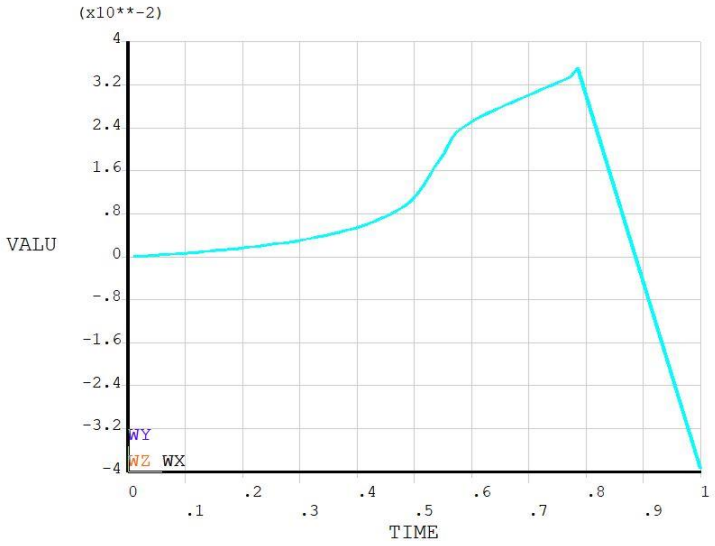

Figure 6.18. Displacement-Time diagram in the middle of the rib-reinforced I-beam, E configuration. Time is the sub-steps which total load is applied over the structure.

Figures 6.19 and 6.20 are shown the Tsai-Wu failure index for configurations D and E, respectively. For configuration D in all point when buckling happened the Tsai-Wu index is less than one, therefore the dominant failure mode for this configuration is buckling. For configuration E at some points especially around the loading part the Tsai-Wu index is more than one. The reason is, the loading applied in a line which is real world it is not happened in this way and the load distributes in larger part, but for withstand this problem, one can add some layer of material to this part to make it stronger, or spread the loading to larger span.

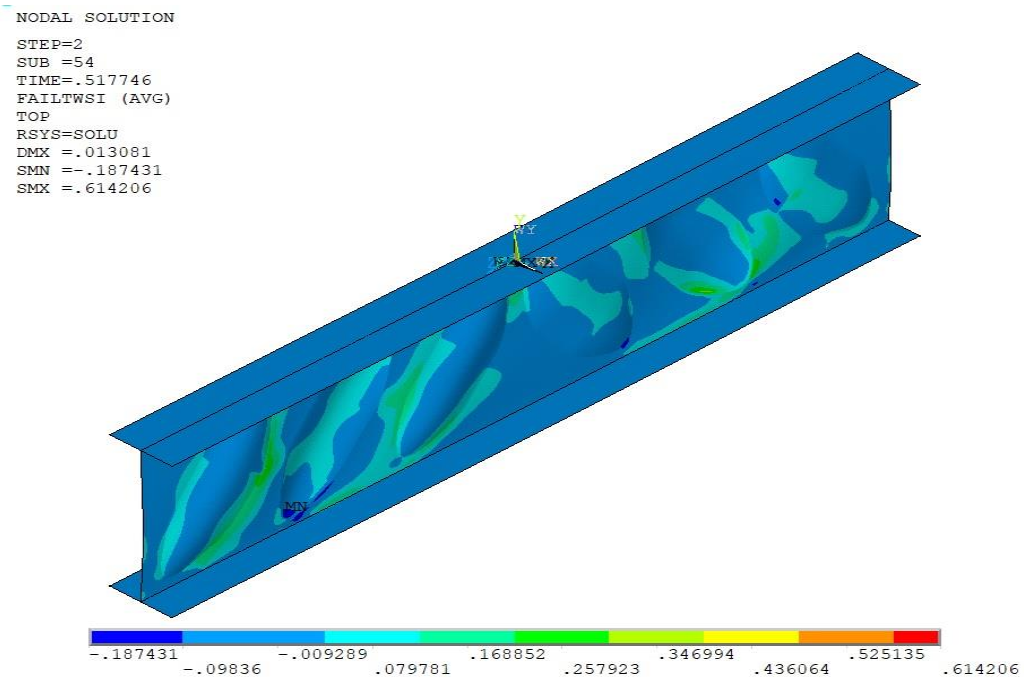

Figure 6.19. Tsai-Wu failure index of configuration D.

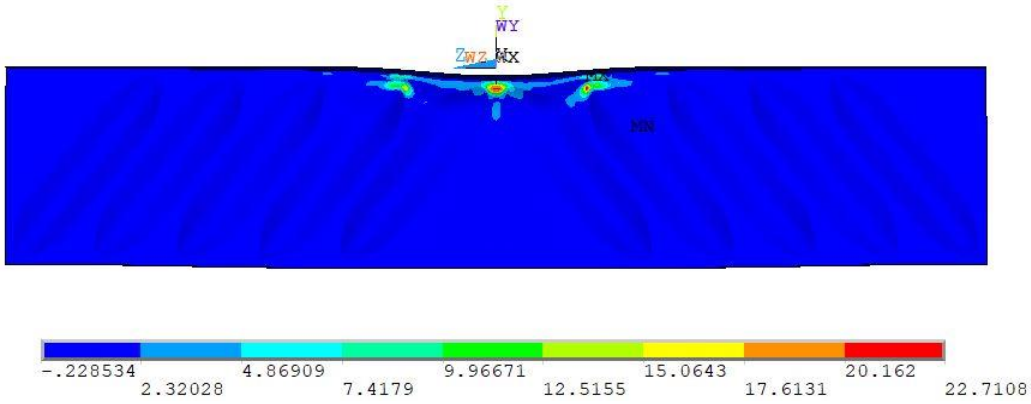

Figure 6.20. Tsai-Wu failure index of configuration E.

7. FUTURE WORKS AND RECOMMENDATIONS

In this study, the buckling failure resistance of a composite I-beam subjected to a bending loading in three-point bending test analyzed and by attaching an optimally designed ribs to it the buckling resistance of it is improved. The optimization variables are length, height, width, and orientation angle of the ribs. For further improvements the stacking sequence, number of laminate plies, the thickness of the web, and general dimensions of the I-beam can be considered as optimization variables. In addition, using different rib configurations, the position of them on the web of the I-beam, and different number of ribs can be a subject for the future studies.

Additionally, since beams are very useful in any field of engineering such civil, aerospace, mechanical, automotive engineering sectors, it is beneficial to study the effect of the ribs for different beam types such as T-type beams and L-type beams

8. CONCLUSION

The main aim of the optimization in this study is to improve the buckling failure resistance of a rib-reinforced I-beam with minimum use of material. A finite element model is developed to simulate the behavior of the beam under three-point bending test. A modified simulated annealing algorithm is used to seek the optimum shape design for the ribs. Different rib configurations are tried and the best one among them is chosen. The length, height, width, and orientation angle of the ribs are considered as the design variables. Six-rib I-beam and 10-rib I-beam are optimized and the optimum configurations are compared with the I-beam without rib-reinforcement.

The I-beam without rib-reinforcement exhibit a low buckling resistance (5.8kN). Changing the stacking sequence of the web laminate does not improve the performance. Increasing the thickness of the web leads to a larger buckling strength, but with a significant increase in material use.

The six-rib I-beam with optimum shape design has a buckling strength of 40.4 kN. This means about 7 times increase in buckling strength and only 0.84% increase in mass compared to the I-beam with flat web. The 10-rib I-beam with optimum shape design has a buckling strength of 66.8. This means about times increase in buckling strength and only 2.33% increase in mass compared to the I-beam with flat web.

Tsai-Wu failure criterion is not used as a constraint during optimization. However, after obtaining the optimum shape design, the critical buckling load is applied statically on the beam and Tsai Wu failure index is calculated. In the main body of the structure, Tsai Wu index is much smaller than 1.0. Only a small region below the point of application of the force is found to be critical. This means locally strengthening this region by additional layers is sufficient to avoid intra-laminar failure of the composite material.

REFERENCES

1. Lucintel's Market Reports, "Growth Opportunities in the Global Composites Industries 2016-2021" Irving, TX, 2016. (Private communication with S. Mazumdar, CEO of Lucintel, a global market research and management consulting firm.)
2. Federal Aviation Administration, *Aviation Maintenance Technician Handbook*. JL Aviation LLC, 2012.
3. https://www.youtube.com/watch?v=cM1mVXSFnq0&t=48s
4. Ogorkiewicz, R. M., Mucci, P. E. R. Testing of fibre-plastics composites in three-point bending. *Composites*, Vol.2, No.3, pp. 139-145, 1971.
5. Yang, T., He, M., Niu, X., and Y. Du, Experimental Investigation of the Three-point Bending Fatigue Properties of Carbon Fiber Composite Iaminates, 2016.
6. Ozbasaran, H., Optimal design of I-section beam-columns with stress, non-linear deflection and stability constraints. *Engineering Structures*, Vol. 171, pp. 385-394, 2018.
7. Yang, B., Zhang, Y., Xiong, G., Elchalakani, M., and S. B. Kang, Global buckling investigation on laterally-unrestrained Q460GJ steel beams under three-point bending. *Engineering Structures*, Vol. 181, pp. 271-280, 2019.
8. Zeinali, E., Nazari, A., and H. Showkati, Experimental-numerical study on lateral-torsional buckling of PFRP beams under pure bending. *Composite Structures*, Vol. 237, p. 111925, 2020.
9. Chambers, R. E. ASCE design standard for pultruded fiber-reinforced-plastic (FRP) structures. *Journal of Composites for Construction*, Vol. 1, No.1, pp. 26-38, 1997.
10. Correia, J. R., Branco, F. A., Silva, N. M. F., Camotim, D., and N. Silvestre, First-order, buckling and post-buckling behaviour of GFRP pultruded beams. Part 1: Experimental study. *Computers & Structures*, Vol. 89, No. 21-22, pp. 2052-2064, 2011.
11. Estep, D. D., Bending and shear behavior of pultruded glass fiber reinforced polymer composite beams with closed and open sections, 2014.
12. Fernandes, L. A., Gonilha, J., Correia, J. R., Silvestre, N., and F., Nunes, Web-crippling of GFRP pultruded profiles. Part 1: Experimental study. *Composite Structures*, Vol. 120, pp. 565-577, 2015.

13. Liu, T., & K. A. Harries, Flange local buckling of pultruded GFRP box beams. *Composite Structures*, Vol. 189, pp. 463-472, 2018.
14. A.A. Elbanna, H. M. Ramadan & S. A. Mourad, Buckling enhancement of longitudinally and vertically stiffened plate girders. *Journal of Engineering and Applied Science*, Vol. 61, No. 1, pp. 351-370, 2014.
15. Barbero, E. J. and I. G. Raftoyiannis, Local buckling of FRP beams and columns. *Journal of materials in civil engineering*, Vol. 5, No. 3, pp. 339-355, 1993.
16. Lindgaard, E., and E. Lund, Optimization formulations for the maximum nonlinear buckling load of composite structures. *Structural and Multidisciplinary Optimization*, Vol. 43, No. 5, pp. 631-646, 2011.
17. Nguyen, X. H., Kim, N. I., and J. Lee, Optimum design of thin-walled composite beams for flexural–torsional buckling problem. *Composite Structures*, Vol. 132, pp. 1065-1074, 2015.
18. Duvaut, G., Terrel, G., Léné, F., and V. E. Verijenko, Optimization of fiber reinforced composites. *Composite Structures*, Vol. 48, No. 1-3, pp. 83-89, 2000.
19. Morton, S. K., and J. P. H. Webber, Optimal design of a composite I-beam. *Composite structures*, Vol. 28, No. 2, pp. 149-168, 1994.
20. Rosensaft, M., and G. Marom, Evaluation of bending test methods for composite materials. *Journal of Composites, Technology and Research*, Vol. 7, No.1, pp. 12-16, 1985.
21. Hansdah K. (2012, November 7). *Three Point Bend Test.* https://www.slideshare.net/kkh007/3-point-bend-test?from_action=save
22. Euler, L., Methodus inveniendi lineas curvas maximi minimive proprietate gaudentes 1744. *Leonhardi Euleri Opera Omnia Ser.* I, Vol. 14, 2010.
23. Xu, J., Zhao, Q., and P. Qiao, A critical review on buckling and post-buckling analysis of composite structures. *Frontiers in Aerospace Engineering*, Vol. 2, No.3, pp. 157-168, 2013.
24. Patil, A., Kolhe, A., Sayeed, A., and A. W. Shaikh, Review of buckling in various structures like plate and shells. *International Journal of Research in Engineering and Technology*, Vol. 3, No. 4, pp. 396-402, 2014.
25. Stresses in Engineering Components, Physics Lecture, pp. 43-46, Queen's University at Kingston, 2002, https://www.physics.queensu.ca/~lynann/lectures/W2L3.pdf, accessed at December 2018.

26. Sharifi, Y., and S. Tohidi, Lateral-torsional buckling capacity assessment of web opening steel girders by artificial neural networks—elastic investigation. *Frontiers of Structural and Civil Engineering*, Vol.8, No. 2, pp. 167-177, 2014.
27. Novoselac, S., Ergić, T., and P. Baličević, Linear and nonlinear buckling and post buckling analysis of a bar with the influence of imperfections. *Tehnički vjesnik*, Vol.19, No.3, pp. 695-701, 2012.
28. Da Silva, V. D., *Mechanics and strength of materials*. Springer Science & Business Media, 2005.
29. Roberts, T. M., and P. S. Jhita, Lateral, local and distortional buckling of I-beams. *Thin-Walled Structures*, Vol. 1, No. 4, pp. 289-308, 1983.
30. Barbero, E. J., and I. G. Raftoyiannis, Local buckling of FRP beams and columns. *Journal of materials in civil engineering*, Vol. 5, No.3, pp. 339-355, 1993.
31. Hancock, G. J., Local, distortional, and lateral buckling of I-beams. *Journal of the Structural Division*, Vol. 104, No. 11, pp. 1787-1798, 1978.
32. Hancock, G. J., Bradford, M. A., and N. S. Trahair, Web distortion and flexural-torsional buckling. *Journal of the Structural Division*, Vol. 106, No.7, pp. 1557-1571, 1980.
33. Daniel, I. M., Ishai, O., Daniel, I. M., and I. Daniel, *Engineering mechanics of composite materials*, Vol. 1994, New York: Oxford university press, 2006.
34. Hyer, M. W., and S. R. White, *Stress analysis of fiber-reinforced composite materials*. DEStech Publications, Inc, 2009.
35. Jones, R. M., *Mechanics of composite materials*. CRC press, 1998.
36. Carlsson, L. A., Adams, D. F., and R. B. Pipes, Basic experimental characterization of polymer matrix composite materials. *Polymer Reviews*, Vol. 53, No.2, 277-302, 2013.
37. Kholkin A., *Numerical Simulation of Damage and Failure of Laminated 3-Point bending specimen.* Vienna University of Technology, Vienna, 2012.
38. Bauchau, O. A., and J. I. Craig, *Structural analysis: with applications to aerospace structures*, Vol. 163, Springer Science & Business Media, 2009.
39. *Euler-Bernoulli Beam Theory*. (2008, November). https://en.wikipedia.org/wiki/Euler%E2%80%93Bernoulli_beam_theory. Retrieved April 2020.
40. Sankar, B. V., A beam theory for laminated composites and application to torsion problems, 1993.

41. Ghugal, Y. M., and R. P. Shimpi, A review of refined shear deformation theories for isotropic and anisotropic laminated beams. *Journal of reinforced plastics and composites*, Vol. 20, No. 3, pp. 255-272, 2001.
42. Reifsnider, K. L., Henneke, E. G., Stinchcomb, W. W., and J. C. Duke, Damage mechanics and NDE of composite laminates. In *Mechanics of composite materials*, pp. 399-420, Pergamon, 1983.
43. Warent L., and R. Akkerman, *Composite Course 2008-2009 6. Laminate Failure*. University of Twente, 2009.
44. Agarwal, B. D., Broutman, L. J., and K. Chandrashekhara, *Analysis and performance of fiber composites*. John Wiley & Sons, 2017.
45. Song, K., Dávila, C. G., & Rose, C. A. Guidelines and parameter selection for the simulation of progressive delamination. In *Abaqus User's conference*, Vol. 41, pp. 43-44, May 2008.
46. *Modelling Cracks and Delaminations in Carbon Fiber Composites*, http://www3.cnde.iastate.edu/ ultrasonics-and-composites/modeling-cracks-and-delaminations-carbon-fiber-composites-frank-margetan, Center for Nondestructive Evaluation Iowa State University, accessed in March 2018.
47. Yuan, Y., Yao, X., Niu, K., Liu, B., and Q. Wuyun, Compressive failure of fiber reinforced polymer composites by imperfection. *Composites Part A: Applied Science and Manufacturing*, Vol. 118, pp. 106-116, 2019.
48. Feld, N., Allix, O., Baranger, E., and J. M. Guimard, Micro-mechanical prediction of UD laminates behavior under combined compression up to failure: influence of matrix degradation. *Journal of Composite Materials*, Vol. 45, No. 22, pp. 2317-2333, 2011.
49. Gdoutos, E. E. (Ed.), *Fracture of nano and engineering materials and structures: proceedings of the 16th European Conference of Fracture, Alexandroupolis, Greece, July 3-7 2006*, Vol. 10, Springer Science & Business Media, 2008.
50. Sun, C. T., Strength analysis of unidirectional composites and laminates, 2000.
51. Lopez, R. H., Luersen, M. A., and E. S. Cursi, Optimization of laminated composites considering different failure criteria. *Composites Part B: Engineering*, Vol. 40, No. 8, pp. 731-740, 2009.
52. Gutkin, R., and S. Pinho, Review on failure of laminated composites: Experimental perspective and modelling, 2016.

53. Hill, R., A theory of the yielding and plastic flow of anisotropic metals. *Proceedings of the Royal Society of London. Series A. Mathematical and Physical Sciences*, Vol. 193, No. 1033, pp. 281-297, 1948.

54. Azzi, V. D., and S. W. Tsai, Anisotropic strength of composites. *Experimental mechanics*, Vol. 5, No. 9, pp. 283-288, 1965.

55. Logan, D. L., *A first course in the finite element method using Algor*. Brooks/Cole Publishing Co, 2000.

56. Kardestuncer, H., *Elementary matrix analysis of structures*. McGraw-Hill Companies, 1974.

57. Memon, B. A., Arc-length technique for nonlinear finite element analysis. *Journal of Zhejiang University-Science A*, Vol. 5, No. 5, 618-628, 2004.

58. Metwally, E. M. I., *Design of Transfer Slabs Using Strut-and-Tie Model* (Doctoral dissertation, MANSOURA UNIVERSITY), 2016.

59. Venter, G., Review of optimization techniques. *Encyclopedia of aerospace engineering*, 2010.

60. Geem, Z. W., Kim, J. H., and G. V. Loganathan, A new heuristic optimization algorithm: harmony search. *simulation*, Vol. 76, No. 2, pp. 60-68, 2001.

61. Awad, Z. K., Aravinthan, T., Zhuge, Y., F. Gonzalez, A review of optimization techniques used in the design of fibre composite structures for civil engineering applications. *Materials & Design*, Vol. 33, pp. 534-544, 2012.

62. Sadeghi, J., Sadeghi, S., and S. T. A. Niaki, Optimizing a hybrid vendor-managed inventory and transportation problem with fuzzy demand: an improved particle swarm optimization algorithm. *Information Sciences*, Vol. 272, pp. 126-144, 2014.

63. Zhang, X., Review of Reliability-Based Design Optimization Approach and Its Integration with Bayesian Method. In *IOP Conference Series: Earth and Environmental Science*, Vol. 128, No. 1, p. 012109). IOP Publishing, 2018.

64. Chen, S. M., and C. Y. Chien, Solving the traveling salesman problem based on the genetic simulated annealing ant colony system with particle swarm optimization techniques. *Expert Systems with Applications*, Vol. 38, No. 12, pp. 14439-14450, 2011.

65. Henderson, D., Jacobson, S. H., and A. W. Johnson, The theory and practice of simulated annealing. In *Handbook of metaheuristics*, pp. 287-319, Springer, Boston, MA, 2003.

66. Erdal, O., and F. O. Sonmez, Optimum design of composite laminates for maximum buckling load capacity using simulated annealing. *Composite Structures*, Vol. 71, No. 1, pp. 45-52, 2005.
67. Ledesma, S., and Aviña, G., R. Sanchez, Practical considerations for simulated annealing implementation. *Simulated annealing*, Vol. 20, pp. 401-420, 2008.
68. ANSYS (2020) "S HELL-181" 19.3 User's Manual http://users.abo.fi/rzevenho/ansys%20fluent%2018%20tutorial%20guide.pdf
69. Çok D. (2019*). Design Optimization of Composite I-beam Wing Spars With Corrugated Web* Bogazici University, Turkey
70. Kaddour, A. S., Hinton, M. J., Smith, P. A., and S. Li, Mechanical properties and details of composite laminates for the test cases used in the third world-wide failure exercise. *Journal of Composite Materials*, Vol. 47 No. 20-21, pp. 2427-2442, 2013.
71. Fleuret, C., Andreani, A. S., Lainé, É., Grandidier, J. C., L'héritier, S., and A. L. Gorge, Complex wing spar design in carbon fiber reinforced composite for a light aerobatic aircraft. *Mechanics & Industry*, Vol. 17, No. 6, p. 614, 2016.
72. More, S. T., and R. S. Bindu, Effect of mesh size on finite element analysis of plate structure. *Int. J. Eng. Sci. Innovative Technol*, Vol. 4, No. 3, pp.181-185, 2015.
73. Banks, J., *Discrete event system simulation*. Pearson Education India, 2005.
74. Takayanagi, H., Kemmochi, K., Sembokuya, H., Hojo, M., and H. Maki, Shear-lag effect in CFRP I-beams under three-point bending. *Experimental mechanics*, Vol.34, No. 2, pp. 100-107, 1994.

APPENDIX A: FIGURE AND DIAGRAMS PEMISSIONS

Figure 1.2 permission

Aircraft Handbooks & Manuals

Any reproduction or modification of this material from original FAA source material is solely the responsibility of the publisher.

Aircraft Handbooks & Manuals

Title	Publication Date	Change/Add. Date
IR-M 8040-1C, Airworthiness Directives Manual	2010	02/27/2013
Amateur-built Aircraft & Ultralight Flight Testing Handbook	2015	
Aviation Maintenance Technician Handbook – General (PDF, 64.9 MB)	2018	
FAA-H-8083-31A, Aviation Maintenance Technician Handbook-Airframe Volume 1 (PDF, 193.9 MB)	2018	
FAA-H-8083-31A, Aviation Maintenance Technician Handbook-Airframe Volume 2 (PDF, 336.3 MB)	2018	
FAA-H-8083-32A, Aviation Maintenance Technician Handbook-Powerplant Volume 1 (PDF, 101.3 MB)	2018	
FAA-H-8083-32A, Aviation Maintenance Technician Handbook-Powerplant Volume 2 (PDF, 91.5 MB)	2018	
Balloon Flying Handbook (PDF, 54.2 MB)	2008	
Balloon Flying Handbook Addendum (PDF)	2016	
Glider Flying Handbook	2013	9/13/2013
Glider Flying Handbook Errata Sheet (PDF)	2013	5/11/2015
FAA-H-8083-21, Rotorcraft Flying Handbook (PDF, 16.1 MB) *Note: This handbook is to be used for **gyroplane** information **only**. Disregard any Helicopter information presented. For current Helicopter information refer to FAA-S-8083-21A, Helicopter Flying Handbook.*	2000	

Top Tasks

- Read the Aeronautical Information Manual
- Download the Airplane Flying Handbook
- Download the Pilot's Handbook of Aeronautical Knowledge (PDF)
- Download the Instrument Procedures Handbook
- Search FSIMS

Figure 2.5 permission

Copyright Clearance Center RightsLink®

My Orders | My Library | My Profile | Welcome amin.deldari1992@gmail.com Log out | Help

My Orders > Orders > All Orders

License Details

This Agreement between Mr. Amin Deldari Alamdari ("You") and Springer Nature ("Springer Nature") consists of your license details and the terms and conditions provided by Springer Nature and Copyright Clearance Center.

Print Copy

License Number	5033720268761
License date	Mar 21, 2021
Licensed Content Publisher	Springer Nature
Licensed Content Publication	Frontiers of Structural and Civil Engineering
Licensed Content Title	Lateral-torsional buckling capacity assessment of web opening steel girders by artificial neural networks — elastic investigation
Licensed Content Author	Yasser Sharifi et al
Licensed Content Date	Feb 16, 2014
Type of Use	Thesis/Dissertation
Requestor type	academic/university or research institute
Format	print and electronic
Portion	figures/tables/illustrations
Number of figures/tables/illustrations	1
Will you be translating?	no
Circulation/distribution	1 - 29
Author of this Springer Nature content	no
Title	Optimum Design of Rib-Reinforce Composite I-beam
Institution name	Bogazici University
Expected presentation date	Mar 2021
Portions	Figure 1
Requestor Location	Mr. Amin Deldari Alamdari Ortabayır Mahallesi. Kavaklı Sokak, No. 2, Daire 3 Kağıthane, İstanbul 34413 Turkey Attn: Mr. Amin Deldari Alamdari
Total	**0.00 USD**

BACK

Figure 2.6 permission

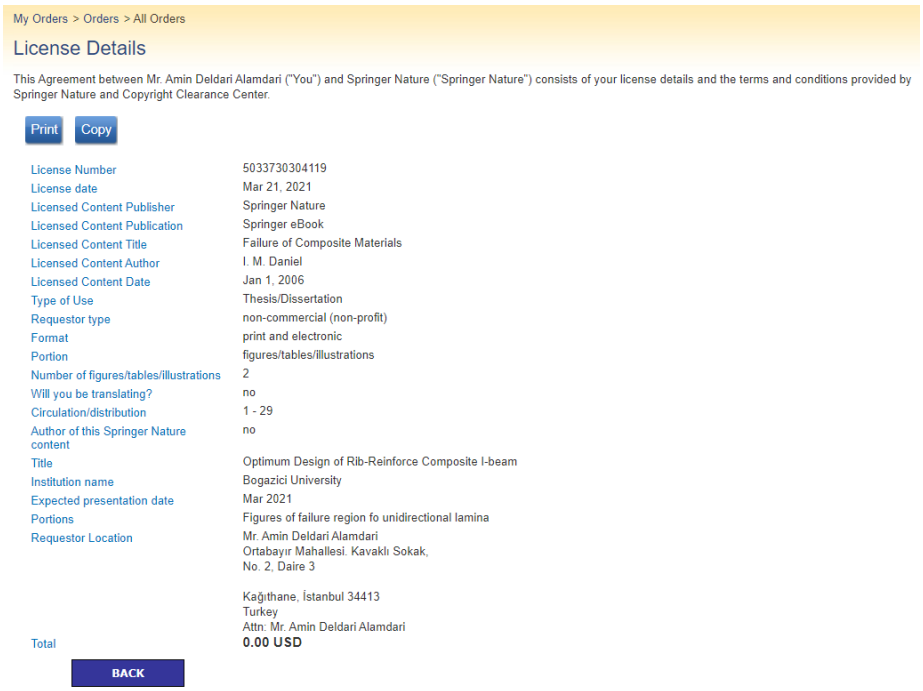

My Orders > Orders > All Orders

License Details

This Agreement between Mr. Amin Deldari Alamdari ("You") and Springer Nature ("Springer Nature") consists of your license details and the terms and conditions provided by Springer Nature and Copyright Clearance Center.

Print Copy

License Number	5033730304119
License date	Mar 21, 2021
Licensed Content Publisher	Springer Nature
Licensed Content Publication	Springer eBook
Licensed Content Title	Failure of Composite Materials
Licensed Content Author	I. M. Daniel
Licensed Content Date	Jan 1, 2006
Type of Use	Thesis/Dissertation
Requestor type	non-commercial (non-profit)
Format	print and electronic
Portion	figures/tables/illustrations
Number of figures/tables/illustrations	2
Will you be translating?	no
Circulation/distribution	1 - 29
Author of this Springer Nature content	no
Title	Optimum Design of Rib-Reinforce Composite I-beam
Institution name	Bogazici University
Expected presentation date	Mar 2021
Portions	Figures of failure region fo unidirectional lamina
Requestor Location	Mr. Amin Deldari Alamdari Ortabayır Mahallesi. Kavaklı Sokak, No. 2, Daire 3 Kağıthane, İstanbul 34413 Turkey Attn: Mr. Amin Deldari Alamdari
Total	**0.00 USD**

BACK

Figures 2.7, 2.12, and 2.13 permission

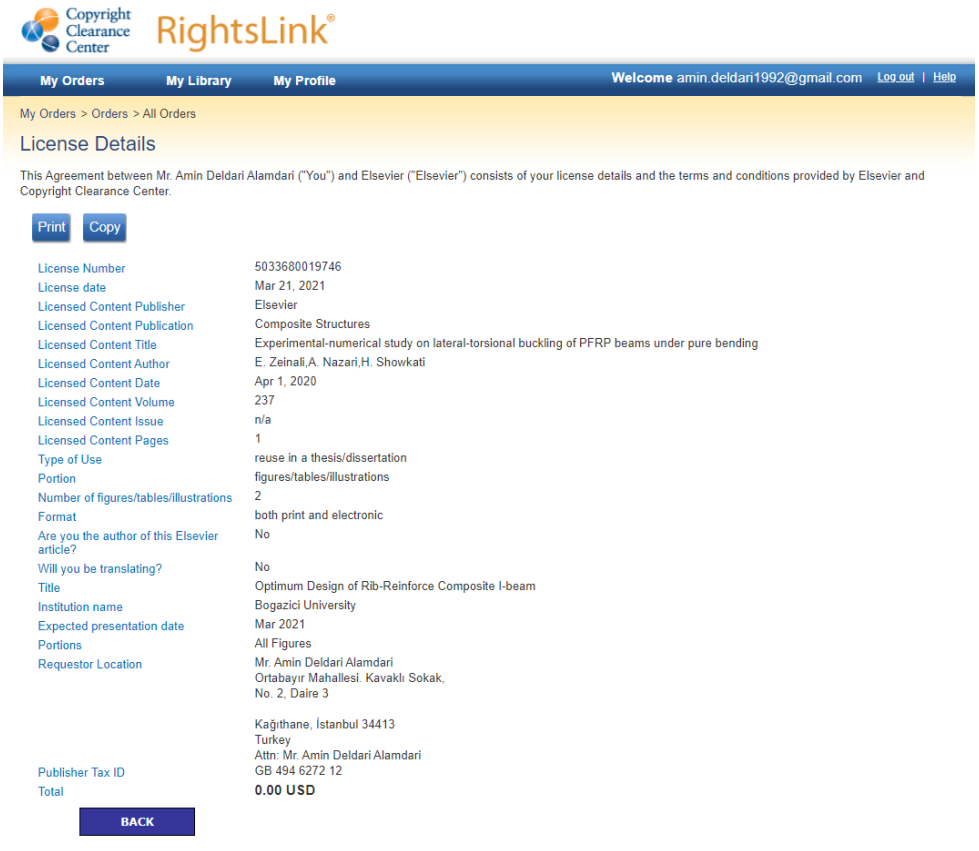

Copyright Clearance Center RightsLink®

My Orders | My Library | My Profile | Welcome amin.deldari1992@gmail.com | Log out | Help

My Orders > Orders > All Orders

License Details

This Agreement between Mr. Amin Deldari Alamdari ("You") and Elsevier ("Elsevier") consists of your license details and the terms and conditions provided by Elsevier and Copyright Clearance Center.

Print Copy

License Number	5033680019746
License date	Mar 21, 2021
Licensed Content Publisher	Elsevier
Licensed Content Publication	Composite Structures
Licensed Content Title	Experimental-numerical study on lateral-torsional buckling of PFRP beams under pure bending
Licensed Content Author	E. Zeinali,A. Nazari,H. Showkati
Licensed Content Date	Apr 1, 2020
Licensed Content Volume	237
Licensed Content Issue	n/a
Licensed Content Pages	1
Type of Use	reuse in a thesis/dissertation
Portion	figures/tables/illustrations
Number of figures/tables/illustrations	2
Format	both print and electronic
Are you the author of this Elsevier article?	No
Will you be translating?	No
Title	Optimum Design of Rib-Reinforce Composite I-beam
Institution name	Bogazici University
Expected presentation date	Mar 2021
Portions	All Figures
Requestor Location	Mr. Amin Deldari Alamdari Ortabayır Mahallesi. Kavaklı Sokak, No. 2, Daire 3 Kağıthane, İstanbul 34413 Turkey Attn: Mr. Amin Deldari Alamdari
Publisher Tax ID	GB 494 6272 12
Total	**0.00 USD**

BACK

Figure 2.8 permission

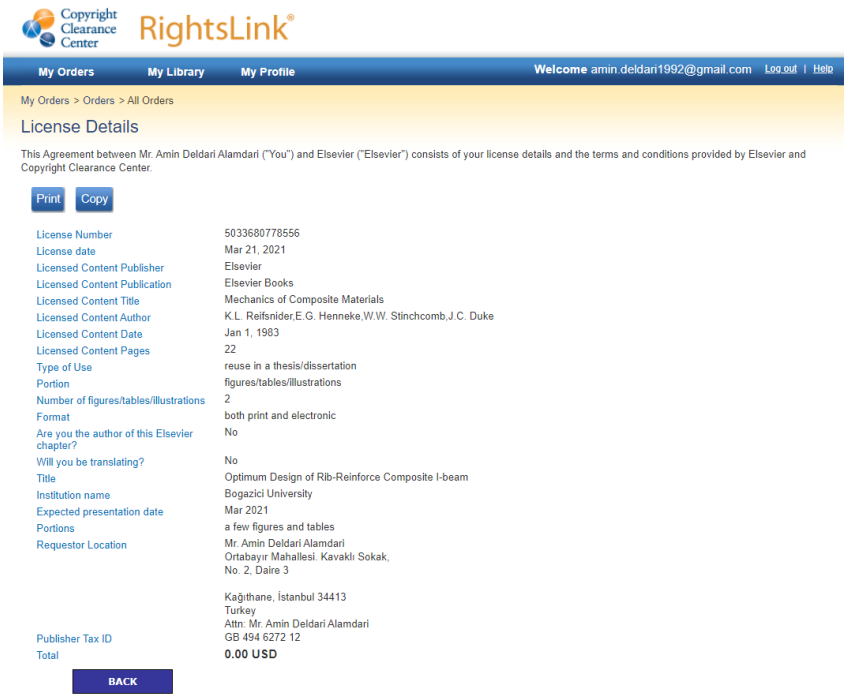

Figures 2.9, 2.10, and 2.11 permission

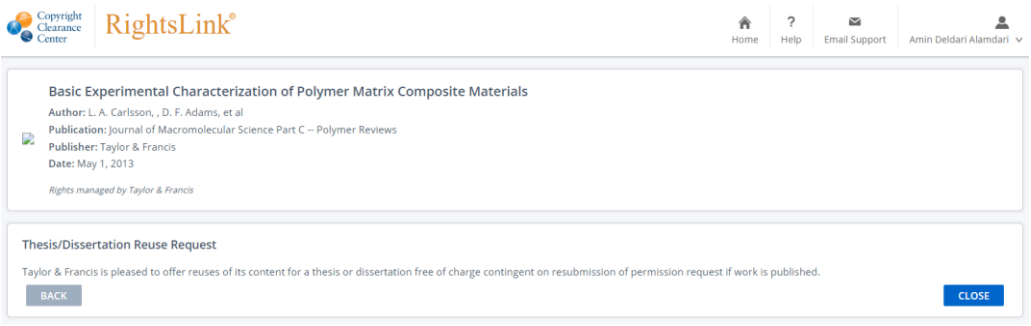

Figure 2.16 permission

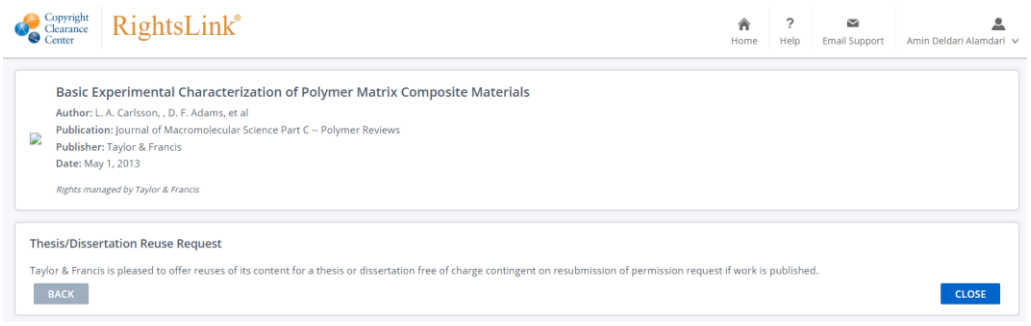

Figure 2.17 permission

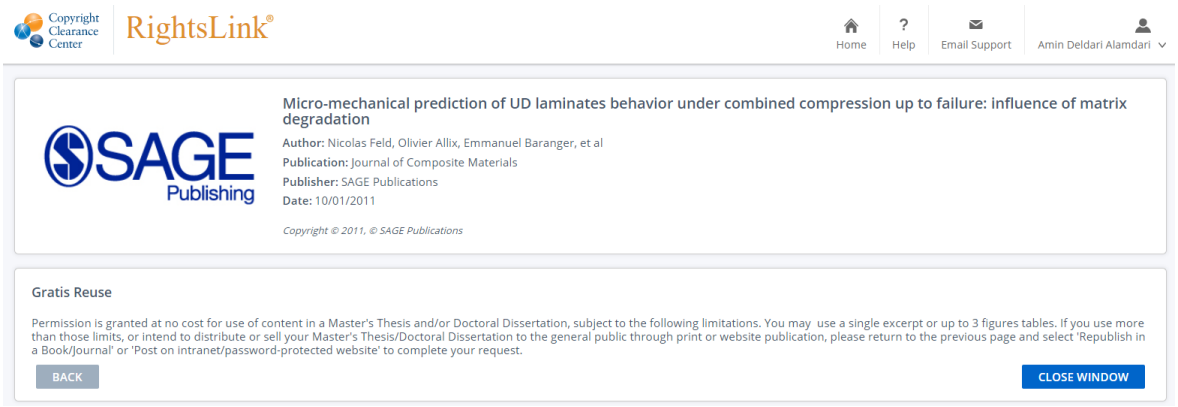

Figures 4.1, 4.2, 4.3,